

**THE UNIVERSITY OF CALGARY**

**Refraction Static Analysis of *P-S* Seismic Data  
Using The Plus-Minus Time Analysis Method**

by

**Jocelyn Dufour**

**A THESIS**

**SUBMITTED TO THE FACULTY OF GRADUATE STUDIES  
IN PARTIAL FULFILLMENT OF THE REQUIREMENTS FOR THE  
DEGREE OF MASTER OF SCIENCE**

**DEPARTMENT OF GEOLOGY AND GEOPHYSICS**

**CALGARY, ALBERTA**

**DECEMBER, 1996**

**© Jocelyn Dufour 1996**



**National Library  
of Canada**

**Acquisitions and  
Bibliographic Services**

395 Wellington Street  
Ottawa ON K1A 0N4  
Canada

**Bibliothèque nationale  
du Canada**

**Acquisitions et  
services bibliographiques**

395, rue Wellington  
Ottawa ON K1A 0N4  
Canada

*Your file Votre référence*

*Our file Notre référence*

**The author has granted a non-exclusive licence allowing the National Library of Canada to reproduce, loan, distribute or sell copies of his/her thesis by any means and in any form or format, making this thesis available to interested persons.**

**The author retains ownership of the copyright in his/her thesis. Neither the thesis nor substantial extracts from it may be printed or otherwise reproduced with the author's permission.**

**L'auteur a accordé une licence non exclusive permettant à la Bibliothèque nationale du Canada de reproduire, prêter, distribuer ou vendre des copies de sa thèse de quelque manière et sous quelque forme que ce soit pour mettre des exemplaires de cette thèse à la disposition des personnes intéressées.**

**L'auteur conserve la propriété du droit d'auteur qui protège sa thèse. Ni la thèse ni des extraits substantiels de celle-ci ne doivent être imprimés ou autrement reproduits sans son autorisation.**

0-612-20824-9

## **ABSTRACT**

The Plus-Minus time analysis (PMT) method was developed to solve the time delays on reflection seismic data caused by low velocity near-surface deposits. The PMT method includes a Plus time analysis for depth analysis and a Minus time analysis for velocity determination. The PMT method was tested with a synthetic dataset and provided a reliable near-surface model.

A refraction analysis involving a three-component 2D seismic line from the Blackfoot area was completed. *S*-wave refractions were identified on the radial component and were used to establish an *S*-wave near-surface model, while *P*-wave refractions were used to build the *P*-wave model. According to the *P*-*S* reflection raypath geometry, the shot static corrections were computed from the *P*-wave model and the receiver static corrections from the *S*-wave model and were applied to the radial component data to produce stacked sections. Improvements in reflector continuity and energy focus were found.

## **ACKNOWLEDGMENTS**

I would like to thank Don Lawton, Rob Stewart, and Gary Margrave for their guidance and precious help in the accomplishment of this research. A special thanks to Darren Foltinek, and Henry Bland for their technical support. This research was supported by the CREWES (Consortium for Research in Elastic Wave Exploration Seismology) sponsors and the FCAR (Fond pour la Formation de Chercheurs et l'Aide à la Recherche) scholarship.

## **DEDICATION**

I would like to dedicate this thesis to my mother, who is a source of inspiration and determination for me.

J'aimerais dédier cette thèse à ma mère, qui est pour moi une source d'inspiration et de détermination.

# TABLE OF CONTENTS

Approval Page.....	ii
Abstract.....	iii
Acknowledgments .....	iv
Dedication.....	iv
Table of Contents .....	v
List of Tables .....	viii
List of Figures.....	ix
Glossary.....	xiii
<b>Chapter 1 - Introduction.....</b>	<b>1</b>
1.1 Background .....	1
1.1.1 Refraction theory.....	1
1.1.2 Refraction history .....	1
1.1.3 Converted-wave ( <i>PS</i> ) seismic theory.....	2
1.1.4 Converted-wave history.....	2
1.2 Thesis objectives.....	2
1.3 Hardware and software .....	3
<b>Chapter 2 - The Plus-Minus time analysis method.....</b>	<b>4</b>
2.1 Introduction .....	4
2.1.1 Purpose of the method.....	4
2.1.2 Theory.....	4
Summary.....	7
2.1.3 Hardware/software requirement.....	7
2.2 Process.....	8
2.2.1 General flow chart .....	8
2.2.2 Reciprocal time check.....	10
2.2.3 Crossover point autopicking .....	11
2.2.3 Crossover point rejection.....	14
2.2.4 Crossover point averaging .....	15
2.2.5 Polyfit and crossover point repicking.....	17
2.2.6 Velocity calculation .....	18
2.2.7 Plus time and Delay time analyses.....	20

2.2.8 Plus time rejection.....	22
2.2.9 Depth calculation.....	22
2.2.10 Static computation.....	23
Weathering correction.....	23
Elevation correction.....	24
Total correction.....	24
<b>Chapter 3 - Synthetic dataset .....</b>	<b>25</b>
3.1 Introduction.....	25
3.1.1 Initial model.....	25
3.1.2 Refracted arrivals.....	25
3.2 Plus-minus time analysis.....	26
3.2.1 Reciprocal time differences.....	26
3.2.2 Crossover points.....	27
3.2.3 Velocity model.....	29
3.2.4 Plus time and Delay time.....	30
3.2.5 Depth model.....	31
3.3 Discussion.....	33
<b>Chapter 4 - Refraction analysis of the Blackfoot 2D-3C data.....</b>	<b>34</b>
4.1 Introduction.....	34
4.2 Shear-refraction analysis.....	38
4.2.1 Identification of <i>S</i> -wave refracted arrivals.....	38
4.2.2 Signal enhancement.....	41
4.3 Plus-Minus time analysis.....	43
4.3.1 Refracted arrivals.....	43
4.3.2 Reciprocal time differences.....	44
4.3.3 Crossover points.....	45
4.3.4 Velocity model.....	50
4.3.5 Plus time and Delay time analyses.....	51
4.3.6 Depth model.....	53
4.3.7 Static corrections.....	54
4.4 Generalized Linear Inversion analysis.....	56
4.4.1 Initial input model.....	56
4.4.2 Final inverted model.....	57

<b>4.5 Comparison of Plus-Minus time analysis method and Generalized Linear Inversion method results</b> .....	<b>58</b>
4.5.1 Depth model comparison.....	58
4.5.2 Static solution comparison .....	60
4.5.3 Common receiver stack comparison .....	61
Vertical component.....	62
Radial component.....	64
4.5.4 Common source stack comparison.....	67
<b>Chapter 5 - Conclusions.....</b>	<b>69</b>
Future work.....	70
References .....	71
Appendix A - Delay time analysis.....	74
Appendix B - The Plus-Minus time analysis method: theory .....	76
Appendix C - The Plus-Minus time analysis method: implementation.....	80
Program overview .....	80
Hardware/software requirement.....	80
Data files .....	81
Files required for import .....	81
Exporting files from PMT.....	82
Interactive editing .....	83
Crossover points .....	83
Crossover point averages .....	84
Velocity model.....	85
Depth model .....	86
Appendix D - Water wells in the area of the Blackfoot 2D-3C data.....	87

## **LIST OF TABLES**

<b>Table C.1. Dataset line orders. ....</b>	<b>81</b>
<b>Table C.2. Trace order attributes. ....</b>	<b>81</b>
<b>Table C.3. Surface station order attributes. ....</b>	<b>82</b>
<b>Table C.4. Source index number order attributes. ....</b>	<b>82</b>
<b>Table C.5. Depth model. ....</b>	<b>82</b>
<b>Table C.6. Velocity model. ....</b>	<b>82</b>
<b>Table C.7. Static corrections. ....</b>	<b>82</b>
<b>Table D.1. Water wells information in the area of the Blackfoot 2D-3C data. ....</b>	<b>87</b>

## LIST OF FIGURES

Figure 2.1. Plus time analysis according to the “plus-minus” method of Hagedoorn (1959).....	5
Figure 2.2. Minus time analysis according to the “plus-minus” method of Hagedoorn (1959).....	6
Figure 2.3. Processing flow chart.....	9
Figure 2.4. Reciprocal time check shot gathers i and j.....	11
Figure 2.5. Direct and refracted raypath for shot gather i. ....	13
Figure 2.6. Crossover point autopicking of the left crossover point for shot gathers i (o) and of the right crossover point for shot gather j (*), according to the traveltimes difference analysis by Lawton (1989) and the branch point analysis of Wang and Cheadle (1995). ....	14
Figure 2.7. Left crossover point determination for shot gather j, established from the overlapping shot spread to the right . ....	16
Figure 2.8. Right crossover point determination for shot gather j, established from the overlapping shot spread to the left.....	16
Figure 2.9. Shot gathers i and j with their left and right crossover points, and the Plus-Minus time analysis window . ....	19
Figure 2.10. Minus time variation displayed in function of twice the receiver separation ( $2\Delta x$ ) and best-fit straight line. ....	19
Figure 2.11. Plus time analysis limitation.....	21
Figure 2.12. Delay time analysis for receiver locations outside the Plus-Minus time analysis window limit.....	21
Figure 2.13. Surface-consistent static corrections including elevation and weathering static corrections for a 2 layer model.....	23
Figure 3.1. Synthetic initial model showing the location of one of the shot gather (25) (vertical exaggeration = 67).....	25
Figure 3.2. Direct and refracted arrival traveltimes resulting from the synthetic model. ....	26
Figure 3.3. Reciprocal traveltimes differences of overlapping shot spreads with shot 25.....	26
Figure 3.4. Crossover autopicking process for the left crossover point of shot gather 20 (o) and for the right crossover point of shot gather 25 (*). ....	27
Figure 3.5. Crossover point averages of the synthetic dataset for the left	

trailing (o) and right leading (*) shot spreads with all the arrival traveltimes.....	28
Figure 3.6. Crossover point statistics for the synthetic dataset.....	29
Figure 3.7. Velocity model calculated from the synthetic arrival traveltimes, including the first layer velocity (+) and second layer velocity (x).....	30
Figure 3.8. Plus time values and statistics for the synthetic dataset.....	31
Figure 3.9. Calculated depth model from the synthetic arrival traveltimes (vertical exaggeration = 67).....	32
Figure 3.10. First layer thickness comparison between the initial model and the calculated model (vertical exaggeration = 107).....	32
Figure 3.11. First layer thickness absolute difference between the initial model and the calculated model.....	33
Figure 4.1. Near-surface geology map of the Blackfoot area modified from Stalker (1957), Geiger (1967) and Irish (1967).....	35
Figure 4.2. <i>P-S</i> reflection raypath geometry.....	36
Figure 4.3. Raypath geometry of the Rayleigh-wave, the <i>S</i> -wave and <i>P</i> -wave refractions.....	38
Figure 4.4. Vertical component data (shot gather #1).....	39
Figure 4.5. Radial component data (shot gather #1).....	39
Figure 4.6. Relative vertical and radial component amplitude of the <i>S</i> -wave refractions.....	40
Figure 4.7. Relative vertical and radial component amplitude of the <i>P</i> -wave refractions.....	40
Figure 4.8. Relative vertical and radial component amplitude of the Rayleigh-wave.....	41
Figure 4.9. Radial component from the Blackfoot dataset (shot gather #1).....	42
Figure 4.10. Radial component with an <i>F-K</i> filter applied and <i>S</i> -wave refractions picks (*).....	42
Figure 4.11. <i>P</i> -wave refracted arrival traveltimes from the vertical component data.....	43
Figure 4.12. <i>S</i> -wave refracted arrival traveltimes from the radial component data.....	44
Figure 4.13. Crossover autopicking process for the left crossover point of shot gather #90 (o) and for the right crossover point of shot gather #100 (*) on the <i>P</i> -wave refractions (median filter window length of 11 samples and differentiation separation length of 3 samples).....	46
Figure 4.14. Crossover autopicking process for the left crossover point of shot gather #90 (o) and for the right crossover point of shot gather	

#100 (*) on the <i>S</i> -wave refractions (median filter window length of 11 samples and differentiation separation length of 3 samples).....	47
Figure 4.15. Crossover point averages of the <i>P</i> -wave refractions for the left trailing (o) and right leading (*) shot spreads.....	48
Figure 4.16. Display of the right crossover point average (*) and left crossover point average (o) for the <i>P</i> -wave refractions.....	48
Figure 4.17. Crossover point averages of the <i>S</i> -wave refractions for the left trailing (o) and right leading (*) shot spreads.....	49
Figure 4.18. Display of the right crossover point average (*) and left crossover point average (o) of the <i>S</i> -wave refractions.....	49
Figure 4.19. <i>P</i> -wave velocity model calculated from the <i>P</i> -wave arrival traveltimes: first layer velocity (+) and second layer velocity (x).....	50
Figure 4.20. <i>S</i> -wave velocity model calculated from the <i>S</i> -wave arrival traveltimes: first layer velocity (+) and second layer velocity (x).....	51
Figure 4.21. Plus time values and statistics for the <i>P</i> -wave refractions.....	52
Figure 4.22. Plus time values and statistics for the <i>S</i> -wave refractions.....	52
Figure 4.23. <i>P</i> -wave depth model and statistics (vertical exaggeration =6).....	53
Figure 4.24. <i>S</i> -wave depth model and statistics (vertical exaggeration =6).....	54
Figure 4.25. Surface consistent static corrections established from the <i>P</i> -wave model: elevation corrections (*), weathering corrections (+), and total corrections (o).....	55
Figure 4.26. Surface consistent static corrections established from the <i>S</i> -wave model: elevation corrections (*), weathering corrections (+), and total corrections (o).....	55
Figure 4.27. <i>P</i> -wave refracted arrival traveltimes versus offset and initial input <i>P</i> -wave model (straight line-slope).....	56
Figure 4.28. <i>S</i> -wave refracted arrival traveltimes versus offset and initial input <i>S</i> -wave model (straight line-slope).....	57
Figure 4.29. First and second layer interface elevation for the <i>P</i> -wave models: PMT method (x) and GLI method (o).....	59
Figure 4.30. First and second layer interface elevation for the <i>S</i> -wave models: PMT method (x) and GLI method (o).....	59
Figure 4.31. Receiver static corrections (weathering + elevation) from the <i>P</i> -models: PMT (x) and GLI (o).....	60
Figure 4.32. Receiver static corrections (weathering + elevation)	

from the <i>S</i> -models: PMT (x) and GLI (o).....	61
Figure 4.33 Shot static corrections (weathering + elevation)	
from the <i>P</i> -models: PMT (x) and GLI (o).....	61
Figure 4.34. Vertical component common receiver stack (raw).....	62
Figure 4.35. Vertical component common receiver stack with the PMT	
static solutions (receiver and shot static corrections from the <i>P</i> -model).....	63
Figure 4.36. Vertical component common receiver stack with the GLI	
static solutions (receiver and shot static corrections from the <i>P</i> -model).....	63
Figure 4.37. Radial component common receiver stack (raw).....	65
Figure 4.38. Radial component common receiver stack with the PMT	
static solutions (receiver static corrections from the <i>S</i> -model and shot	
static corrections from the <i>P</i> -model).....	65
Figure 4.39. Radial component common receiver stack with the GLI	
static solutions (receiver static corrections from the <i>S</i> -model and shot	
static corrections from the <i>P</i> -model).....	66
Figure 4.40. Horizon time structure comparison for a common reflector	
on the radial component data before and after static corrections	
applied (PMT and GLI static solutions).....	66
Figure 4.41 Radial component common source stack (raw).....	67
Figure 4.42. Radial component common source stack with the PMT	
static solutions (receiver static corrections from the <i>S</i> -model and shot	
static corrections from the <i>P</i> -model).....	68
Figure 4.43. Radial component common source stack with the GLI	
static solutions (receiver static corrections from the <i>S</i> -model and shot	
static corrections from the <i>P</i> -model).....	68
Figure A.1. Refracted raypath for a two layers model, i.e. a subweathering	
layer of $z_0$ thickness and low velocity ( $v_0$ ), and a second undefined	
layer of high velocity ( $v_1$ ).....	74
Figure A.2. First-arrivals traveltimes in function of source-receiver offset	
distance based on the two layers model in figure (A.1).....	75
Figure B.1. Plus time analysis according to the “plus-minus”	
method of Hagedoorn (1959).....	76
Figure B.2. Minus time analysis according to the “plus-minus”	
method of Hagedoorn (1959).....	79
Figure C.1. Crossover point averaging editing.....	85

## GLOSSARY

$\theta_c$  : Refracted critical angle ( $\theta_c = \sin^{-1}(V_1/V_2)$ ).

**Delay time:** Time to travel from the receiver to the refractor minus the time necessary to travel the normal projection of the raypath on the refractor.

**Plus time:** Sum of the traveltimes at the receiver from a forward source and the traveltimes at the receiver from the reverse source, minus the traveltimes between the two sources.

**Minus time:** Subtraction of the traveltimes at the receiver from the reverse source of the traveltimes at the receiver from the forward source, minus the traveltimes between the two sources.

**P-wave:** Compressional wave (body wave).

**S-wave:** Shear wave (body wave).

**Rayleigh wave:** Surface wave; retrograde elliptical particle motion; low-velocity and low frequency.

**Converted wave (PS):** "Seismic energy which has traveled partly as a P-wave and partly as an S-wave, being converted from one to the other upon reflection or refraction at oblique incidence on an interface" (Sheriff, 1991).

$V_P/V_S$  : Ratio of the P-wave velocity to the S-wave velocity of a common layer.

**Radial component:** Horizontal component in the in-line direction with the acquisition survey line.

**Vertical component:** Vertical axis perpendicular to the horizontal survey line.

**Anisotropy:** "Variation of seismic velocity depending on the direction in which it is measured" (Sheriff, 1991).

**Surface-consistent:** According to a constant surface location along a survey, only one result is allowed (static correction).

**Traveltime reciprocity:** Traveltime of a seismic wave from source to receiver is equal to the traveltimes in the opposite direction if source and receiver are interchanged.

**Crossover point (CVP) :** Change in the first arrival times between the first layer arrivals and the second layer arrivals.

**Raypath:** Trajectory describes by the normal to the expanded wavefield shell.

**Direct arrivals:** Arrivals traveling along the surface.

**Refracted arrivals:** Arrivals being refracted and traveling along a velocity interface (else than the surface).

**Standard deviation or root mean square error:** "Square root of the average of the squares of the differences between a series of measurements and their mean" (Sheriff, 1991).

**Fold:** Number of redundant determination.

**Offset:** Distance between two locations, example source-receiver offset is the distance between the source and the receiver locations.

**Uphole time:** “Time for the first wave from an explosion to reach the surface at or near the source-point” (Sheriff, 1991).

**Static corrections:** Time shift applied to seismic reflection data to compensate for the elevation and weathering effects (Sheriff, 1991).

**Weathering correction:** Time correction corresponding to the replacement of the weathering layer velocity by another velocity.

**Elevation correction:** Time needed to bring back the receiver or the shot from the surface to a flat datum using a replacement velocity.

**Total correction:** Summation of the weathering and elevation static corrections.

**Subweathering layer:** Surface layer composed of soil or glacial deposits and/or poorly compacted sediments.

**Till:** Moraine deposits composed of mixed sized grains (glacial deposits).

**Glaciolacustrine:** Glacial lake deposits composed mainly of clay.

**Bedrock:** Consolidated rock as oppose to uncompact deposits or sediments (overburden) or soil.

**Cycle-skipping:** Correlation problem due to poor reflector continuity (noncorresponding peaks of a period).

***F-K* filter:** Frequency-wavenumber domain apparent velocity discrimination.

**Common source stacks:** Summation of traces according to the source locations.

**Common receiver stacks:** Summation of traces according to the receiver locations.

## CHAPTER 1 - INTRODUCTION

### 1.1 BACKGROUND

#### 1.1.1 Refraction theory

Seismic refraction events are observed from the propagation of an elastic impulse (through the Earth) across any velocity interface in accordance with the basic Snell's law. The principle of this law is that the sine of the angle of incidence is to the sine of the angle of refraction as the velocity on the first side of the interface is to the velocity on the second side (refractor velocity).

$$\frac{\sin \theta_1}{\sin \theta_2} = \frac{V_1}{V_2} \quad (1.2)$$

where  $\theta_1$  is the angle of incidence,  $\theta_2$  is the angle of refraction,  $V_1$  is the velocity on the first side and  $V_2$  is the refractor velocity.

When the angle of incidence reaches the critical angle ( $\theta_c$ ), the elastic wave is refracted along the interface and again towards the surface according to the same critical angle, which enables the recording of the elastic wave at the surface.

#### 1.1.2 Refraction history

During World War I, seismic energy was studied in the development of sound-ranging equipment used to locate enemy artillery (McGee and Palmer, 1967). Therefore, the idea of using reflected seismic energy to map geological structure soon followed. In 1922, Burton McCollum continued the reflection work and also started research with refraction experiments. The first commercial use of refraction method was in 1924, in Mexico (McGee and Palmer, 1967). Refraction was used to locate an oil reservoir created by a system of faults in limestone (McGee and Palmer, 1967). A refraction method called "fan shooting" was developed and used in 1925 to find salt domes (Weatherby, 1940). The first time the refraction method was used to map refracting interfaces was described by Jones (1934). This method was used to map anticlinal structures. Later, Gardner (1939) introduced a method of mapping subsurface structures using refraction shooting. This method is also known as the "delay time" method. The "delay time" method was further developed by Hawkins (1961) and Barry (1967) (more details in Appendix A).

### **1.1.3 Converted-wave (*PS*) seismic theory**

The use of impulsive source generates an expanding shell of a compression followed by rarefaction (Ricker, 1953). Traditionally, vertical geophones are used to record the compressional energy. However, the presence of inhomogeneities results in the conversion of some compressional wave energy into different wave types. These waves can be called converted-waves and are defined by Sheriff (1991) as “seismic energy which has traveled partly as a *P*-wave and partly as an *S*-wave, being converted from one to the other upon reflection or refraction at oblique incidence on an interface”. The use of multicomponent geophones allows the recording of the compressional seismic energy as well as shear seismic energy.

### **1.1.4 Converted-wave history**

Experiments to obtain shear wave energy using a shear source began in the late 1930's and early 1940's. However, the recording of shear reflections produced by the conversion of incident compressional energy was first reported by Ricker and Lynn (1950). Further investigation of shear waves was reported by Jolly (1956) and the idea of using  $V_p/V_s$  to identify lithology was introduced by Pickett (1963), and further studied by Gregory (1976), Tatham and Stoffa (1976), Domenico (1984), Ensley (1984), Winterstein and Hanton (1985), Robertson and Pritchett (1985), and Anno (1987), as well as Corbin et al. (1987).

## **1.2 THESIS OBJECTIVES**

The near-surface geology in Western Canada is often composed of unconsolidated deposits and low velocity sediments that induce time delays of seismic reflection data. Refraction analysis represents the best way to establish a near-surface model from which static corrections are determined. In this thesis, the Plus-Minus time analysis method, which is based on the “plus-minus” method of Hagedoorn (1959), is developed to build near-surface 2-D models according to the refracted arrivals. The method is used with synthetic data to test its accuracy. Then, the method is used with a three-component dataset from the Blackfoot area. The Blackfoot 2D-3C data allow an amplitude analysis of possible *S*-wave refraction events and the study of the *P-S* reflection geometry. The possibility of solving the time delays that degrade the *P-S* reflections represents a great challenge. To provide a comparison with the Plus-Minus time analysis method, the Generalized Linear Inversion method of Hampson and Russell (1984) was also used.

### **1.3 HARDWARE AND SOFTWARE**

The refracted arrival picking of the Blackfoot data was achieved using the ProMax software, which is an extensive data processing software package. ProMax has also been used to filter and to gain the amplitude of the Blackfoot data, as well as to reverse the polarity of the radial component data. The Plus-Minus time analysis method was coded using the Matlab software. Matlab is a commercial package which provides a technical computing and visualization environment. The Plus-Minus time analysis method under the platform of Matlab was used with the Blackfoot data and the synthetic dataset. Furthermore, the Generalized Linear Inversion refraction static software package (Hampson and Russell) was also used with the same data.

## **CHAPTER 2 - THE PLUS-MINUS TIME ANALYSIS METHOD**

### **2.1 INTRODUCTION**

#### **2.1.1 Purpose of the method**

The Plus-Minus time analysis method has two objectives: to establish a near-surface model of the Earth in terms of subweathering layer thicknesses and seismic wave velocities; and to compute static corrections to be applied to seismic data. The surface layers of the Earth are often made of unconsolidated deposits or soil which have low seismic velocities. For example, in Western Canada the near-surface layers are generally composed of Quaternary glacial deposits (Clague, 1991), while in South America or Africa the surface layers are made of weathered soil materials. These low velocity layers will induce recording delays of seismic reflection data. The impact of these delays on reflector structure can be quite significant. The use of seismic refracted arrivals to establish the thicknesses of these layers and their seismic wave velocities represents one of the best ways to correct for these delays.

#### **2.1.2 Theory**

The refraction analysis method used is the “plus-minus” method of Hagedoorn (1959), which includes the Plus time analysis for depth analysis and the Minus time analysis for velocity determination (van Overmeeran, 1987). The basis of the Plus-Minus time analysis method lies in the traveltimes reciprocity, i.e. the traveltimes of a seismic wave from source to receiver is equal to the traveltimes in the opposite direction if source and receiver are interchanged. The Plus time analysis uses the concept of the Delay time analysis introduced by Gardner (1939, 1967) and further developed by Hawkins (1961) and Barry (1967) (see Delay time analysis in Appendix A). The basic geometry of the Plus-Minus time analysis method is illustrated in Figure 2.1.

To be able to use the Plus time analysis, reciprocal spread data are essential so that the forward arrival spread extends at least to the position of the reverse source ( $S_r$ ) and the reverse arrival spread to the position of the forward source ( $S_f$ ) (Figure 2.1). The Plus-Minus time analysis window is defined by the two crossover points (forward spread ( $X_f$ ) and reverse spread ( $X_r$ )), which determine the offset limit between the first layer arrivals and the second layer arrivals.

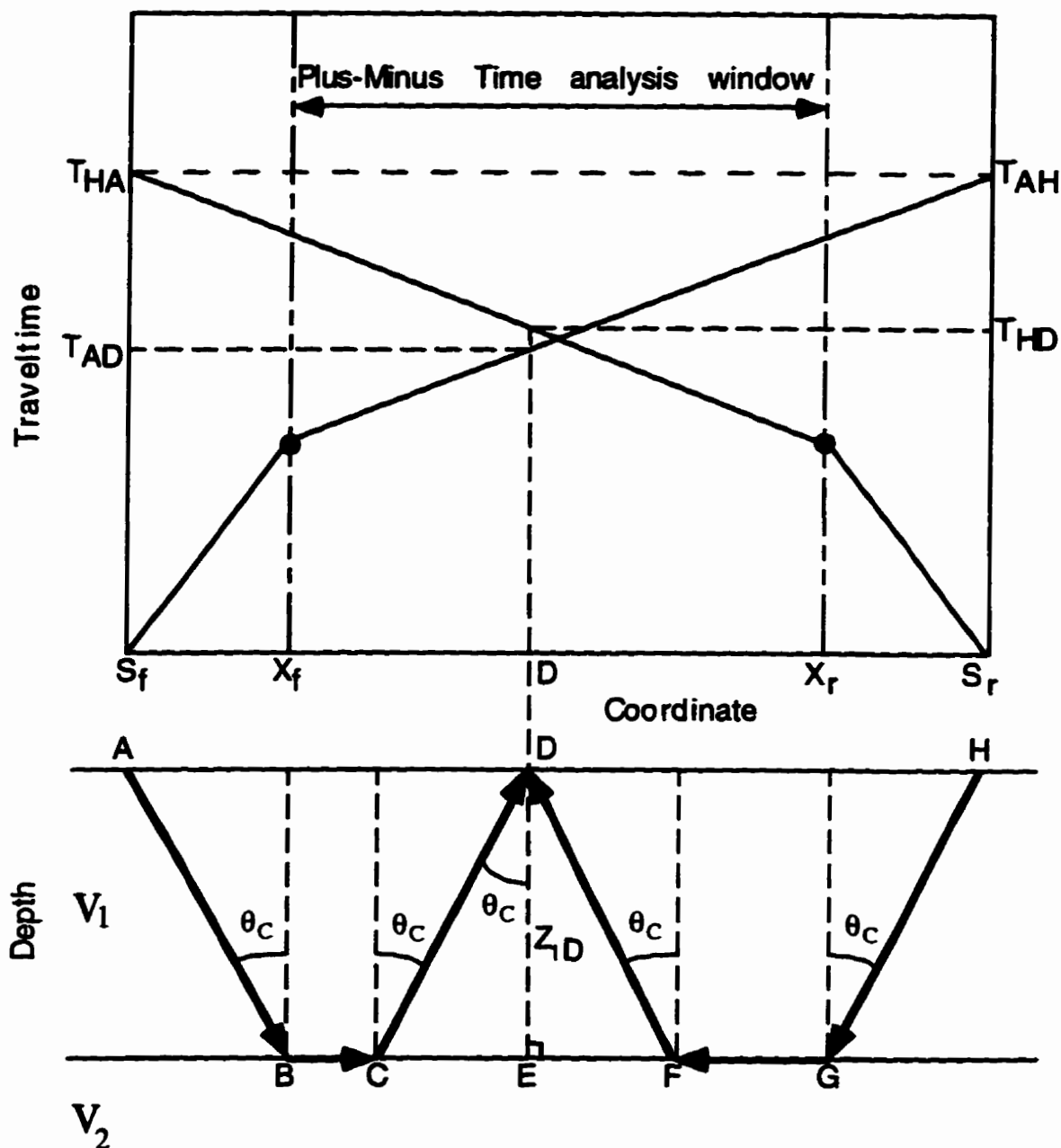


Figure 2.1. Plus time analysis according to the "plus-minus" method of Hagedoorn (1959).

The Plus time value ( $T^+$ ) can be evaluated for each of the receivers inside that window. The Plus time value at a receiver ( $T^+D$ ) is defined (Hagedoorn, 1959) as the sum of the traveltime at the receiver from a forward source ( $T_{AD}$ ) and the traveltime at the receiver from the reverse source ( $T_{HD}$ ), minus the traveltime between the two sources ( $T_{AH}$ ).

$$T^+D = T_{AD} + T_{HD} - T_{AH} \quad (2.1)$$

After some substitution in Equation (2.1) and knowing that the Delay time at receiver D ( $\delta_D$ ) is equal to half the Plus time ( $T^+D$ ) at the same receiver, a relation with the thickness ( $Z_1D$ ) of the first layer below the receiver can be found.

$$Z_1D = [(T^+D) \cdot (V_1)] / 2(\cos(\theta_c)) \quad (2.2)$$

where  $\theta_c = \sin^{-1}(V_1/V_2)$ ,  $V_1$  and  $V_2$  are respectively the first and second layer velocities.

The velocity of the first layer can be found using the inverse slope of the first layer arrivals ( $S_f$  to  $X_f$  and  $S_r$  to  $X_r$ ). From the second layer arrivals (after  $X_f$  for the forward spread and after  $X_r$  for the reverse spread), the second layer velocity can be derived using the Minus time analysis (Figure 2.2).

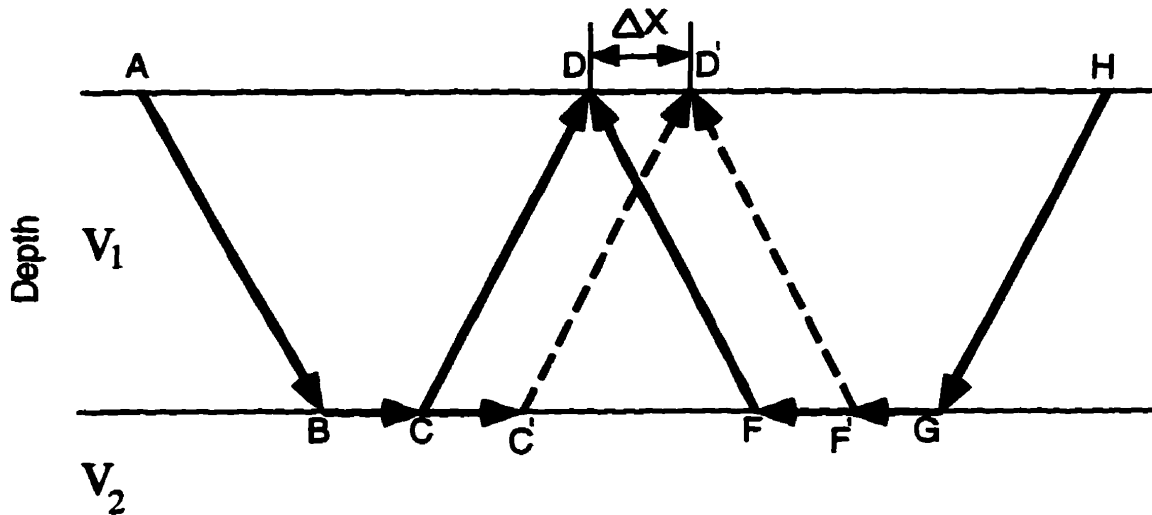


Figure 2.2. Minus time analysis according to the “plus-minus” method of Hagedoorn (1959).

The definition of the Minus time ( $T^-D$ ) at a receiver is the subtraction of the traveltime at the receiver from the reverse source ( $T_{HD}$ ) of the traveltime at the receiver from the forward source ( $T_{AD}$ ), minus the traveltime between the two sources ( $T_{AH}$ ).

$$T^-D = T_{AD} - T_{HD} - T_{AH} \quad (2.3)$$

A velocity analysis of the second layer can be undertaken using the Minus time values at two receivers ( $D$  and  $D'$ ) with a specified separation distance ( $\Delta X$ ).

$$T'D' - T'D = \Delta T'D = 2(\Delta X)/V_2 \quad (2.4)$$

The velocity of the second layer ( $V_2$ ) is equal to twice the inverse slope of a best fit line through the Minus time variations ( $\Delta T'D$ ) calculated for receivers inside the Plus-Minus time analysis window.

$$V_2 = 2(\Delta X)/\Delta T'D \quad (2.5)$$

### *Summary*

Knowing the Plus time values, the first and second layer velocities at each receiver, the thickness of the first layer below each receiver can be found according to the Delay time analysis. For more details about the Plus time and Minus time analyses, see Appendix B. The Delay time represents the time to travel from the receiver to the refractor minus the time necessary to travel the normal projection of the raypath on the refractor (Figure 2.1). From Snell's law, a relation between the Delay times and the thickness of the first layer at the receiver can be established. Finally, the link between the Delay times and the Plus times allows us to determine the thickness of the first layer below each receivers inside the Plus-Minus time analysis window (Equation 2.2). This will allow the determination of the first layer thickness all along a seismic survey line. Therefore, this analysis is restricted to a two layer case in two dimensions. The first layer velocity can be evaluated using a polynomial fit of the direct arrival or a rough estimate of the subweathering layer (first layer). The knowledge of the first layer thickness and velocity allows the determination of surface-consistent weathering static corrections, where the replacement velocity is the average refractor velocity.

### **2.1.3 Hardware/software requirement**

The Plus-Minus time analysis software is written in the Matlab language. Matlab is a commercial package which provides a technical computing and visualization environment. A Matlab license is required to run the Plus-Minus time analysis software. Currently, arrival times and geometry are input from ProMax exported database files. The refracted arrival times are previously picked in the processing software (currently ProMax) and then input to the Plus-Minus time analysis software. The geometry files include the receiver coordinates and elevations, and the shot coordinates and elevations, as well as the uphole time (see data files section in Appendix C). The software can be run on any platform for

which Matlab is available, including UNIX, MS-Windows, and Macintosh (see PMT method implementation in Appendix C).

## **2.2 PROCESS**

### **2.2.1 General flow chart**

The Plus-Minus time analysis method developed for this thesis consists of seven major steps and four optional steps (Figure 2.3). As explained in the data file section (Appendix C), the refracted arrivals and the geometry files are required to properly initiate the processing. There are three final results of processing; a velocity model, a depth model, and the static corrections.

After the data are loaded, the inflection points on the refracted arrivals are identified. These are called crossover points (CVPs). The crossover points represent a change in the first arrival times between the first layer arrivals and the second layer arrivals. Once the locations of the crossover points are known for each source arrival spread, the velocities of the first layer can be calculated using a polynomial fit of the direct arrivals. The second layer velocities are calculated using the Minus time analysis with the refracted arrivals.

Simultaneously, the time delays caused by the downgoing and upgoing refracted wave raypath through the first layer can be determined using Plus time and Delay time analyses of the refracted arrivals. Once the Plus times and the two layer velocities are known, the first layer thicknesses are computed in the depth calculation processing step. Finally, from the first layer thicknesses and velocities, the static corrections which determine the effect of that layer, can be found using the static computation processing step.

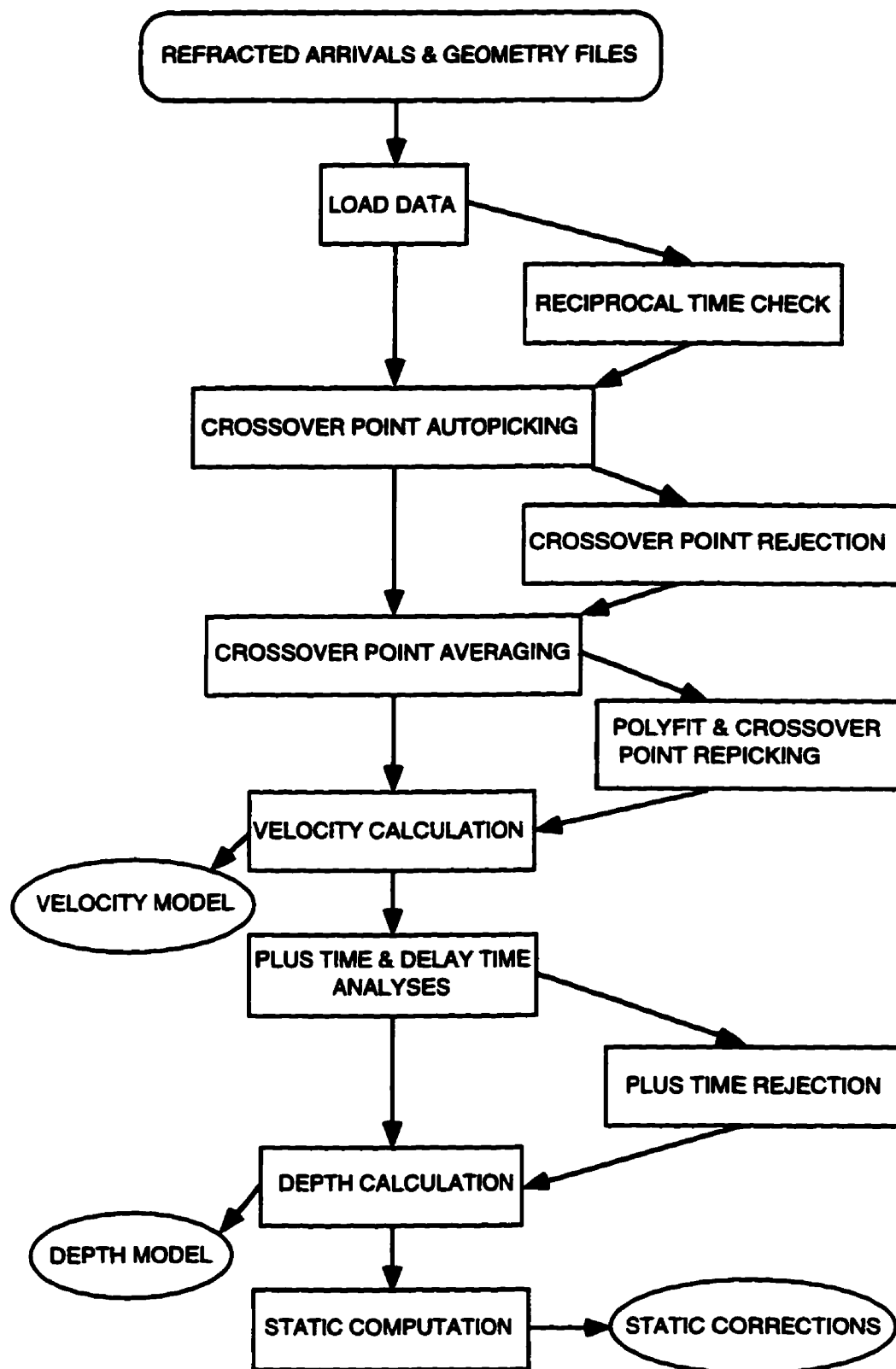


Figure 2.3. Processing flow chart

### **2.2.2 Reciprocal time check**

As mentioned in the theory section, the basis of the Plus-Minus time analysis method lies in the traveltime reciprocity, i.e. the traveltime of a seismic wave between two locations in one direction is equal to the traveltime in the opposite direction. For example, if seismic energy is sent from a shot and recorded at a certain distance by a receiver, the shot and receiver position may be switched, but the traveltime recorded in both cases should be equal.

The first step after loading the data is to check if the traveltime reciprocity is valid. The reciprocal time check process will determine the traveltime difference for all possible shot pairs, i.e. the two shot spreads have overlapping receivers at the pairing shot location. Figure 2.4 shows two generalized shot gathers where the receiver spread of the  $i$ th shot overlaps the receiver spread of the  $j$ th shot. It can be noted that the traveltime of the forward spread arrivals at the reverse shot location is equal to the traveltime of the reverse spread arrivals at the forward shot location. The subtraction of the two traveltimes equals zero and the traveltime reciprocity is correct.

With real data, however, the traveltime reciprocity is generally not respected due to slight separations between shots and receivers at the same station, and also to arrival picking errors. Also, if dynamite is used, the source is often buried below the surface to variable depth. Therefore, the uphole time, which is the time taken by the seismic energy to travel back up to the surface, should be added before the reciprocity is verified. The reciprocal time check process allows the user to identify the shot pairs with reasonable reciprocal traveltime differences and the problematic shot pairs. There are several possibilities to solve the problem of shot pairs with significant reciprocal traveltime differences: first a review and correction of the arrival picking errors in the processing software used to create them; second the problematic shot pairs can be ignored in the subsequent process; third the reciprocal traveltime difference of a problematic shot pair can be used to adjust the arrival traveltimes of one of the shots according to the pairing shot (bulk shift).

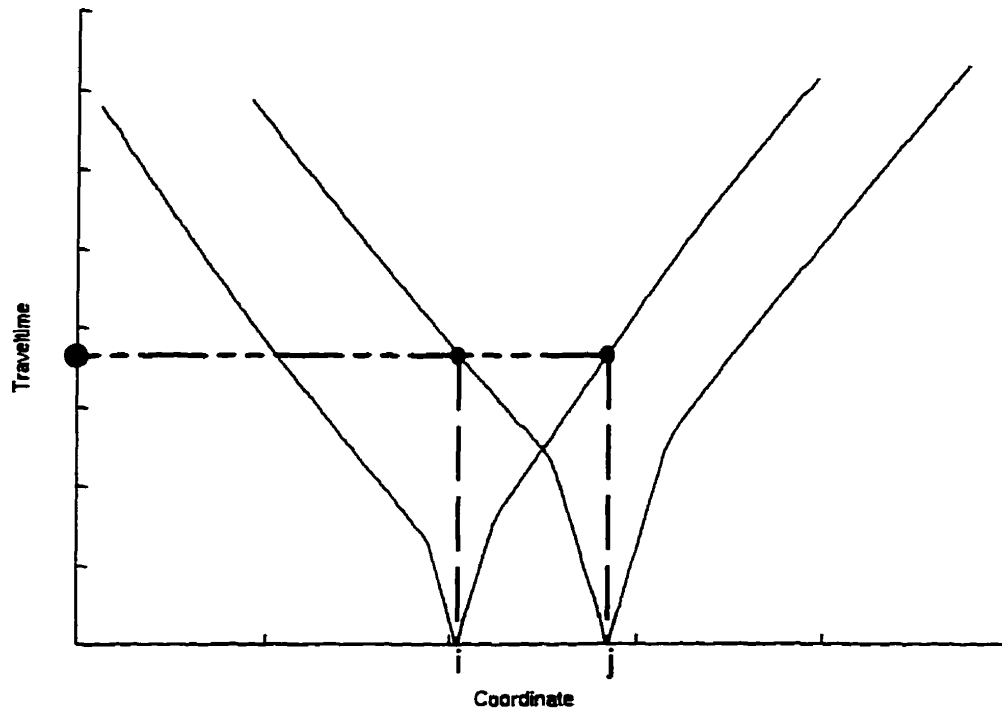


Figure 2.4. Reciprocal time check with shot gathers i and j.

### 2.2.3 Crossover point autopicking

Crossover point picking represents the most important step of this program. The crossover points indicate a change in the arrivals between the first and second layer. At the crossover point, the traveltime of the second layer arrivals is equal to the traveltime of the first layer arrivals. Beyond the crossover point, the refracted arrivals from the second layer are recorded before the first layer arrivals. The first layer arrivals (also called direct arrivals) are the traveltimes of a seismic wave from the source to the receivers along the surface of the first layer. The second layer arrivals (also called refracted arrivals) are the traveltimes of a seismic wave from the source to the bottom of the first layer then along the first and second layer interface and back up through the first layer to the receivers (Figure 2.5).

The position of the crossover points on each shot spread is found using the traveltime difference analysis developed by Lawton (1989) and the branch point analysis of Wang and Cheadle (1995). The traveltime difference analysis consists of subtracting two adjacent shot arrival traveltimes at common receiver locations (Figure 2.6). The traveltime differences ( $\delta t$ ) remain constant when the arrivals from the two shots involve the same layer. The crossover point is located at the limit between a constant traveltime difference

and an increasing or decreasing traveltime difference. For example, if we subtract the traveltime of two overlapping shot gathers (Figure 2.6), it can be noticed that the traveltime difference on the left of shot  $i$  location is constant until it reaches the left crossover point of the shot gather  $i$  and then the traveltime difference increases. On the other side (right of shot  $j$  location), the traveltime difference decreases until it reaches the right crossover point of shot gather  $j$  and then remains constant. Then, if we calculate the first and second derivatives of the traveltime differences, the crossover point locations correspond to the maximum value of the second derivative. This result is due to a maximum change of slope on the traveltime differences at the first and second layer inflection point and allows automatic crossover point location picking for each overlapping shot pair spread. The use of all possible overlapping shot pairs allows not only the identification of the crossover point (left and/or right) on each shot gather but also a statistically redundant crossover point location on the same shot spread (left or right).

Another important feature of the traveltime difference analysis is the cancellation of traveltime irregularities due to topographic features. However, in the real data case, traveltime irregularities can also be due to errors in the arrival picking and other instrumental factors, so that filtering is essential. A median filter is first applied to the traveltime difference to remove high-frequency variation and keep the general trend of the traveltime difference, especially the step trend at the crossover point. After the first derivative is calculated, a mean filter can be applied to smooth the short wavelength variations due to small steps in the median filtered traveltime difference curve, and keep the long wavelength variation due to major steps associated with the crossover point locations. The mean filter should be used with care and only if the first derivative curve appears noisy. The window length of these filters is determined by the user and should be tested on each dataset. Also, the first and second derivatives use a parameter called differentiation separation length, which can be defined by the user. This parameter determines the number of samples in between each subtraction for the derivation. For example if one is used the differentiation of the traveltime difference curve corresponds to its simple derivative, i.e. the sample interval is one.

$$\Delta t/\Delta x = [t(x + n\Delta s) - t(x)]/n\Delta s \quad (2.6)$$

where  $x$  and  $\Delta x$  are respectively the coordinate of the arrival and the coordinate variation;  $t$  and  $\Delta t$  are respectively the time of the arrival and the time variation; and  $\Delta s$  is the distance of a sample interval, while  $n$  is the differentiation separation length factor.

The window filter length and the differentiation separation length need to be tested on each different dataset to optimize the crossover point autopicking consistency. This will reduce the amount of manual editing of the crossover points.

Finally, the user can specify an offset range in which the crossover points can be picked. This feature should be used only if the user has sufficient knowledge of the data (near-surface geology, previous identification of some crossover points throughout the entire survey) and can confine the crossover points within a certain offset range from the shot locations. It can also be used if third layer arrivals are suspected at a larger offsets, so that the crossover points might be divided between the first and second layer inflections and the second and third layer inflections. In both cases, the offset range limitation will enable consistent crossover point picking and will save a lot of manual editing.

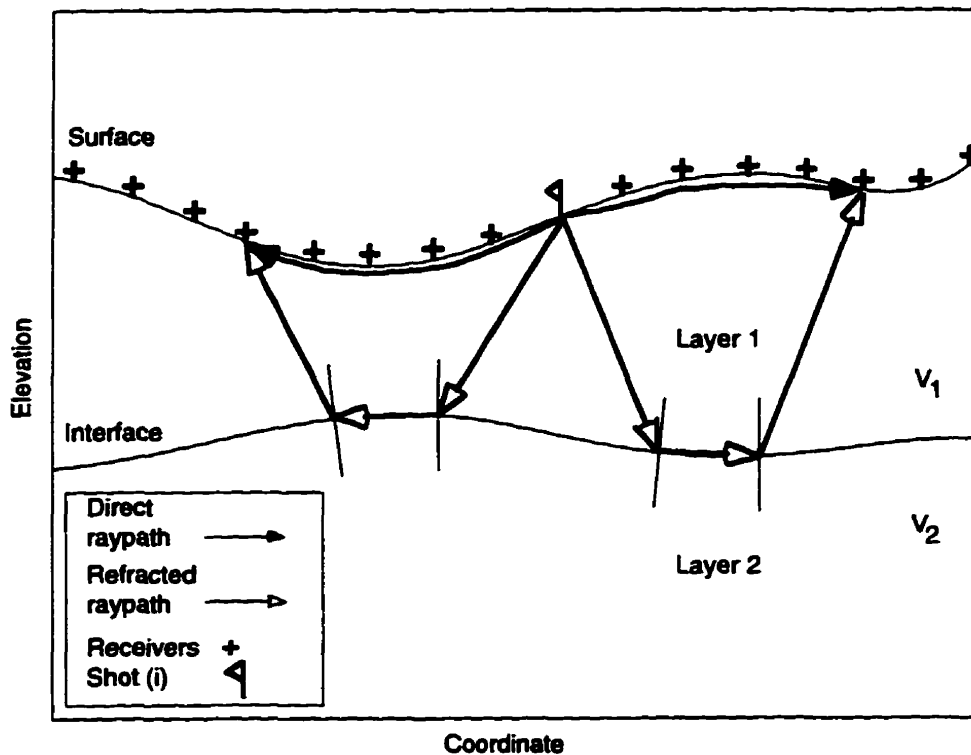


Figure 2.5. Direct and refracted raypath for shot gather i.

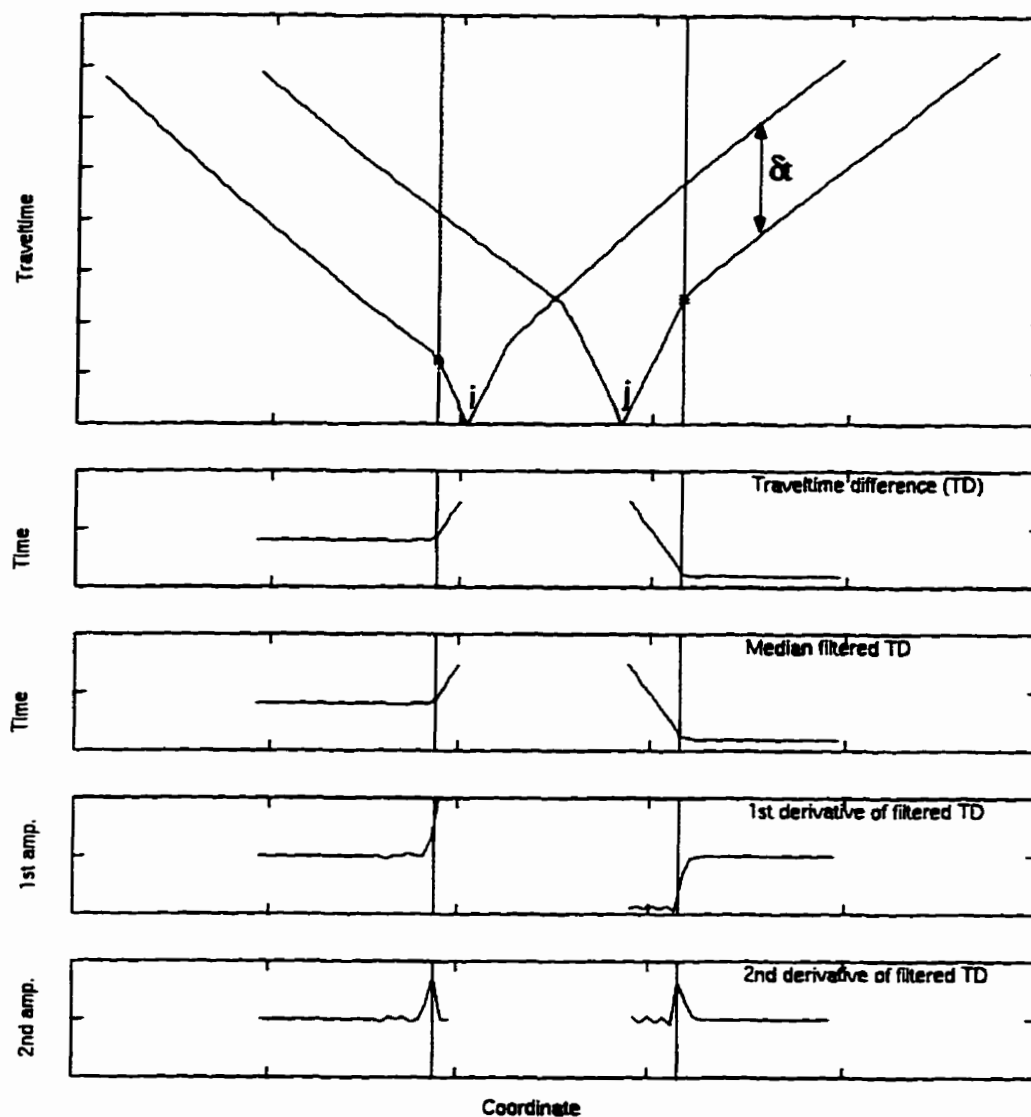


Figure 2.6. Crossover point autopicking of the left crossover point for shot gathers  $i$  (o) and of the right crossover point for shot gather  $j$  (\*), according to the traveltime difference analysis by Lawton (1989) and the branch point analysis of Wang and Cheadle (1995).

### 2.2.3 Crossover point rejection

This optional process is based on the statistics of the crossover points previously picked. As mentioned in the above section, the use of all possible overlapping shot pairs brings an over determination of the crossover point on a shot spread. The next step is to average all the crossover points that belong to the same shot spread (forward or reverse) and use that value in the subsequent process. The subtraction of each possible overlapping shot spread with a common shot spread should result in consistent traveltime differences and same crossover point surface location. However, if the arrivals are inconsistent and

noisy due picking problem, the traveltimes difference of each overlapping shot spreads might result in different crossover point locations. The utility of the crossover point rejection is to identify and remove the crossover point picks for a given shot spread that have a high deviation from the average crossover point value.

The rejection can be based on a fraction of the standard deviation of the crossover point picks for each shot spread or on a constant deviation limit. The difference between the two rejection limits is that the fraction of the standard deviation limit changes for each crossover point shot spread (right or left) and the constant deviation limit remains constant for all crossover point shot spreads. In both cases, the use of the crossover point statistics, which includes the standard deviation, the fold and the value of the crossover point averages, is recommended to determine the rejection limit. The user should look not only at the average crossover point values, but at the standard deviation and at the fold of each crossover point average. The combination of a high standard deviation with a low fold indicates a crossover point autopicking problem and manual editing might be required, while a low standard deviation with either a high or low fold generally indicates a successful crossover point autopick. In the case of a high standard deviation and a high fold, the crossover point autopicking was noisy, and the crossover point rejection might help remove some bad crossover picks. One thing to keep in mind is that each time crossover point rejection is used, the redundancy (fold) of the crossover point averages is reduced.

#### **2.2.4 Crossover point averaging**

The next major step after the crossover point autopicking is the averaging of all the crossover points for a shot spread (left and/or right). For a shot with a leading (right) and a trailing (left) spread, two individual averaging processes are required; one for the left crossover points and one for the right crossover points. In Figure 2.7, the left crossover points of shot gather *j* comes from the traveltimes difference analysis of its left (trailing) spread with all overlapping left shot spreads to its right, whereas in Figure 2.8, the right crossover points of shot gather *j* come from the traveltimes analysis of its right (leading) spread with all the overlapping right shot spreads to its left. The proper crossover point positioning is important for the velocity calculation and the Plus time analysis. The crossover points can be edited individually before the crossover point averages are computed. The crossover point averages can also be edited (see PMT method implementation in Appendix C).

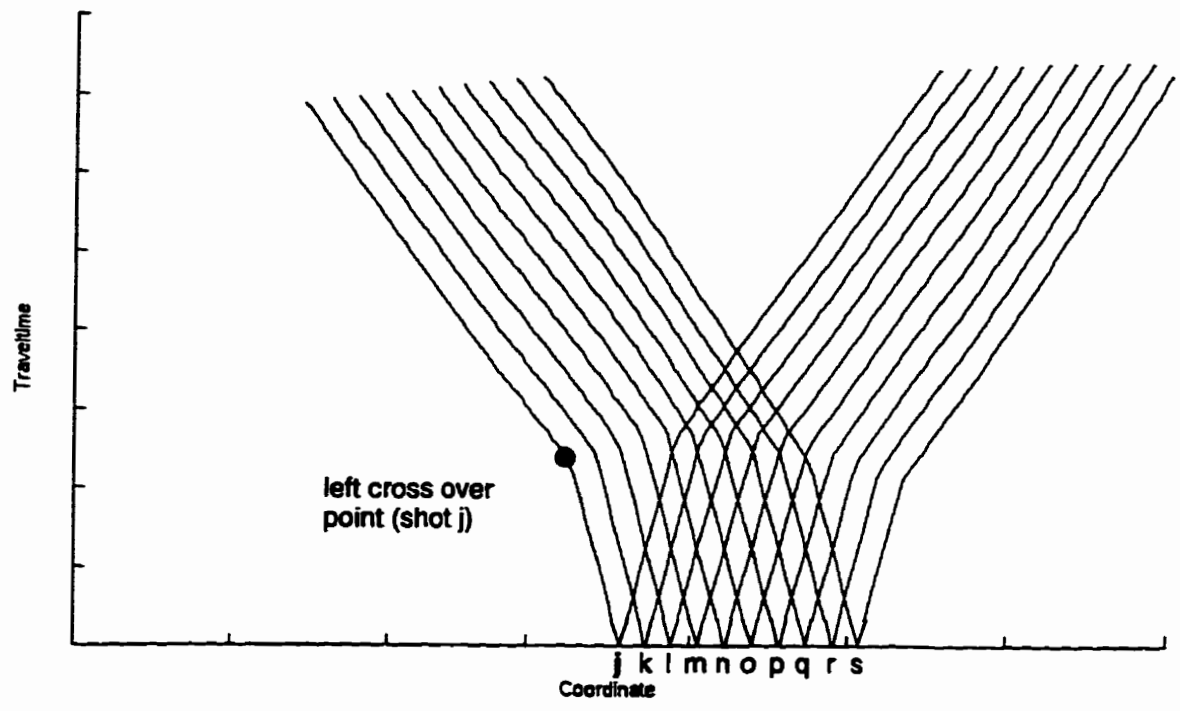


Figure 2.7. Left crossover point determination for shot gather j, established from the overlapping shot spread to the right .

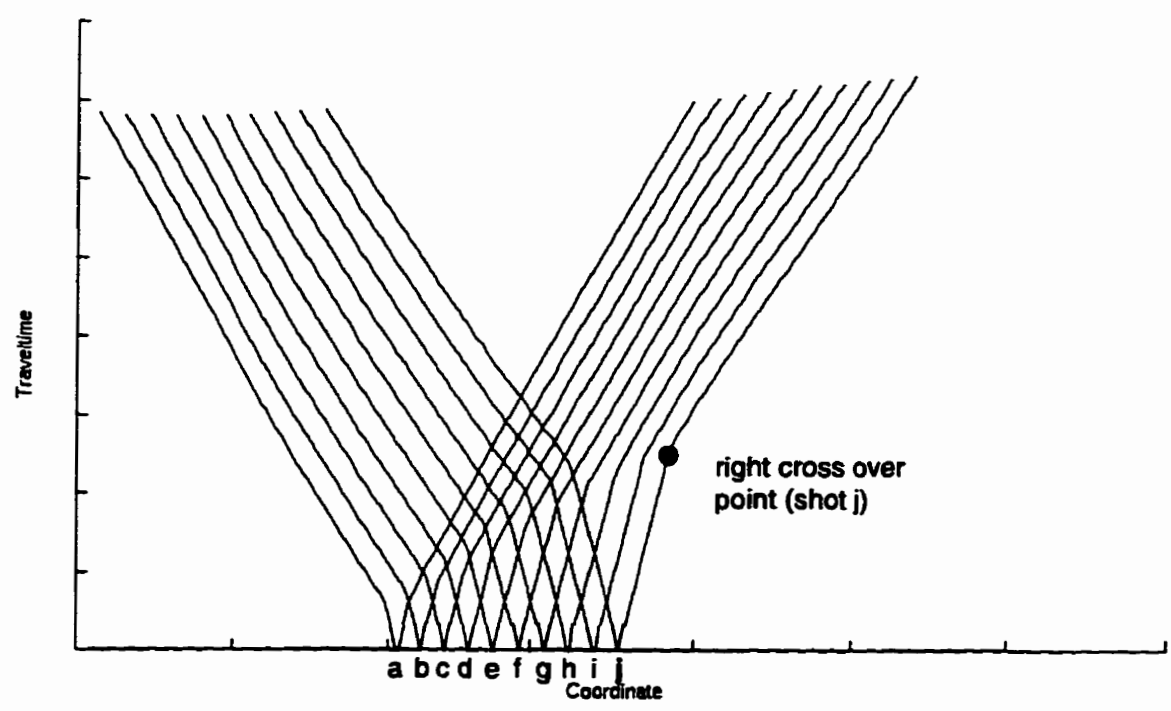


Figure 2.8. Right crossover point determination for shot gather j, established from the overlapping shot spread to the left.

### **2.2.5 Polyfit and crossover point repicking**

This optional process has the objective of obtaining a better crossover point consistency between shot spreads. In fact, the offset distance of the crossover point average of a shot spread from the shot location should not be too different than the offset distance of the crossover point average on the next shot spread from its location. The offset distances between the crossover point averages and their shot locations reveal the general shape of the first layer thickness. Generally, the offset varies proportionally with the variation of the first layer thickness and illustrates its long wavelength shape. If there is an abrupt crossover point average offset change from adjacent shot spreads, it might indicate a crossover point picking problem depending on the distance between their shot locations. The user can solve the problem by editing each crossover point that enters into the crossover point average location or edit directly the crossover point average location (see PMT method implementation in Appendix C). Another way to resolve this problem is to fit a polynomial curve through the crossover point average offset values and repick all the crossover points entering in the average that lie outside a certain deviation from the polynomial curve. Two parameters are defined by the user: the first one is the polynomial degree for the polynomial curve (polyfit curve) and the second one is the deviation limit from the polyfit curve. The polynomial degree determines the amount of complexity in the polyfit curve, i.e. the higher the polynomial degree, the more complex the polyfit curve can be. This parameter should be tested first until the polyfit curve follows the general trend of the crossover point average offsets.

The deviation limit parameter is specified according to the tolerated distance between the crossover point average offsets and the polyfit curve. The deviation limit is determined according to the user interpretation. However, the user should know that the crossover point repicking process will be constrained within an offset range, which is the polyfit curve plus the deviation limit, and the polyfit curve minus the deviation limit. For a small deviation limit, the constraint on crossover point repicking is important, so that the crossover point average offset curve will closely follow the polyfit curve. The user should be concerned about influencing the crossover point repicking process too much, unless he or she has a sufficient knowledge of the data.

### **2.2.6 Velocity calculation**

Once the crossover point average locations are known, then the velocities of the first and second layer can be calculated. A polynomial fit of the direct arrivals will enable the determination of the first layer velocity, while the Minus time analysis of the refracted arrivals will establish the second layer velocity. For a given shot gather, with a leading and a trailing spread, the velocity of the first layer at the shot location is given by the inverse slope of the two direct arrival segments (leading and trailing). The direct arrivals segments are limited by the shot location and the crossover point locations (Figure 2.9). The slope of the direct arrivals is found using a best fit straight line (one degree polynomial fit). Then, the first layer velocity at the shot location corresponds to the average inverse slope of the two direct arrival segments. Finally, the first layer velocity values at each surface station between shotpoints are interpolated.

The second layer velocity is found using Minus time analysis on the refracted arrivals within the Plus-Minus time analysis window (Figure 2.9 and equation 2.5). The Minus time values are calculated for each receiver location inside the Plus-Minus time analysis window. Then, the Minus time variations ( $\Delta T_D$ ) are displayed as a function of twice the receiver separation ( $2\Delta x$ ) (Figure 2.10).

Finally, a straight line is fit through the Minus time variation values, with the inverse slope of it corresponding to the second layer velocity. The second layer velocity value belongs at the half-way location in the Plus-Minus time analysis window, which is defined by the right crossover point of the shot gather  $i$  and the left crossoverpoint of the shot gather  $j$ . After all the possible Plus-Minus time analysis windows (different shot pairs) have been used, an average of all the second layer velocity values at the same location is calculated, followed by interpolation to the receiver locations. Both first and second layer velocities can then be edited manually and median filtered to remove the high frequency variation and any bad velocity values (see PMT method implementation in Appendix C).

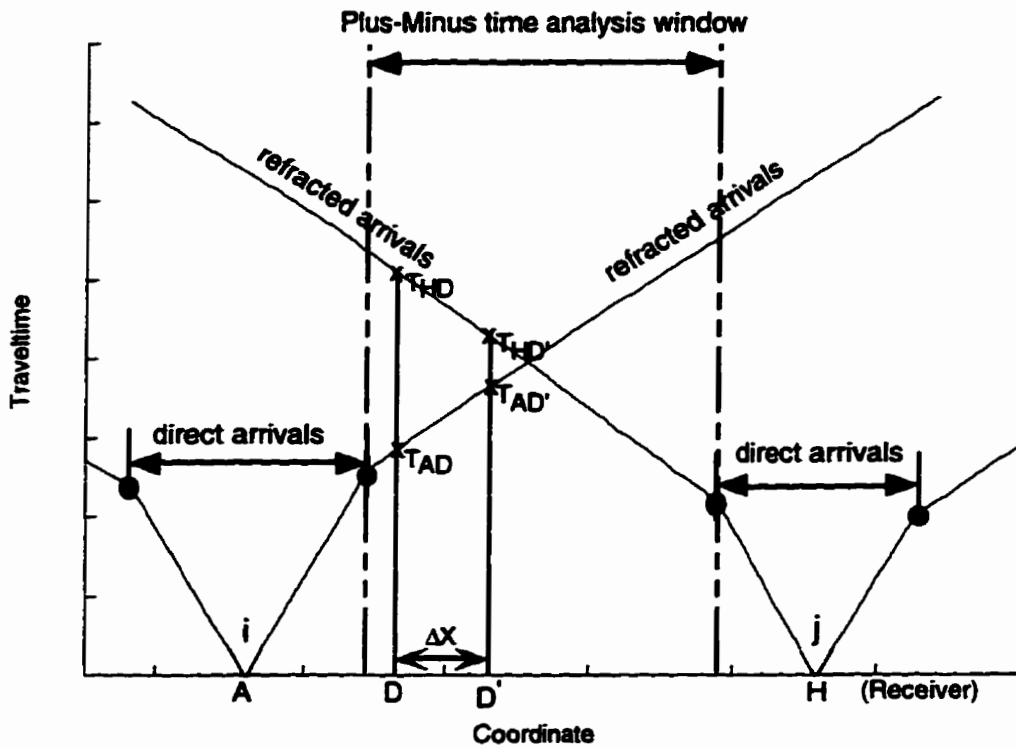


Figure 2.9. Shot gathers i and j with their left and right crossover points, and the Plus-Minus time analysis window .

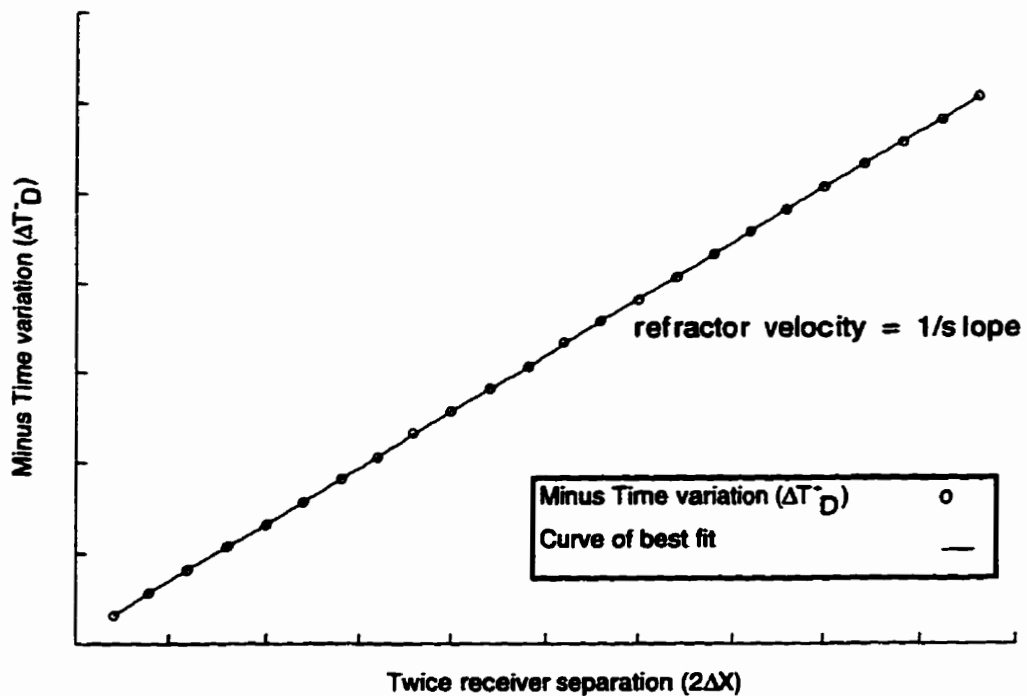


Figure 2.10. Minus time variation displayed in function of twice the receiver separation ( $2\Delta x$ ) and best-fit straight line.

### 2.2.7 Plus time and Delay time analyses

The Plus time analysis process, like the velocity calculation, requires the determination of the crossover point average locations. As explained in the theory section, the Plus time analysis uses the Delay time analysis concept to calculate the thickness of the first layer below each receiver. This process calculates the Plus time values that are going to be used for the first layer thickness computation in the depth calculation process. The Plus time analysis computes the Plus time values for each receiver within all the possible Plus-Minus time analysis windows (use of different shot pairs). All the Plus time values are stored under the associated receiver locations. The use of all the possible overlapping shot spreads allows a redundant determination of the Plus time values at each receiver location. This is important to reduce the effect of noisy data and bad picks. Some of the Plus time values can be rejected according to their deviation from the average Plus time value at a receiver location (see Plus time rejection section). As mentioned previously, the Plus time analysis process needs the crossover point average locations. Some of the crossover point averages may be missing, because they have been deleted or not computed. In this case, they need to be interpolated from the other crossover point average values or the shot spread without a crossover point average value will not be used in the Plus time analysis process. Also, if the presence of third layer arrivals is known, these arrivals can be excluded from the Plus time analysis computation by simply limiting the offset range.

The Plus time analysis cannot be used to determine the Plus time values for the receivers outside the Plus-Minus time analysis window limit (Figure 2.11). Therefore, the Delay time analysis is computed for these receivers (Figure 2.12) (Lawton, 1989). The Delay time value at a receiver can be expressed as:

$$\delta_r = T_r - \delta_s - X/V_2 \quad (2.7)$$

where  $T_r$  is the refracted travelttime at the receiver,  $\delta_s$  is the shot Delay time,  $X$  is the distance between the shot and the receiver, and  $V_2$  is the second layer velocity.

The shot Delay time ( $\delta_s$ ) is equivalent to half the Plus time value at that surface location and the receiver delay time can be multiplied by two to obtain the Plus time value at this surface location. So, the Plus time analysis has to be computed prior to the use of the Delay time analysis. Also, the second layer velocity has to be already calculated or known. The use of the Delay time analysis in conjunction of the Plus time analysis allows the determination of the Plus time values at each surface location.

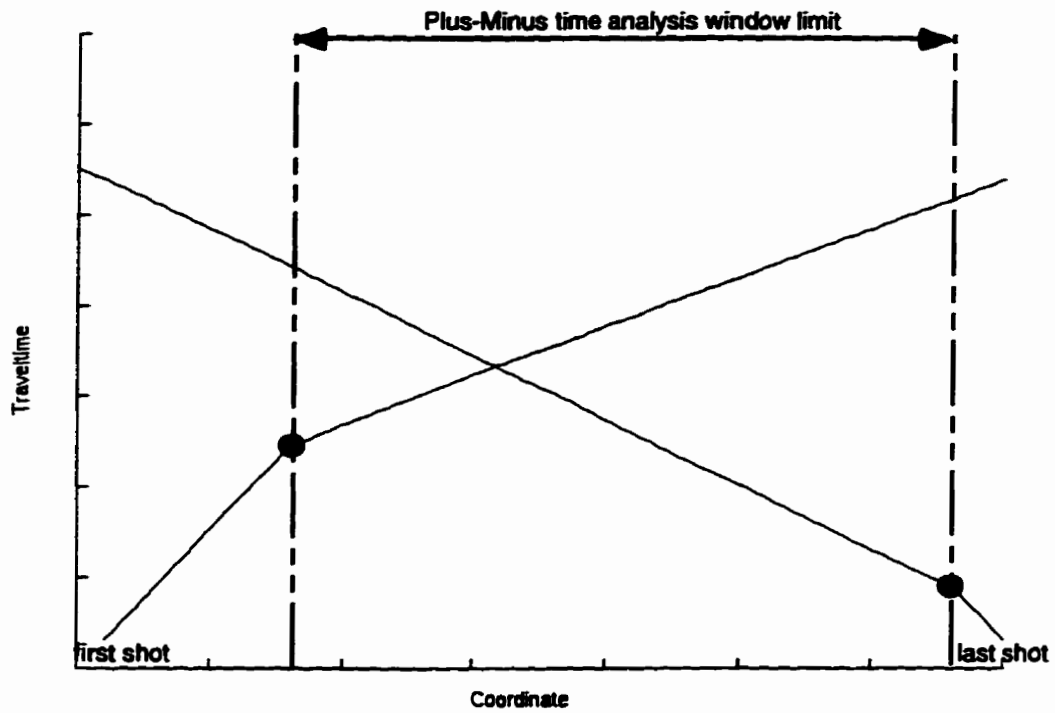


Figure 2.11. Plus time analysis limitation.

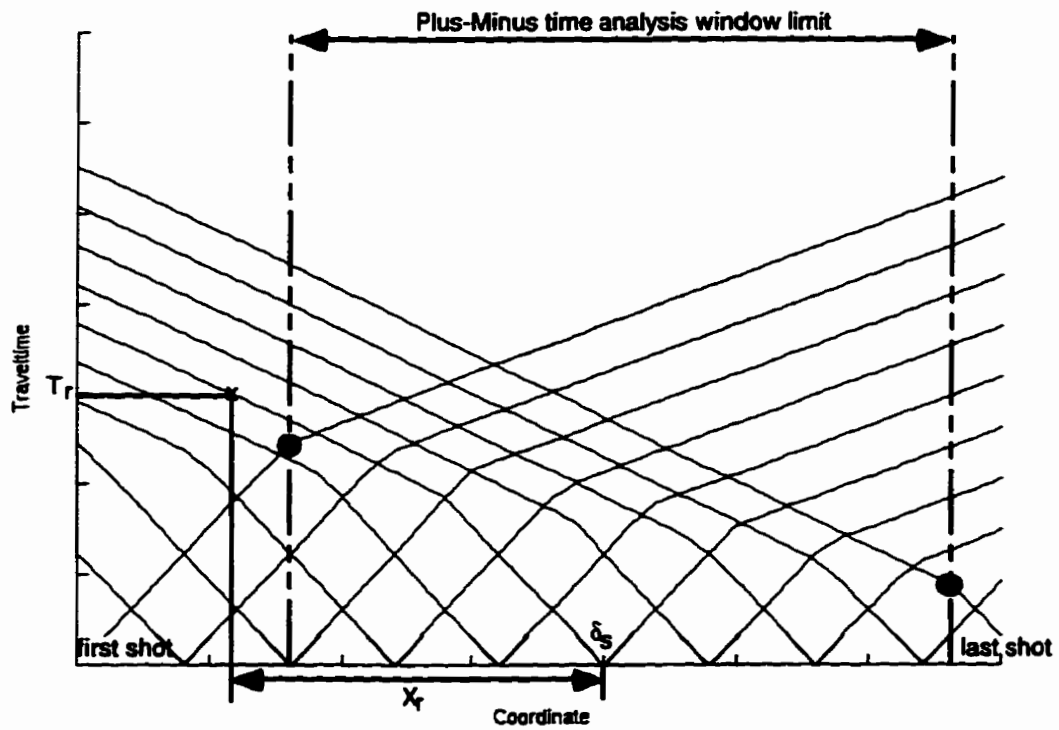


Figure 2.12. Delay time analysis for receiver locations outside the Plus-Minus time analysis window limit.

### 2.2.8 Plus time rejection

The Plus time rejection process is similar to the crossover point rejection in terms of the statistical rejection concepts. The rejection can be done according to a constant deviation limit or according to a fraction of the standard deviation limit. The constant deviation limit remains unchanged for all the receiver locations, while the standard deviation changes for each receiver location. At each receiver locations, the Plus time average value, the standard deviation and the fold are known and can be evaluated. The Plus time average curve should have a reasonable long wavelength trend combined with short wavelength variations. If a Plus time average value is completely out of the range of the other Plus time average values and the standard deviation for this Plus time average value is high, it reveals that there are some bad Plus time values entering into the Plus time averaging at this receiver location. In general, high standard deviation indicates the presence of bad Plus time values, which can be rejected using the Plus time rejection process. Again, like the crossover point rejection, the Plus time rejection process will reduce the redundancy (fold) of the Plus Time averages. The Plus time rejection process should be used before the Delay time analysis computation.

### 2.2.9 Depth calculation

After the Plus time analysis is completed, the Plus Time average values at each receiver are calculated. At this stage, the first and second layer velocity at each receiver, as well as the Plus time average, should be known. The calculation of the first layer thickness below each receiver is based on the delay time analysis concept (Equation 2.2). Before the depths are calculated, the user has to make sure that the Plus time average values are consistent and that the two layer velocities are reasonable, i.e. no noisy short wavelength variations and the first layer velocity is not greater than the second layer velocity. The Plus time average values, and the first and second layer velocities are needed to evaluate the thickness of the first layer below each receiver (Figure 2.13 and Equation 2.8). The first layer thickness can be manually edited or median filtered before the static corrections are computed to reduce the high frequency noise (see PMT method implementation in Appendix C).

$$Z_1 = [(T^+)*(V_1)]/2(\cos(\theta_c)) \quad (2.8)$$

$$\text{where } \theta_c = \sin^{-1}(V_1/V_2)$$

### 2.2.10 Static computation

The final process computes the static corrections to be applied to the seismic data. The corrections are for the weathering layer (first layer) and for the surface elevation variation (topography). The weathering correction will cancel the time delays produced by the first low velocity layer. The elevation correction will bring the shots and the receivers to a common flat datum. The static computation process is based on the depth and velocity model and will calculate the receiver static corrections and shot static corrections based on surface-consistent static corrections.

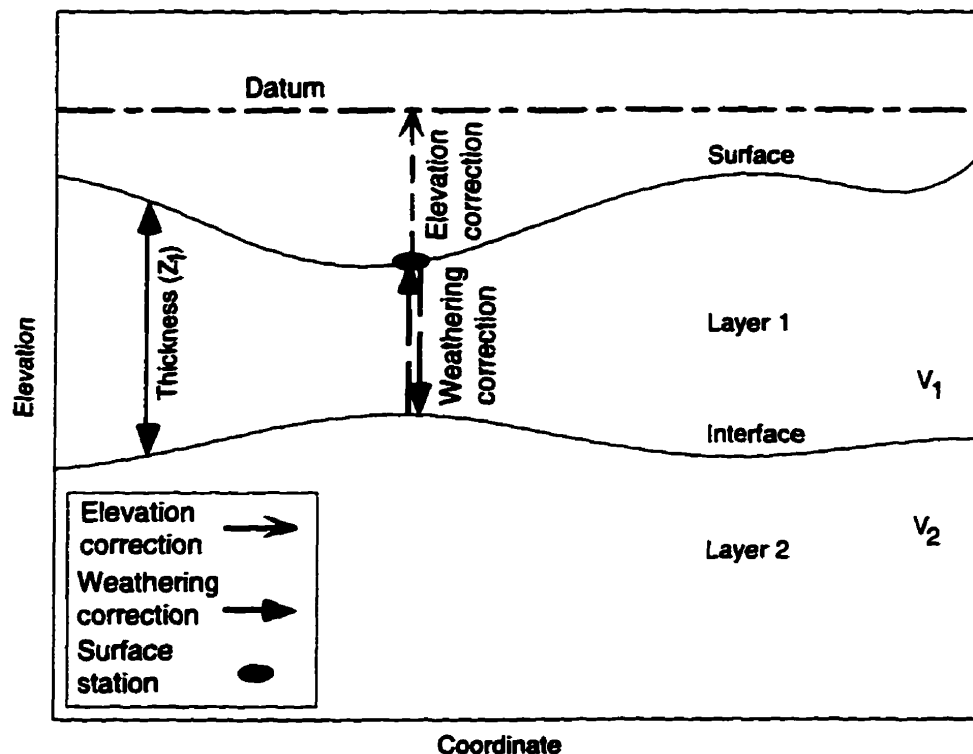


Figure 2.13. Surface-consistent static corrections including elevation and weathering static corrections for a 2 layer model.

#### *Weathering correction*

The weathering correction corresponds to a time correction which essentially replaces the weathering layer velocity with the second layer velocity (Figure 2.13). If the shot is buried below the surface, the uphole time is used to bring the shot back to the surface (before the weathering correction is applied). Then, the shot or the receiver is brought back to the surface using the replacement velocity. The replacement velocity is normally chosen to be the second layer velocity, either the local or average value.

The weathering static correction ( $\Delta t_w$ ), for a shot or a receiver can be expressed as follows:

$$\Delta t_w = -Z_1/V_1 + Z_1/V_{rep} + T_{uh} \quad (2.9)$$

where  $Z_1$  is the first layer thickness,  $V_1$  is the first layer velocity,  $V_{rep}$  is the replacement velocity used, and  $T_{uh}$  is the uphole time.

#### *Elevation correction*

The elevation correction ( $\Delta t_e$ ) corresponds to the time needed to bring back the receiver or the shot from the surface to a flat datum using the replacement velocity (both flat datum and replacement velocity are user defined).

$$\Delta t_e = (H_d - H_s)/V_{rep} \quad (2.10)$$

where  $H_d$  is the datum elevation, and  $H_s$  is the surface elevation.

#### *Total correction*

Finally, the total correction ( $\Delta t$ ) is a summation of the weathering and elevation static corrections. The total static correction for a shot or a receiver can be expressed as follow:

$$\Delta t = \Delta t_w + \Delta t_e \quad (2.11)$$

$$\Delta t = -Z_1/V_1 + Z_1/V_{rep} + (H_d - H_s)/V_{rep} \quad (2.12)$$

## CHAPTER 3 - SYNTHETIC DATASET

### 3.1 INTRODUCTION

#### 3.1.1 Initial model

A synthetic model has been designed to test the Plus-Minus time analysis method developed. The model consists of two layers with a first layer velocity of 650 m/s ( $V_1$ ) and a second layer velocity of 1600 m/s ( $V_2$ ) (Figure 3.1).

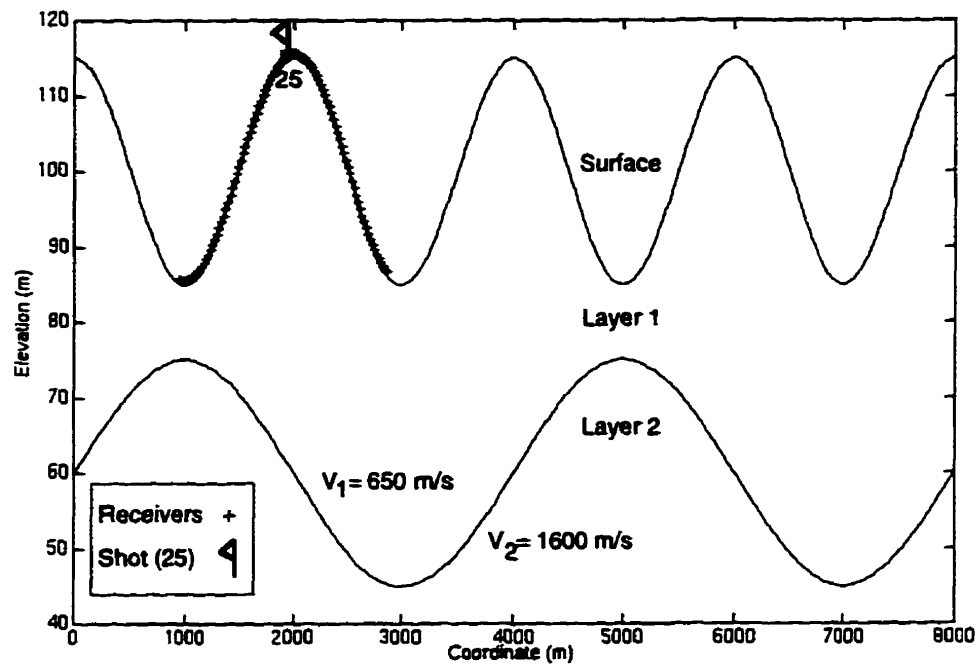


Figure 3.1. Synthetic initial model showing the location of one of the shot gather (25) (vertical exaggeration = 67).

#### 3.1.2 Refracted arrivals

From the initial model, split-spread direct and refracted arrivals traveltimes have been calculated from 101 shots and 96 roll-along receivers according to the Delay time analysis (Figure 3.2 and Equations 3.1 and 3.2).

$$T_r = h_s \cdot \cos(\theta_c) / V_1 + h_r \cdot \cos(\theta_c) / V_1 + X / V_2 \quad (3.1)$$

where  $T_r$  is the refracted arrival traveltime,  $h_s$  is the thickness of the first layer below the shot,  $h_r$  is the thickness of the first layer below the receiver,  $\theta_c$  is the refracted critical angle ( $\theta_c = \sin^{-1}(V_1/V_2)$ ), and  $X$  is the horizontal distance between the shot and the receiver.

$$T_d = X / V_1 \quad (3.2)$$

where  $T_d$  is the direct arrival traveltime.

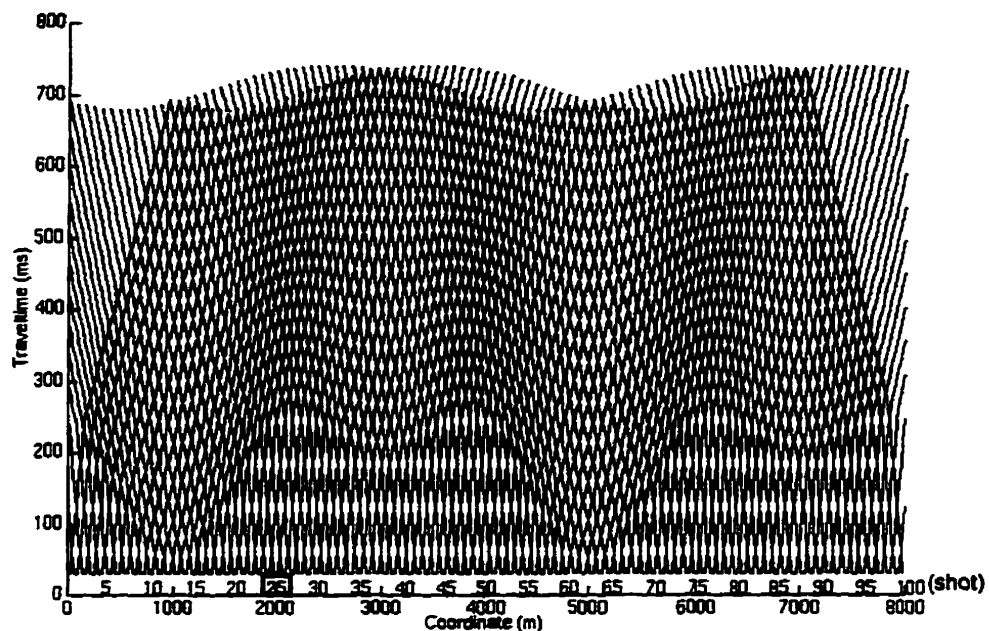


Figure 3.2. Direct and refracted arrival traveltimes resulting from the synthetic model.

## 3.2 PLUS-MINUS TIME ANALYSIS

### 3.2.1 Reciprocal time differences

The reciprocal time check provides a bank of all the possible shot pair reciprocal traveltime differences. Figure 3.3 shows the reciprocal traveltime differences of shot gather 25 with all the possible overlapping shot gathers. It can be noticed that reciprocal traveltime differences are equal to zero, so that the traveltime reciprocity is valid. This result was expected because synthetic calculated traveltimes are used.

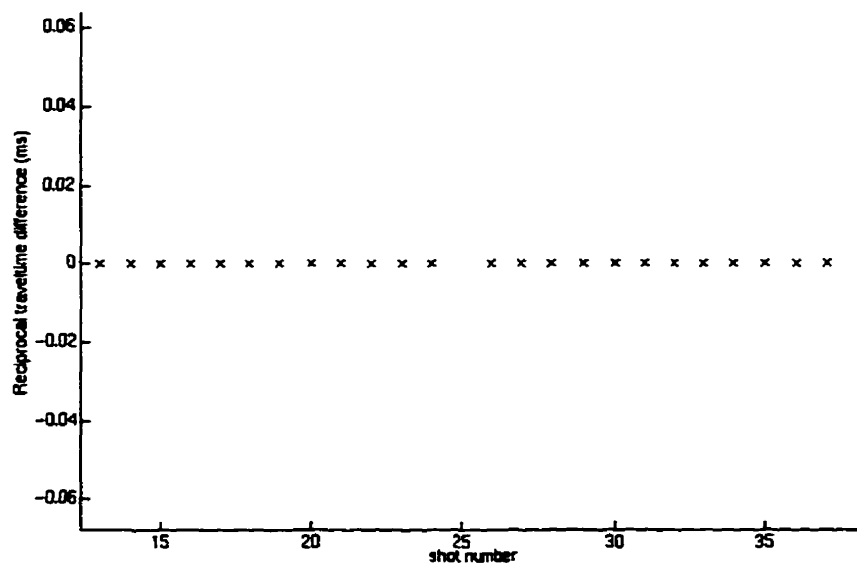


Figure 3.3. Reciprocal traveltime differences of overlapping shot spreads with shot 25.

### 3.2.2 Crossover points

The synthetic calculated traveltimes, being free of noise, represent an excellent example to demonstrate the crossover point autopicking. Figure 3.4 shows the autopicking process of the left crossover point for shot gather 20 and of the right crossover point for shot 25. The crossover point autopicking process was undertaken using a short median filter on the traveltime difference curve (window length of 5 samples).

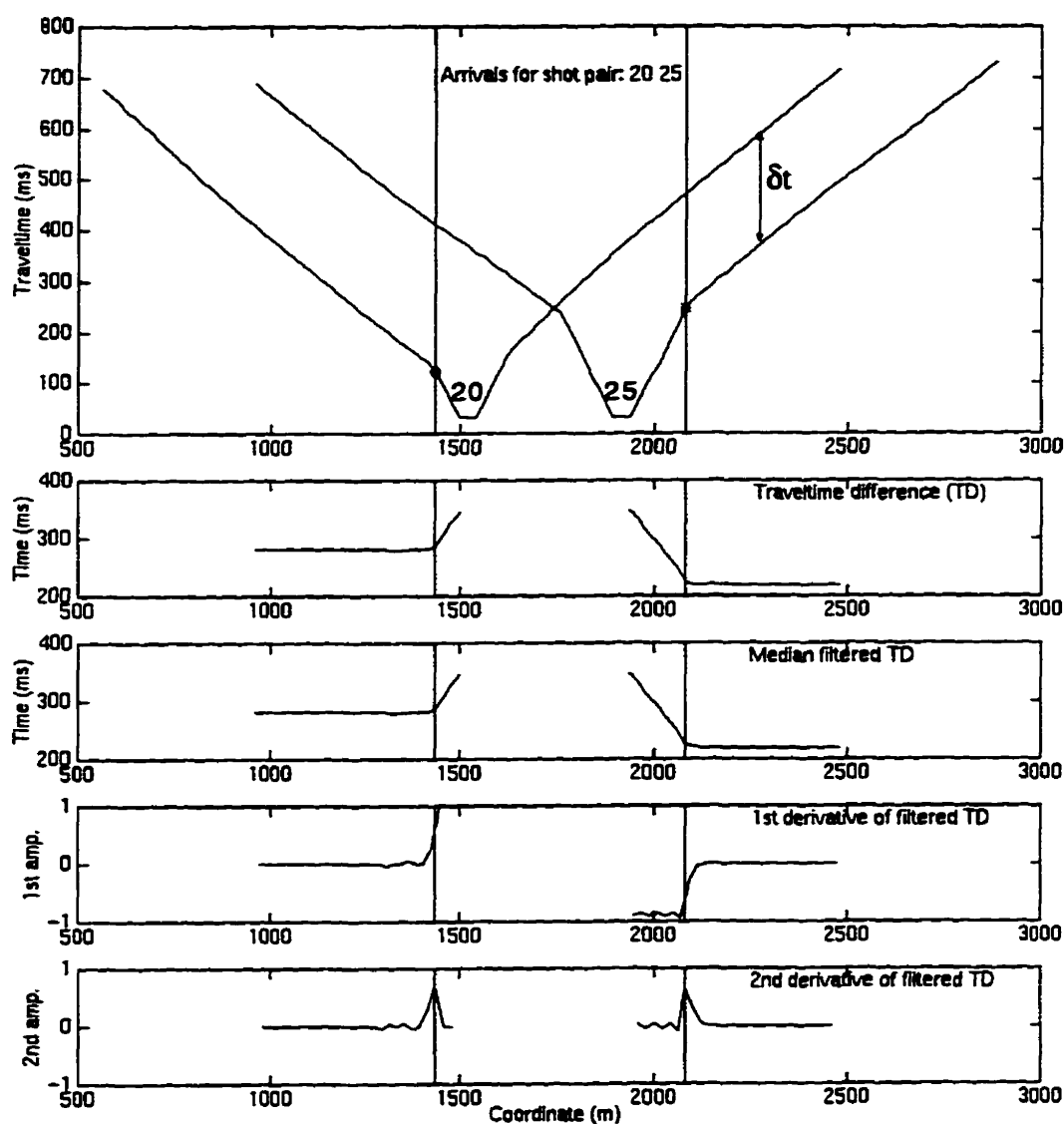


Figure 3.4. Crossover autopicking process for the left crossover point of shot gather 20 (o) and for the right crossover point of shot gather 25 (\*).

Once the crossover point autopicking process was completed for all the possible overlapping shot gathers, a crossover point rejection using a fraction (0.5) of the standard

deviation was applied. Then, the crossover point averages were computed. Figure 3.5 shows all the crossover point averages. From the crossover point averages, it can be noticed that the crossover point autopicking process was successful. The statistical results, including the crossover point average offset (from the corresponding shot location), the standard deviations and the fold are displayed in Figure 3.6. The crossover point average offsets are proportional to the first layer thickness (Figure 3.1). The standard deviation is equal to zero as a result of the crossover point rejection. Finally, the fold for the right crossover point averages decreases on the left extremity of the survey due to fewer overlapping shot gathers available, while the fold of the left crossover point average decreases on the right extremity of the survey for the same reason. The use of the crossover point statistical display is to help indicate inconsistencies in the crossover point average locations, and identify regions in the survey that need to be worked on by using the crossover point rejection process, the crossover point repicking process or the crossover point edit (see PMT method implementation in Appendix C).

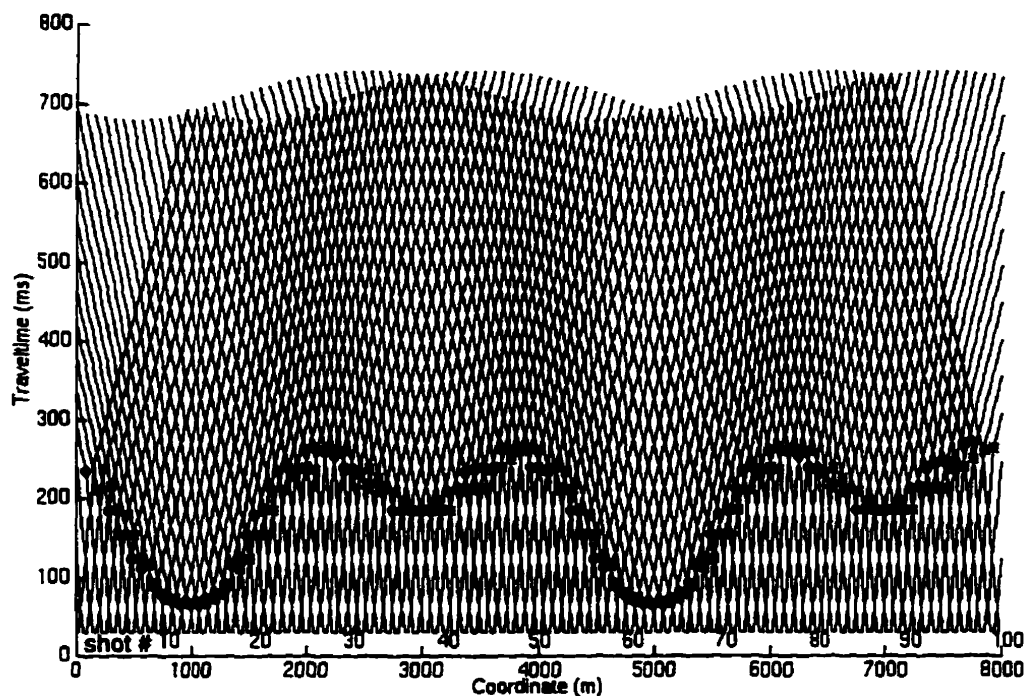


Figure 3.5. Crossover point averages of the synthetic dataset for the left trailing (o) and right leading (\*) shot spreads with all the arrival traveltimes.

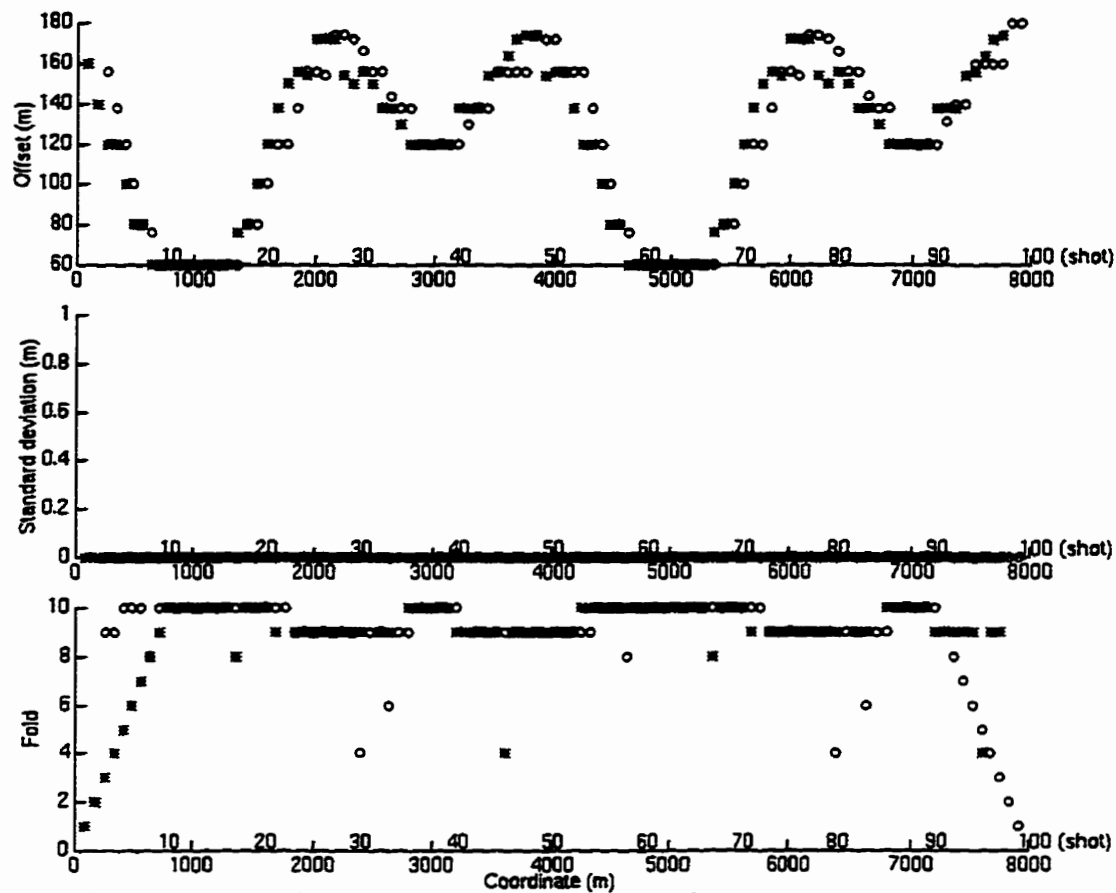


Figure 3.6. Crossover point statistics for the synthetic dataset.

### 3.2.3 Velocity model

The velocities of the first and second layers can be computed after the crossover point averages are known. The velocity calculation process uses the direct arrival traveltime to find the velocity of the first layer and the refracted arrival traveltimes to establish the second layer velocity. Figure 3.7 shows the velocity model calculated from the synthetic arrival traveltimes for each surface station location. This display will allow the user to determine if manual editing or filtering is needed before the depth calculation process is undertaken (see PMT method implementation in Appendix C). In this case, the first and second layer velocities are in agreement with the initial synthetic model, which demonstrates that the velocity calculations are reliable.

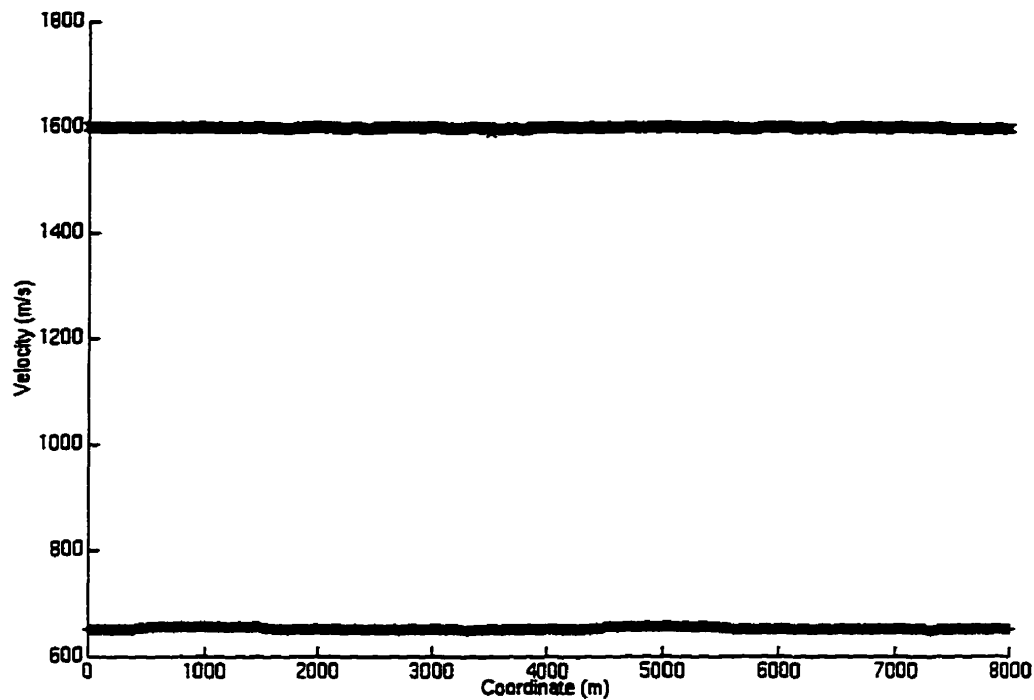


Figure 3.7. Velocity model calculated from the synthetic arrival traveltimes, including the first layer velocity (+) and second layer velocity (x). Both velocities were median filtered with a window length of 7 samples.

### 3.2.4 Plus time and Delay time

Once the crossover point averages are computed the Plus time analysis process can also be undertaken. Figure 3.8 displays the Plus time average values at each receiver with the corresponding statistics (standard deviation and fold). It plays the same role as the crossover point statistics display, which is to identify crossover point picking problems. The Plus time statistics will also help determine the parameters for the Plus time rejection process. The presence of bad traveltimes will introduce bad Plus time values. Hopefully, the ratio of bad to good Plus time values for a receiver location is low, so that the Plus time rejection process will exclude the bad Plus time values and keep the good ones. In this case, there are no bad arrival traveltimes so that the Plus time rejection process is not needed.

It can also be noticed that there is a Plus time value at each receiver location at the two line extremities. These Plus time values come from the use of the Delay time analysis for the surface locations outside the Plus-Minus time analysis window limit. The fold at these surface locations is less than at the other surface locations because Delay time analysis uses only one shot spread at a time, whereas Plus time analysis uses a combination of two or more shot spreads.

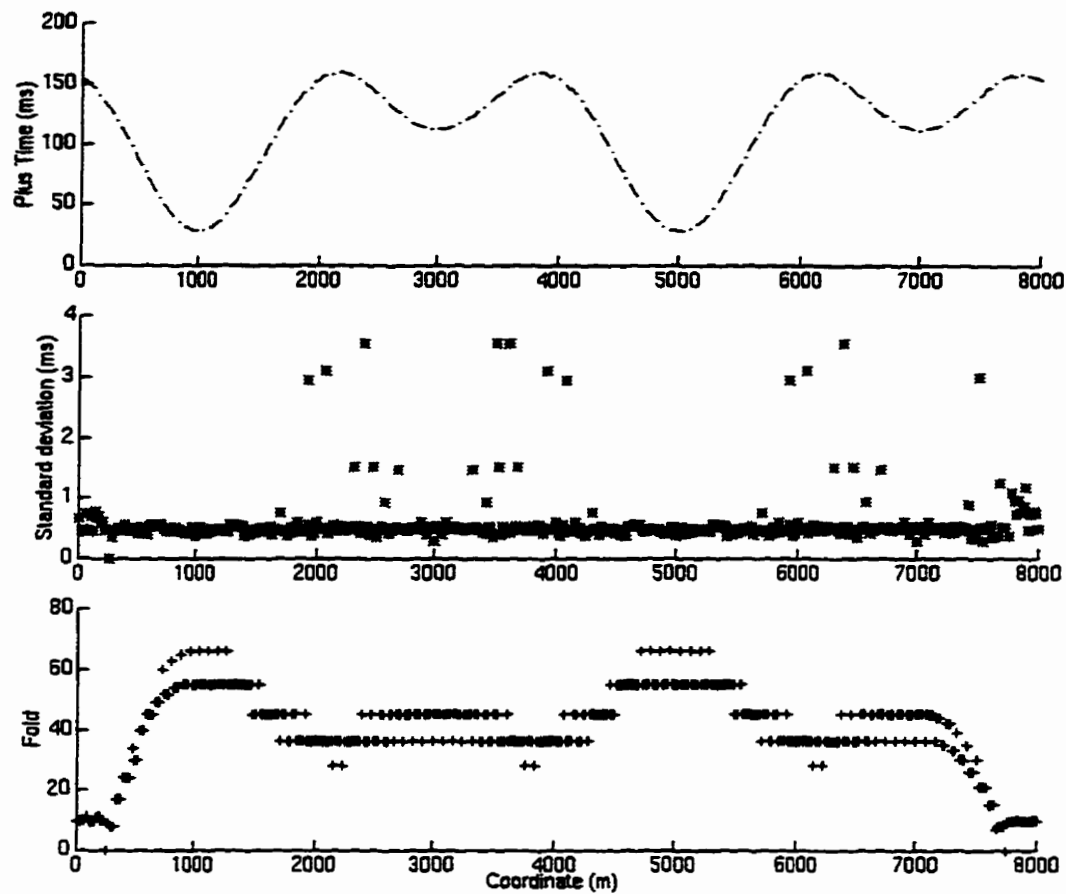


Figure 3.8. Plus time values and statistics for the synthetic dataset.

### 3.2.5 Depth model

Knowing the velocities and the Plus time values, the calculation of the first layer thicknesses were undertaken. Figure 3.9 shows the results of that calculation by displaying the surface elevation with the first and second layer interface (the first and second layer interface elevation is found by subtracting the calculated first layer thickness from the surface elevation). The calculated depth model closely matches the initial depth model (Figure 3.1). Figure 3.10 displays the model first layer thickness with the calculated one. The difference between the two thicknesses is very small (Figure 3.11). The root mean square error of the calculated first layer thickness is of 0.19 m and the maximum thickness error is 0.57 m.

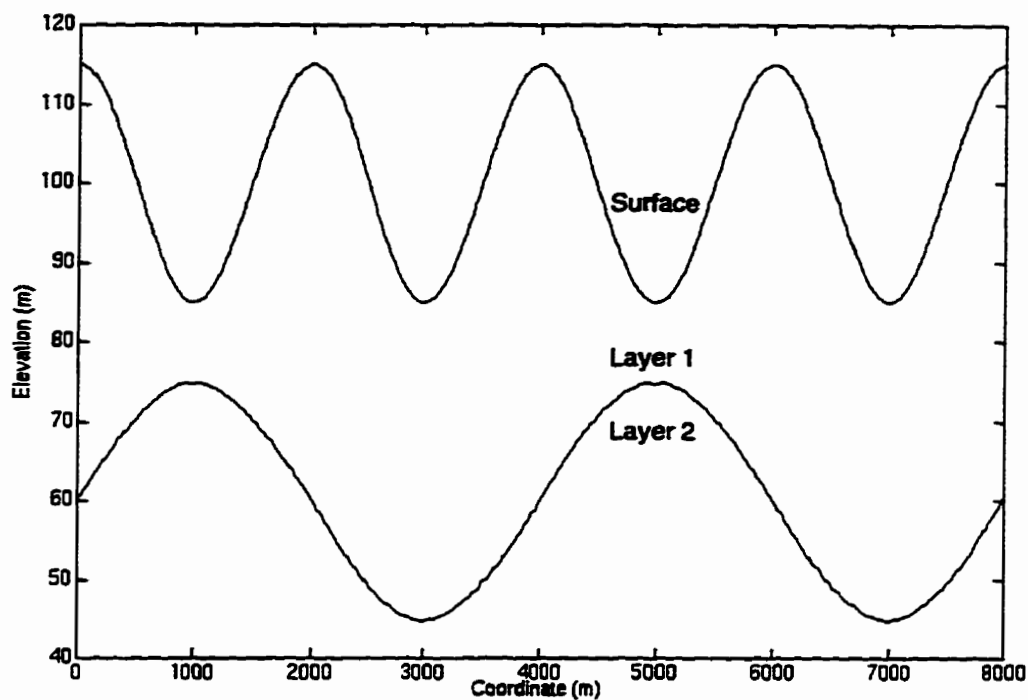


Figure 3.9. Calculated depth model from the synthetic arrival traveltimes (vertical exaggeration = 67).

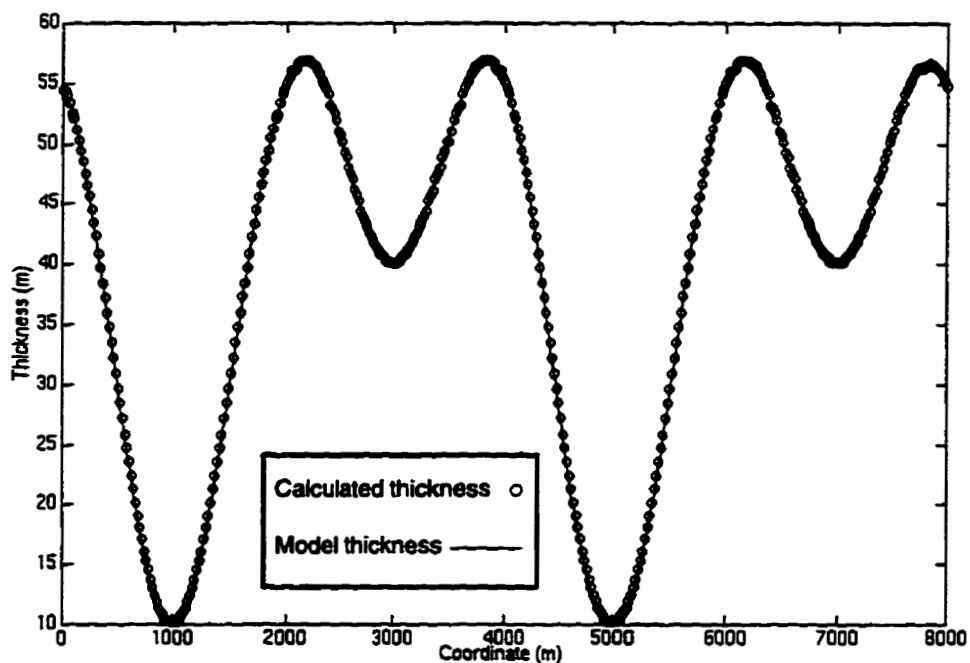


Figure 3.10. First layer thickness comparison between the initial model and the calculated model (vertical exaggeration = 107).

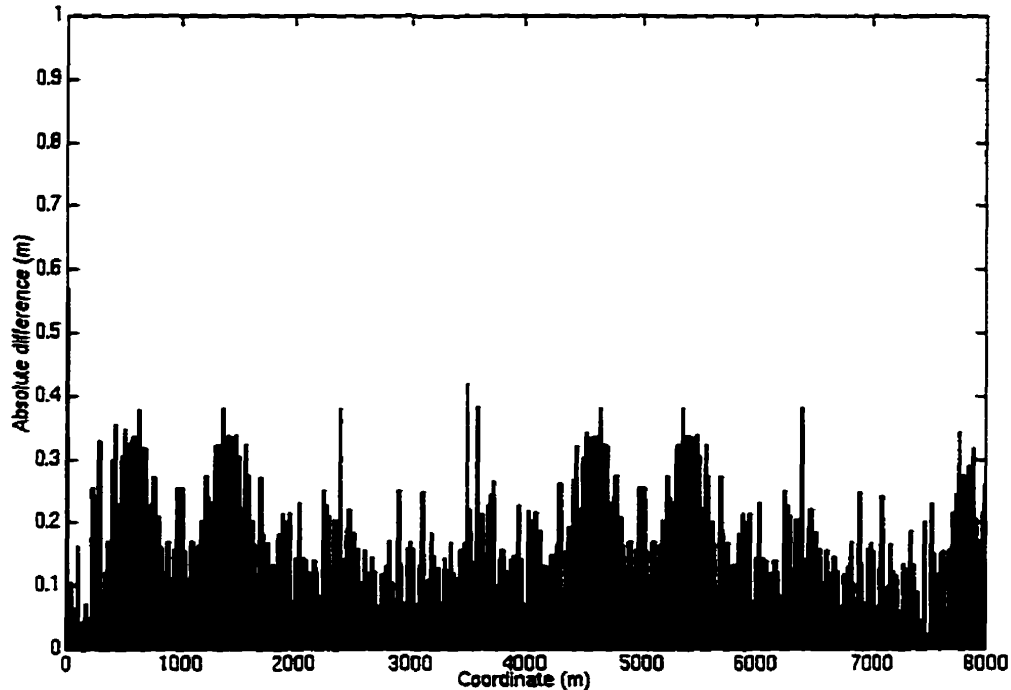


Figure 3.11. First layer thickness absolute difference between the initial model and the calculated model.

### 3.3 DISCUSSION

The Plus-Minus time analysis provides a reliable near-surface model when tested with a synthetic dataset. The method gives accurate depths and velocities. The strength of this method is an overdetermination of the solution and available statistical analysis. The crossover point determination uses a combination of the traveltime difference and the branch point analyses. This allows an automatic crossover point picking. The Plus-Minus time analysis can be fully automatic and no input near-surface model is needed. Therefore, the resulting near-surface model is strictly based on the refracted arrivals. The Plus-Minus time analysis method is simple and fast to use. The option of user interaction is omnipresent, allowing for a more consistent interpretation. This is facilitated by a user friendly menu interface.

## **CHAPTER 4 - REFRACTION ANALYSIS OF THE BLACKFOOT 2D-3C DATA**

### **4.1 INTRODUCTION**

In the Blackfoot Field area, 15 km east south east of Strathmore (Alberta), a three-component 2D seismic survey was acquired in 1995 by the CREWES project. 189 sources (6 kg dynamite) buried at 18 metres below the surface and 200 receivers at a 20 metres interval were used. The presence of an irregular thickness of poorly compacted near-surface deposits induces time delays for the recording of *P*-wave and *S*-wave reflection seismic data. The near-surface deposits in the region of Blackfoot are composed of a thin surficial layer of glacial deposits (less than 10 metres thick) and a low velocity sedimentary layer (Figure 4.1). The glacial deposits are mainly moraine (till) and lake (clay) deposits (Stalker, 1957). The area was glaciated by both Laurentide and Cordilleran ice during Pleistocene and till was deposited. The glaciolacustrine (lake) deposits were deposited beyond the glaciers, and during the nonglacial interval that followed the Pleistocene glacial interval (Teller and Clayton, 1983). In the northwest of the region, the first sedimentary layer, which corresponds to the bedrock in Figure 4.1, is a shale interbedded with fine-grained sandstone and coal (Paskapoo Formation, Tertiary), while in the east and south of the region, the sedimentary layer is an argillaceous sandstone (Edmonton Formation, Cretaceous) with some bentonitic shale (Irish, 1967). The seismic line crosses the two main types of glacial deposits (moraine and glaciolacustrine deposits) and lies over the Paskapoo Formation (Figure 4.1). Water wells in the proximity of the seismic line indicate that the low velocity shale of the Paskapoo Formation extends to at least 70 metres below the surface (see water wells in Appendix D).

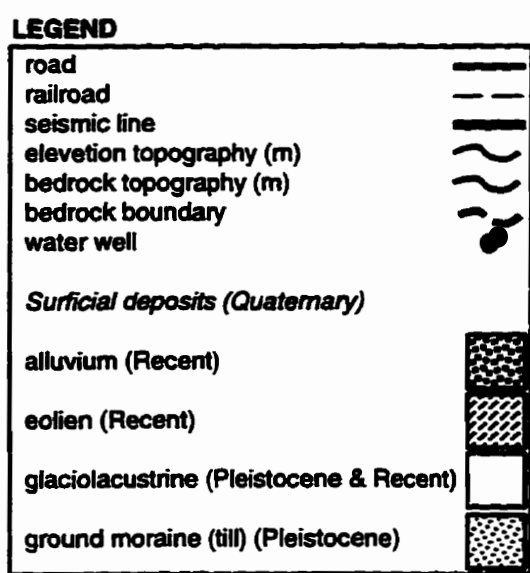
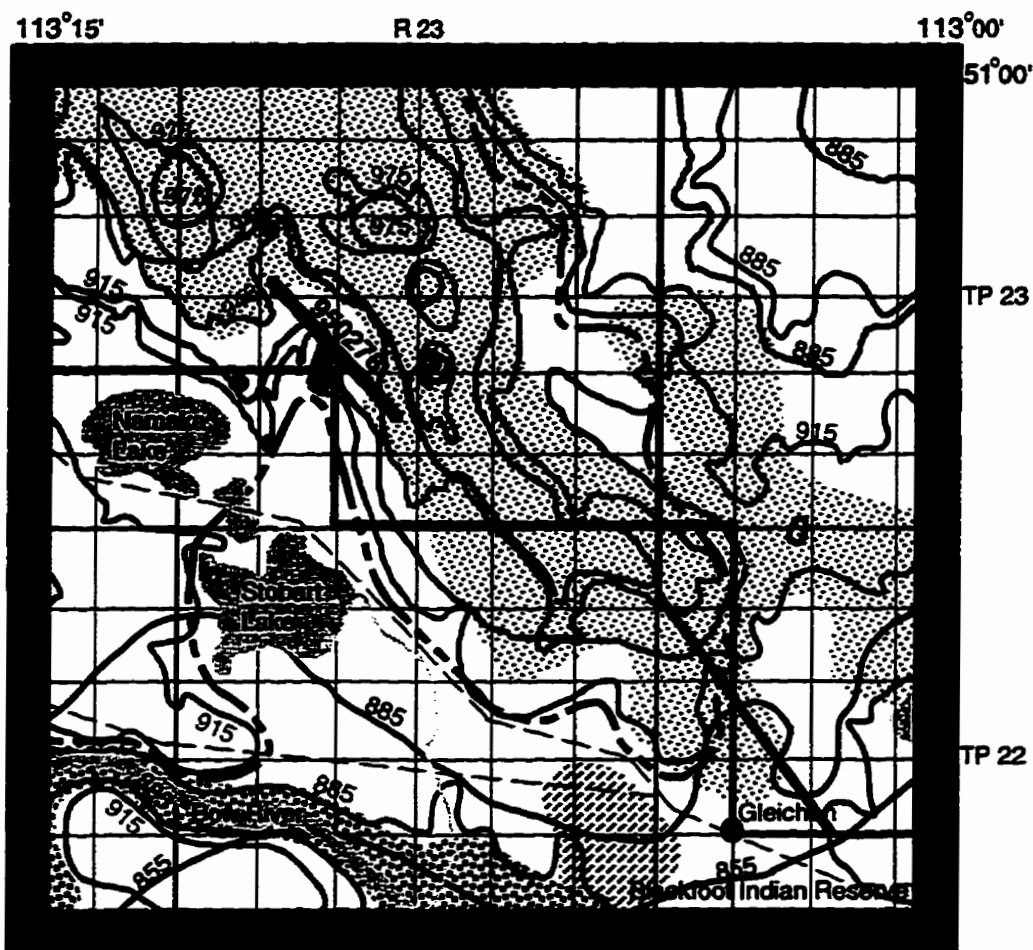


Figure 4.1. Near-surface geology map of the Blackfoot area modified from Stalker (1957), Geiger (1967) and Irish (1967).

Surface and near-surface effects can severely deteriorate the quality of reflection data, especially for *S*-wave data (Edelman and Helbig, 1983). The time delays affecting the *P-S* seismic data can be visualized by looking at the *P-S* reflection raypath geometry. Figure 4.2 illustrates how *S*-wave reflection is recorded after a conversion from a *P*-wave energy.

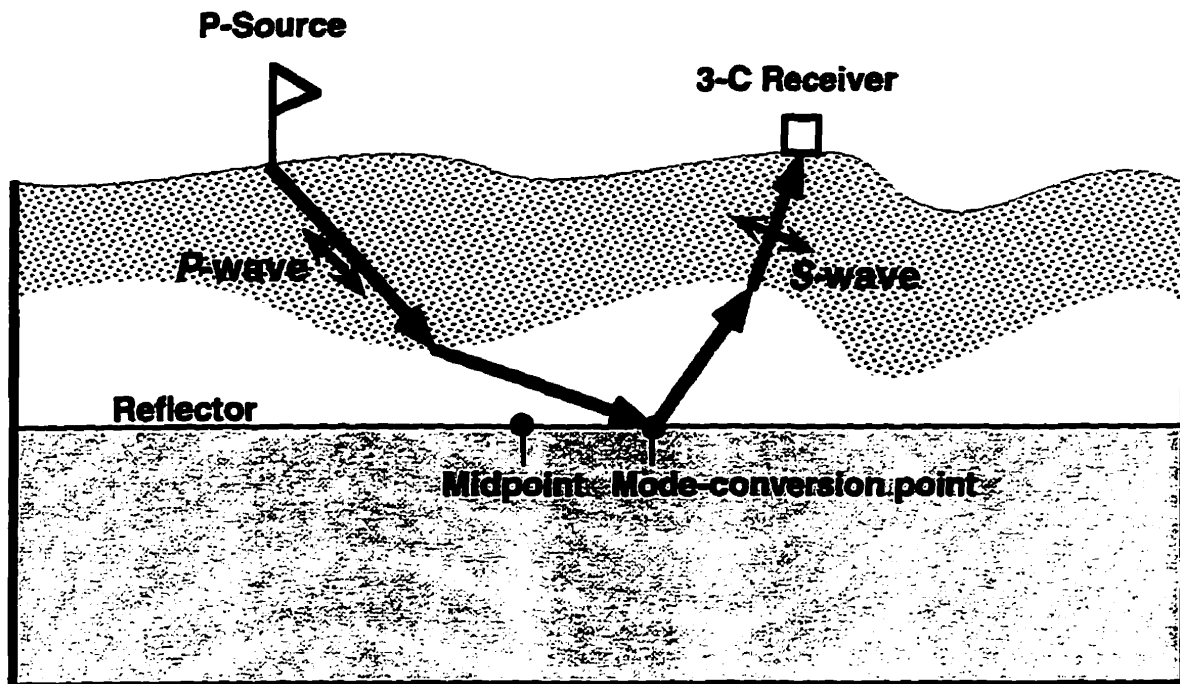


Figure 4.2. *P-S* reflection raypath geometry.

According to the *P-S* reflection raypath in Figure 4.2, the downgoing wave travels as a *P*-wave energy from the source through the surface deposits until the reflector, then some of the energy is converted to *S*-wave energy and travels back up to the surface to be recorded by a 3-component geophone. The *S*-wave energy should be recorded mainly on the horizontal components (radial and transverse). The radial component is in the same direction of the survey line, whereas the transverse component is perpendicular to the survey line. When no azimuthal anisotropy is present, the *S*-wave energy should be recorded mainly along the radial component (Cary and Eaton, 1993). The *S*-wave arrivals at the geophones are being delayed by the surface deposits, as a *P*-wave below the shot and as an *S*-wave below the receiver. To remove the shot delay, a near-surface *P*-wave model needs to be established, while to remove the receiver delay, a near-surface *S*-wave model needs to be built. The *S*-wave statics cannot be approximated by scaling the *P*-wave static values, because they are often unrelated (Anno 1986, Lawton 1990). As an example, the *P*-waves are affected by near-surface fluctuations in the water table while the *S*-waves are not. The Plus-Minus time analysis method developed in this thesis and the Generalized

Linear Inversion method of Hampson and Russell (1984) are used to establish the near-surface models. Their results are then compared according to the accuracy of the model, the static corrections and their impact on the reflection data.

*P*-wave refraction analysis is well known and is used to establish a near-surface *P*-wave model, from which static corrections are computed. However, *S*-wave refracted arrivals are not generally used to establish a near-surface *S*-wave model and to compute static corrections that are associated with severe time delays affecting the *P*-*S* seismic data. This is primarily because *S*-wave refracted arrivals are often masked by *P*-wave data superimposed (leaking) onto the radial component. Instead of using the refracted arrivals, the static corrections are usually determined by a hand picking process using common receiver stacks, which can bias the picks (Cary and Eaton, 1993). Also, real reflector structure can be flattened. The *S*-wave static corrections cannot be found by simply scaling the *P*-wave static corrections according to a  $V_P/V_S$ , because *P*-wave and *S*-wave velocity in the near-surface are not constant (Lawton 1990, and Wattrus 1989). Furthermore, residual static methods alone fail to remove long and intermediate wavelength and suffer from cycle-skipping.

## 4.2 SHEAR-REFRACTION ANALYSIS

### 4.2.1 Identification of *S*-wave refracted arrivals

Figure 4.3 illustrates the raypath geometry of *P* and *S*-wave refractions as well as the Rayleigh wave propagation mode. The propagation mode of a *P*-wave is in the same direction of its raypath trajectory, so that the *P*-wave energy is mainly recorded by the vertical component data, whereas the *S*-wave energy propagates perpendicularly to its raypath trajectory and is recorded by the radial component data. The conversion from a *P*-wave to an *S*-wave is believed to occur in close proximity to the source, so that the shear head-wave arrivals can be considered as pure *S*-wave refractions.

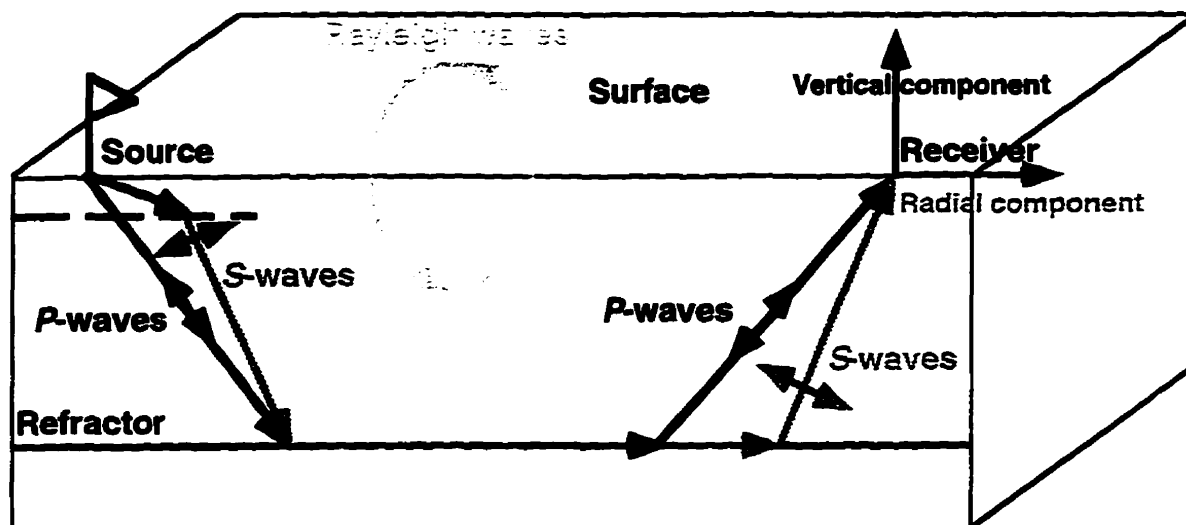


Figure 4.3. Raypath geometry of the Rayleigh-wave, the *S*-wave and *P*-wave refractions.

To help understand and determine the polarization of different events, three domains, including shear head-wave arrivals were picked on the vertical and radial components (Figures 4.4 and 4.5, respectively). Figure 4.6 shows the relative amplitude of the shear head-wave arrivals (*S*-wave refractions) on the radial and vertical component data. Amplitude points cluster in the radial component direction, which shows that the event is horizontally polarized. *P*-wave refraction events also have a rectilinear polarization, but in the vertical component direction (Figure 4.7), whereas Rayleigh wave events have an elliptical polarization (Figure 4.8).

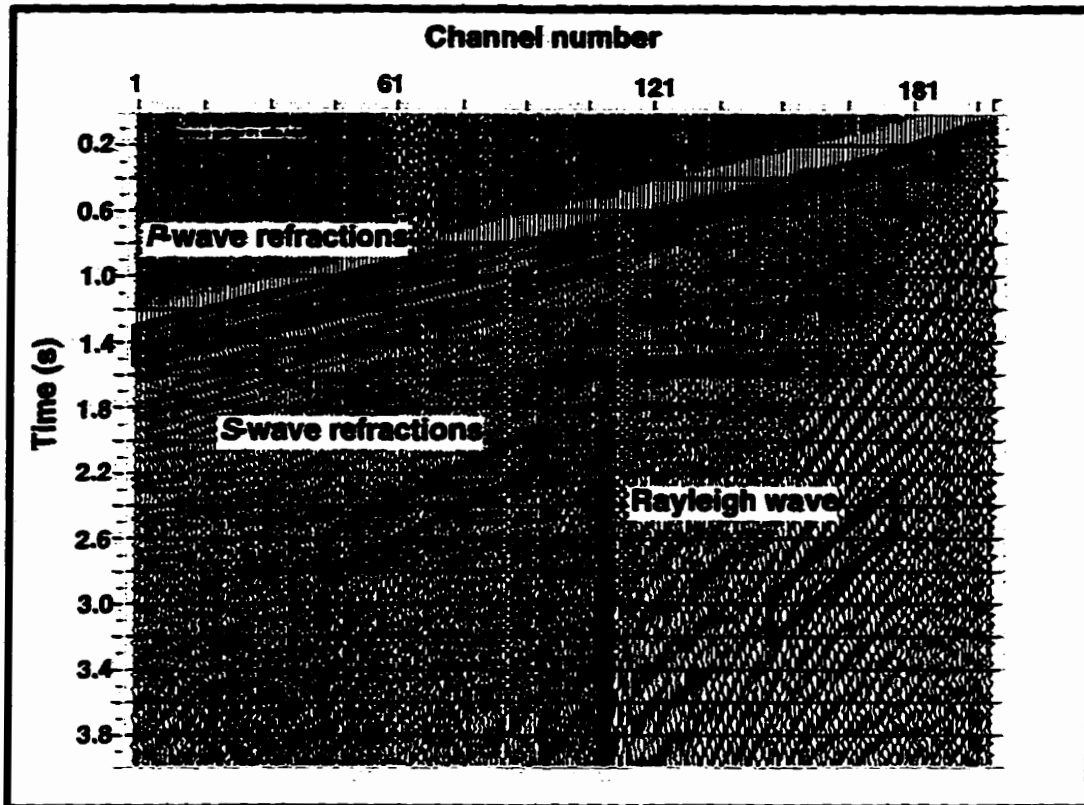


Figure 4.4. Vertical component data (shot gather #1).

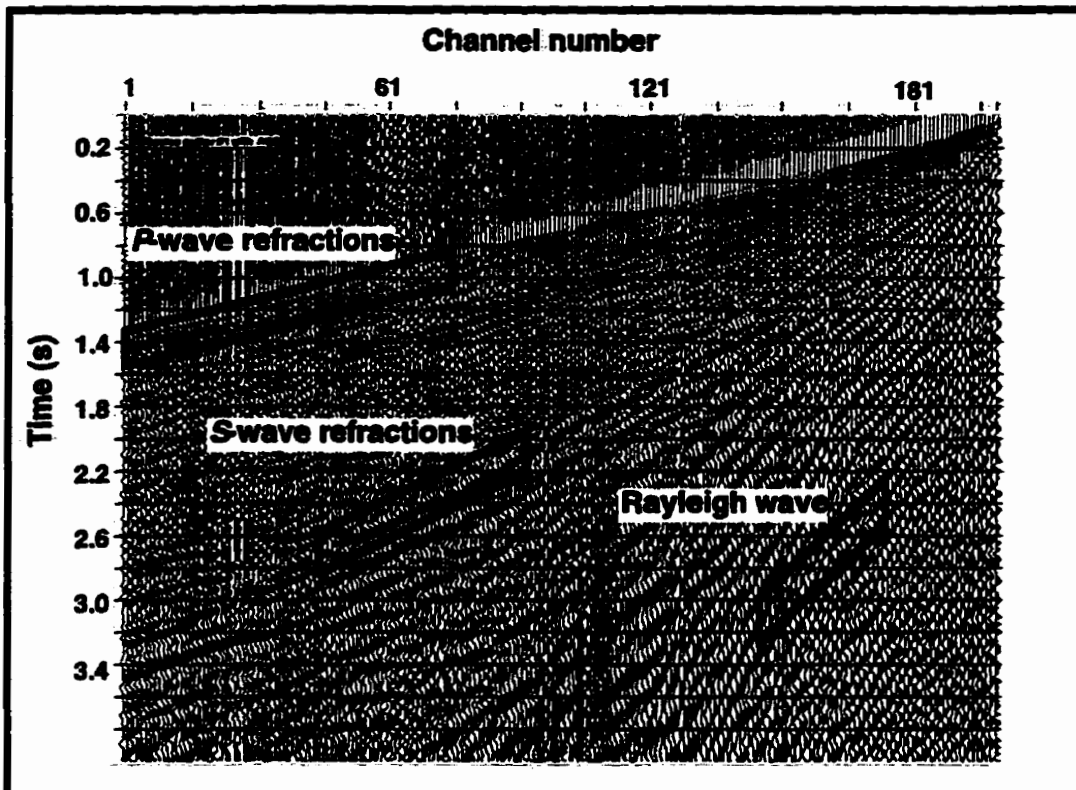


Figure 4.5. Radial component data (shot gather #1).

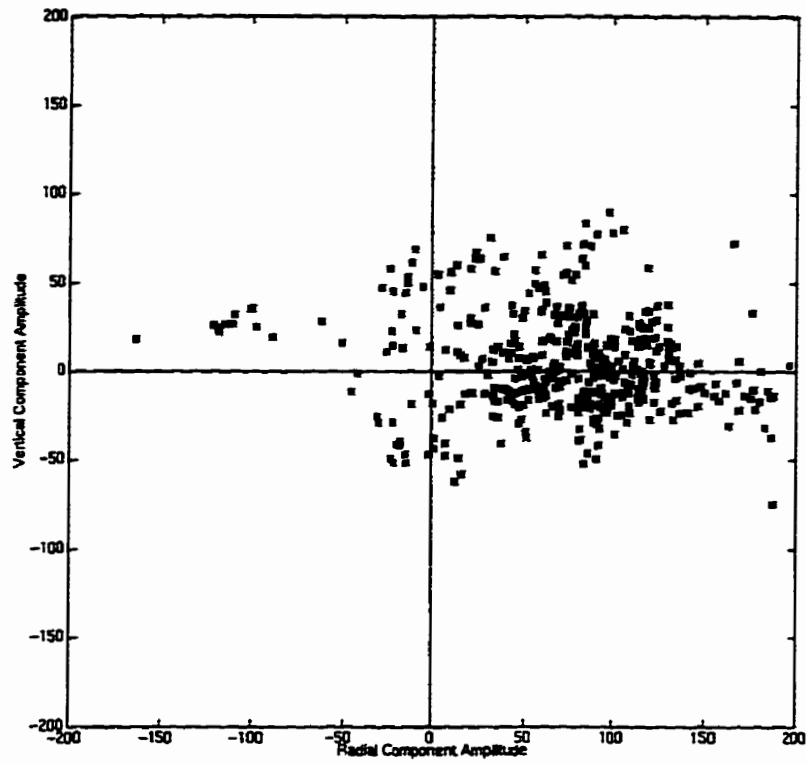


Figure 4.6. Relative vertical and radial component amplitude of the *S*-wave refractions.

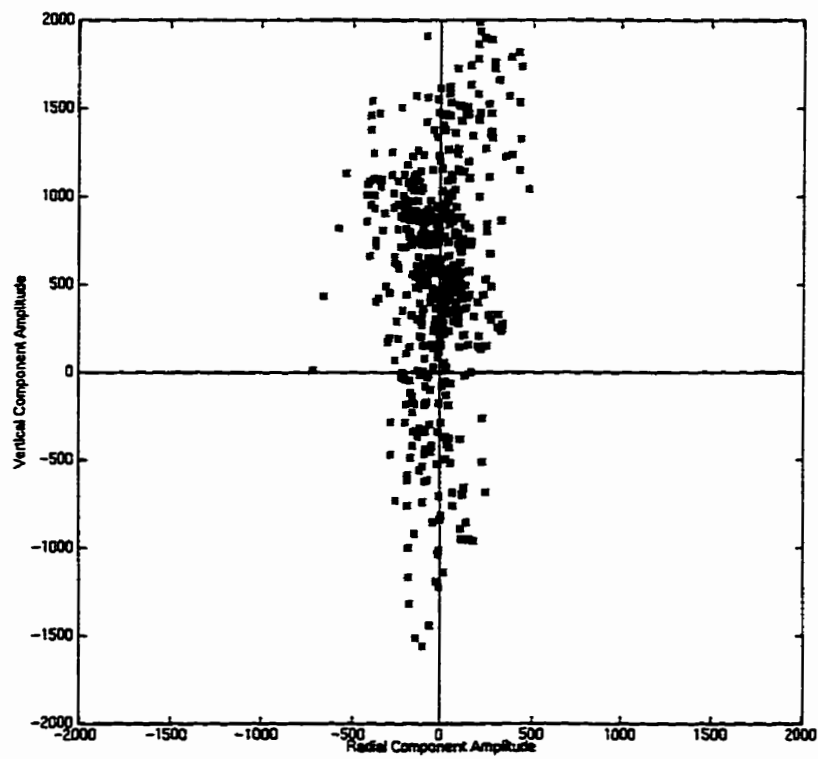


Figure 4.7. Relative vertical and radial component amplitude of the *P*-wave refractions.

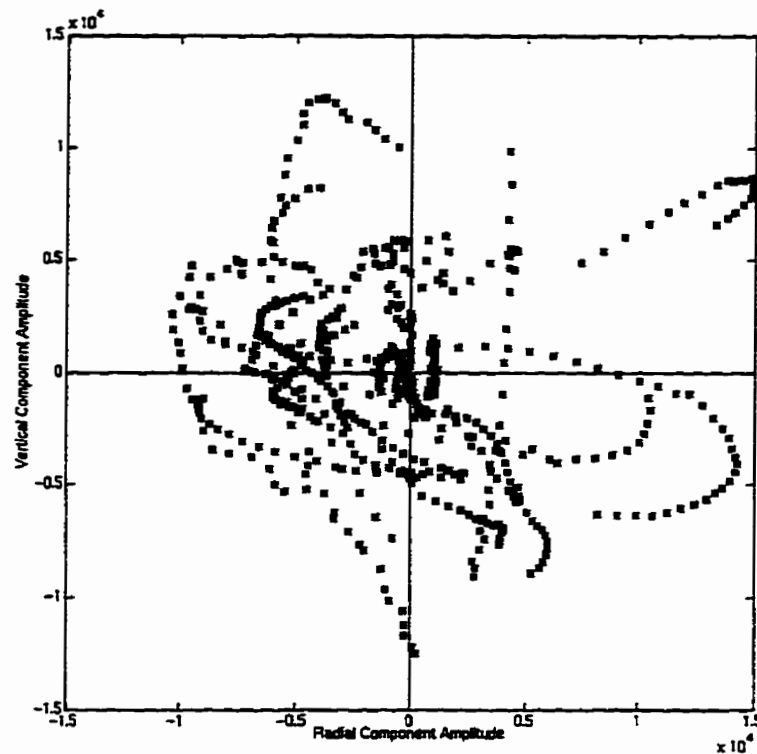


Figure 4.8. Relative vertical and radial component amplitude of the Rayleigh-wave.

*S*-wave refraction events have been identified on the radial component data (in between dashed line in Figure 4.9). As demonstrated, these events are interpreted to be shear head-wave arrivals rather than Rayleigh wave events because their polarization is approximately rectilinear rather than elliptical (Jolly and Mifsud, 1971).

#### 4.2.2 Signal enhancement

A problem of using the *S*-wave refracted arrivals is that they are masked by *P*-wave data and *P-S* reflection data. In an effort to remove these signals and to keep only the *S*-wave refraction events, an *F-K* filter was applied to the radial component data. As a result of data filtering, the refracted arrivals were more easily and rapidly picked (Figure 4.10). From these refracted arrival picks, any standard refraction static method can be used to establish a near-surface model and compute the receiver static corrections.

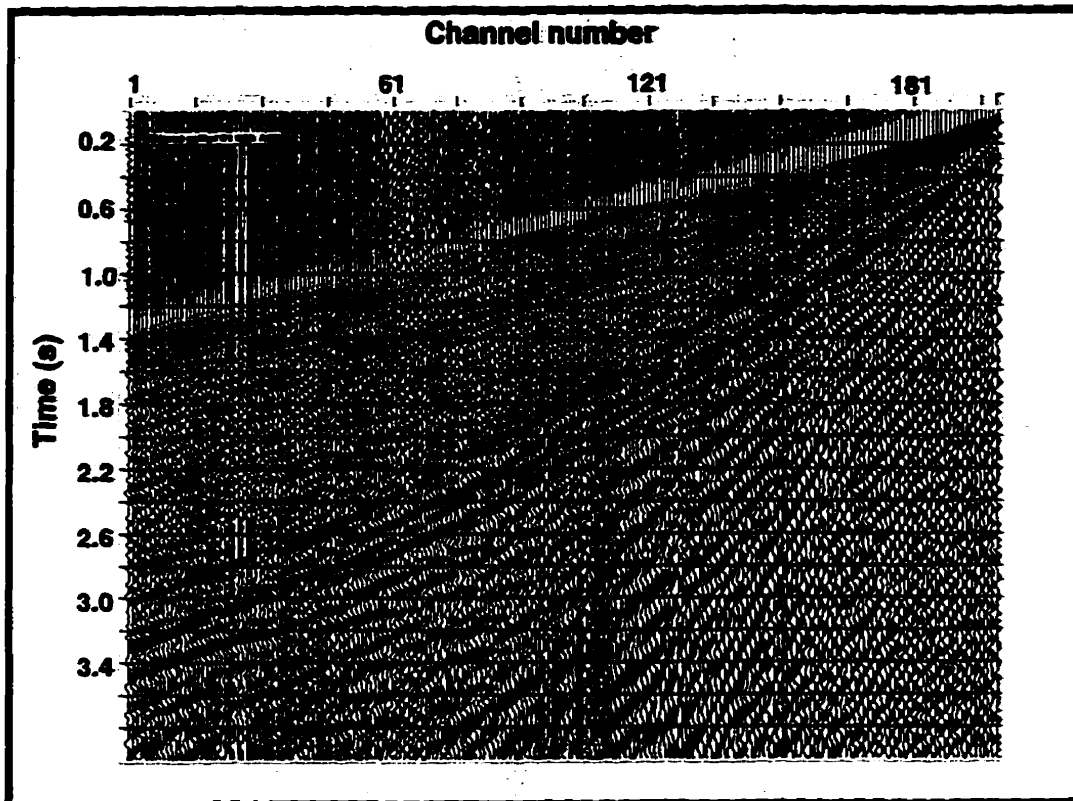


Figure 4.9. Radial component from the Blackfoot dataset (shot gather #1).

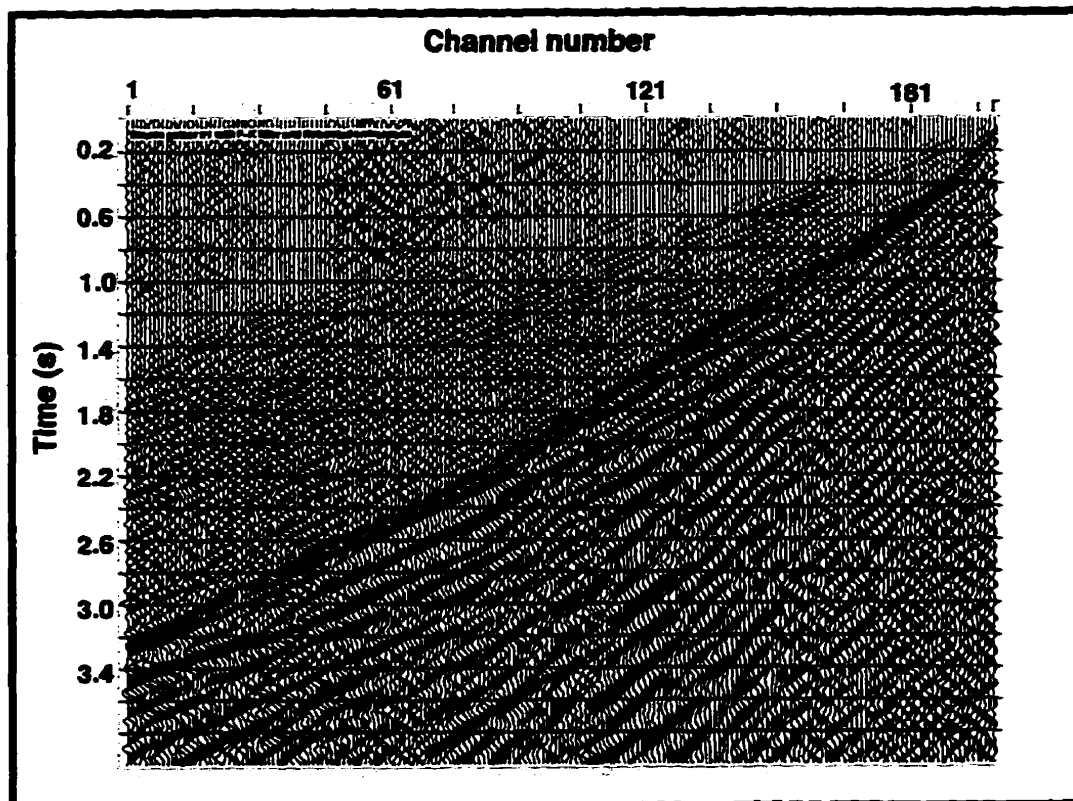


Figure 4.10. Radial component with an  $F-K$  filter applied and S-wave refractions picks (\*).

### 4.3 PLUS-MINUS TIME ANALYSIS

Two refraction static methods were used to find the  $P$  and  $S$  near-surface models. The first method used was the Plus-Minus time analysis method based on the “plus-minus” method of Hagedoorn (1959) and presented in Chapter 2. The “plus-minus” method is an approximation of the wavefront reconstruction method by Thornburgh (1930). The Plus time analysis establish the depth to the refractor below the receivers, while the Minus time analysis finds the velocity of the refractor. The Generalized Linear Inversion by Hampson and Russell (1984) has been used to provide a comparison with the Plus-Minus time analysis method (see section 4.4).

#### 4.3.1 Refracted arrivals

The  $P$ -wave refracted arrivals (first-breaks) were picked on the vertical component data (Figure 4.11), while the  $S$ -wave refracted arrivals were picked on the radial component data (Figure 4.12). It can be noticed that the  $S$ -wave refracted arrival traveltimes are about twice the  $P$ -wave refracted arrival traveltimes. This is a consequence of slower velocity of the  $S$ -wave compared to the  $P$ -wave. Some of the  $S$ -wave refracted arrival traveltimes are absent due to difficulty in picking the event from the records.

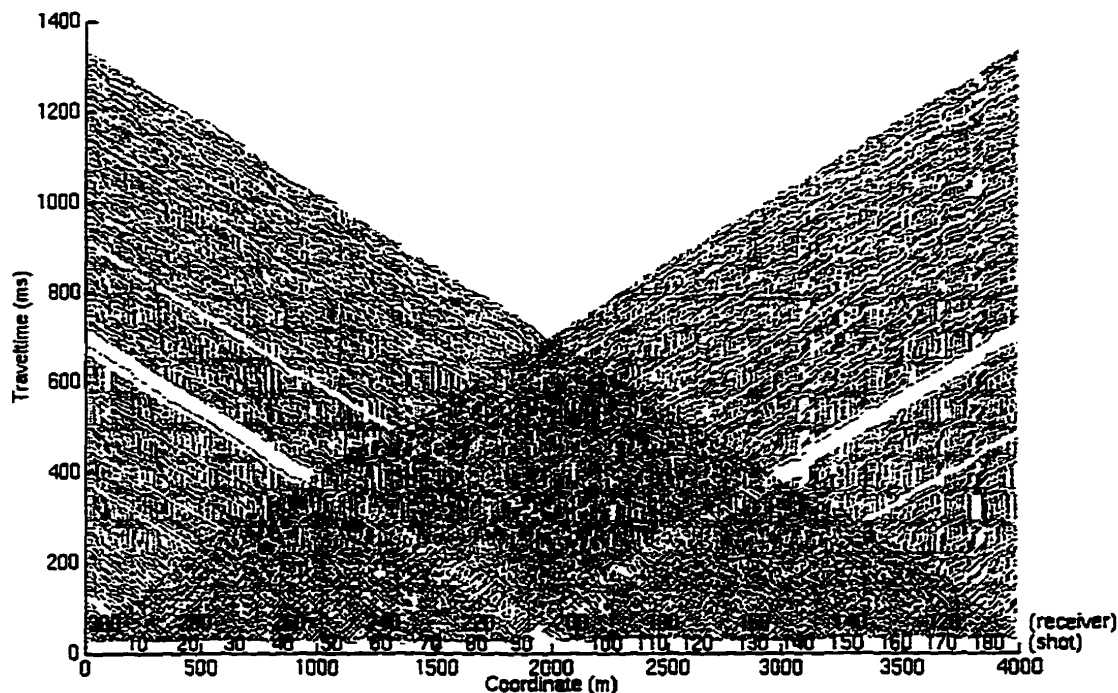


Figure 4.11.  $P$ -wave refracted arrival traveltimes from the vertical component data.

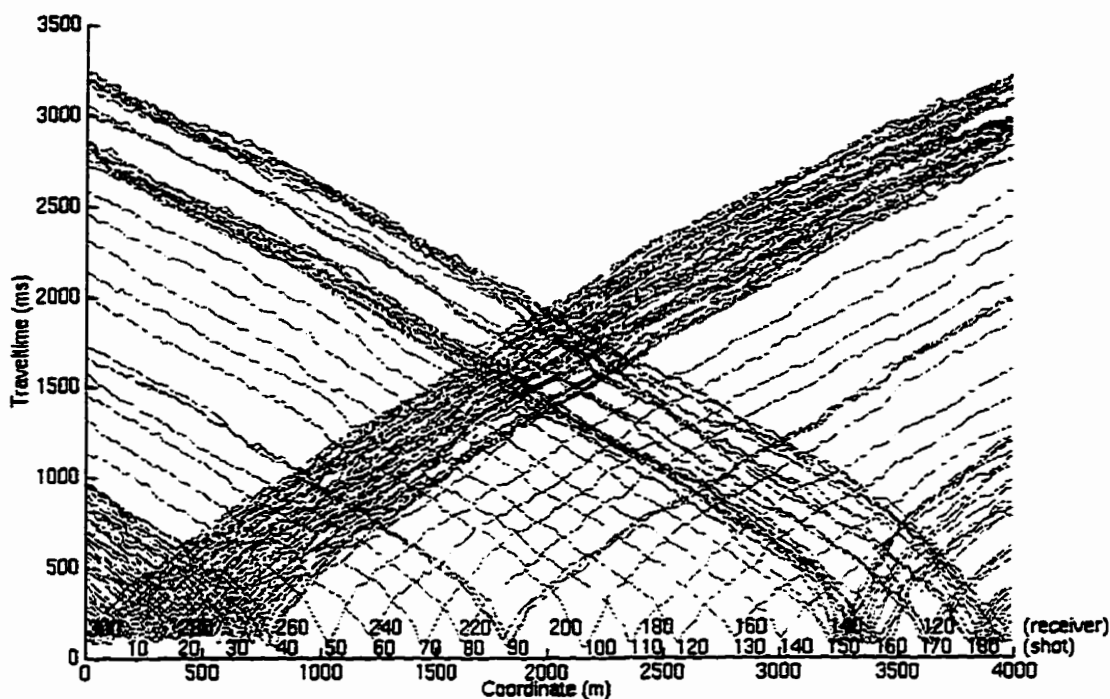


Figure 4.12. *S*-wave refracted arrival traveltimes from the radial component data.

#### 4.3.2 Reciprocal time differences

The average reciprocal traveltime difference for the *P*-wave refractions is 4 ms and 47 ms for the *S*-wave refractions. This difference between the *P*-wave and *S*-wave refraction traveltime reciprocity is due to the fact that the *S*-wave refracted arrival traveltimes are at least twice the *P*-wave refracted arrival traveltimes, and to a larger picking error. A depth variation of the conversion from the source *P*-wave to *S*-wave along the survey line would also create more important reciprocal traveltime difference for the *S*-wave refracted arrivals. Therefore, reciprocal traveltime differences added to the traveltimes of one of the shots, thus correcting for slight separations between shots and receivers at the same station, depth conversion variations (*S*-wave refractions only), picking errors and inaccuracy in the uphole times.

### 4.3.3 Crossover points

The crossover point represents a change in the refracted arrivals from one layer to another, and crossover point locations determine the Plus-Minus time analysis window limits. The crossover point autopicking process was undertaken on both refracted arrivals (*P* and *S*) using a median filter window length of 11 samples on the traveltime difference and a differentiation separation length of 3 samples for the first derivative. Example of this analysis are shown in Figures 4.13 and 4.14. The crossover point locations correspond to the maximum of the second derivative (Wang and Cheadle, 1995).

Once the crossover point autopicking processes using all the possible overlapping shot gathers were completed for both refracted arrivals (*P* and *S*), the crossover point rejection according to one standard deviation was used. Then, the crossover point averages were computed and some of them were edited to a proper location according to a consistent interpretation. Figure 4.15 shows the location of the crossover point averages on their respective arrival shot spreads for the *P*-wave refractions, while Figure 4.16 displays the crossover point average offsets (from the corresponding shot location), the standard deviations and the fold. It can be noticed that the crossover point average offsets varies from 124 to 475 metres and that they generally increase at both ends of the survey, while the standard deviation goes from zero to 122 metres (average of 28 metres). The fold for the right crossover point averages decreases on the left extremity of the survey due to fewer overlapping shot spreads available, while the fold of the left crossover point average decreases on the right extremity of the survey. The maximum fold is 152 and the average is 70.

The equivalent displays are available for the *S*-wave refractions, so the location of the crossover point averages and their respective arrival shot spreads are shown in Figure 4.17, while the crossover point average offsets, the standard deviations and the fold are illustrated by figure 4.18. The crossover point average offsets range from 70 to 286 metres, while the standard deviation goes from zero to 190 metres (average of 18 metres). The maximum fold is 62 and the average is 27.

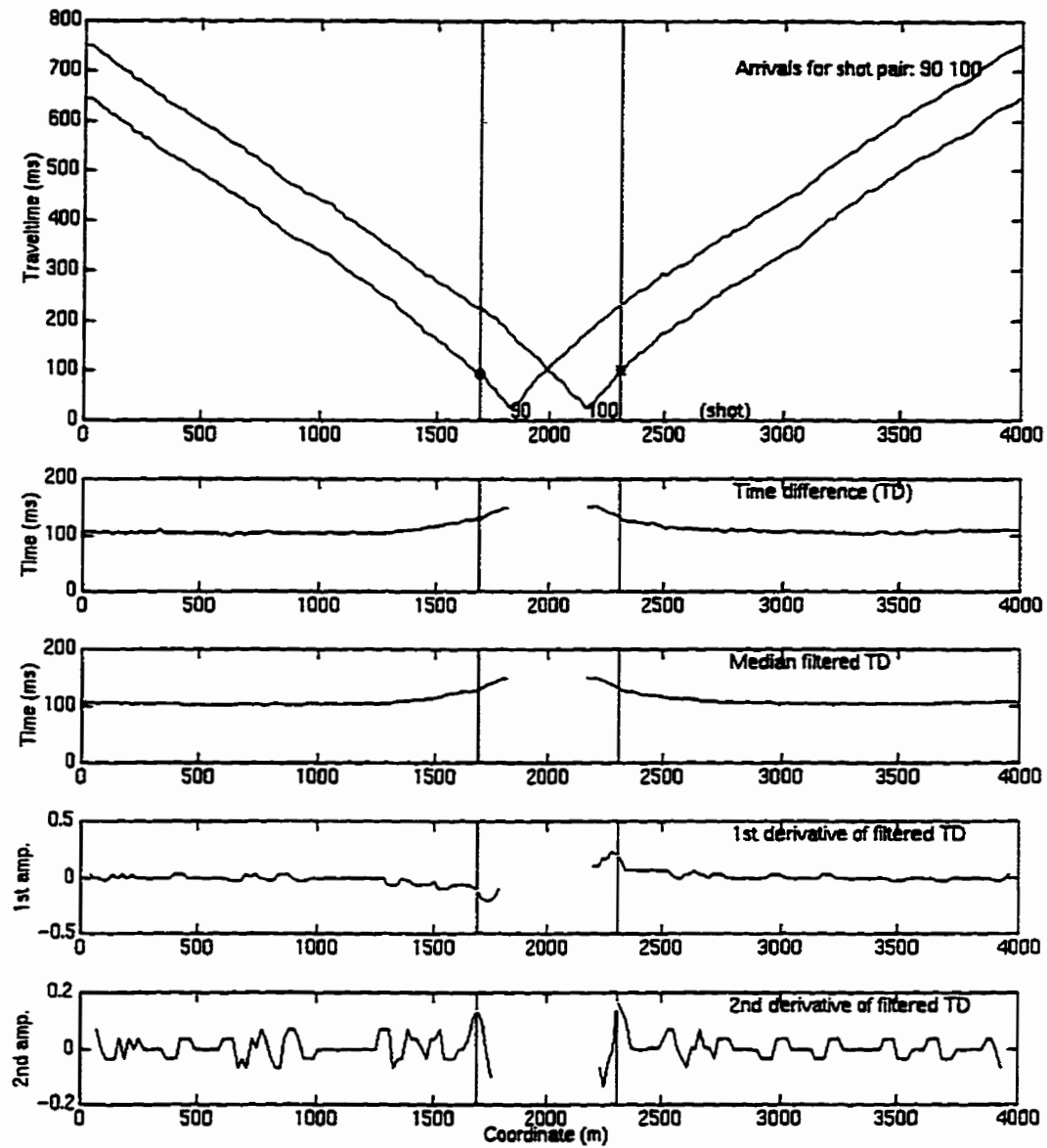


Figure 4.13. Crossover autopicking process for the left crossover point of shot gather #90 (o) and for the right crossover point of shot gather #100 (\*) on the *P*-wave refractions (median filter window length of 11 samples and differentiation separation length of 3 samples).

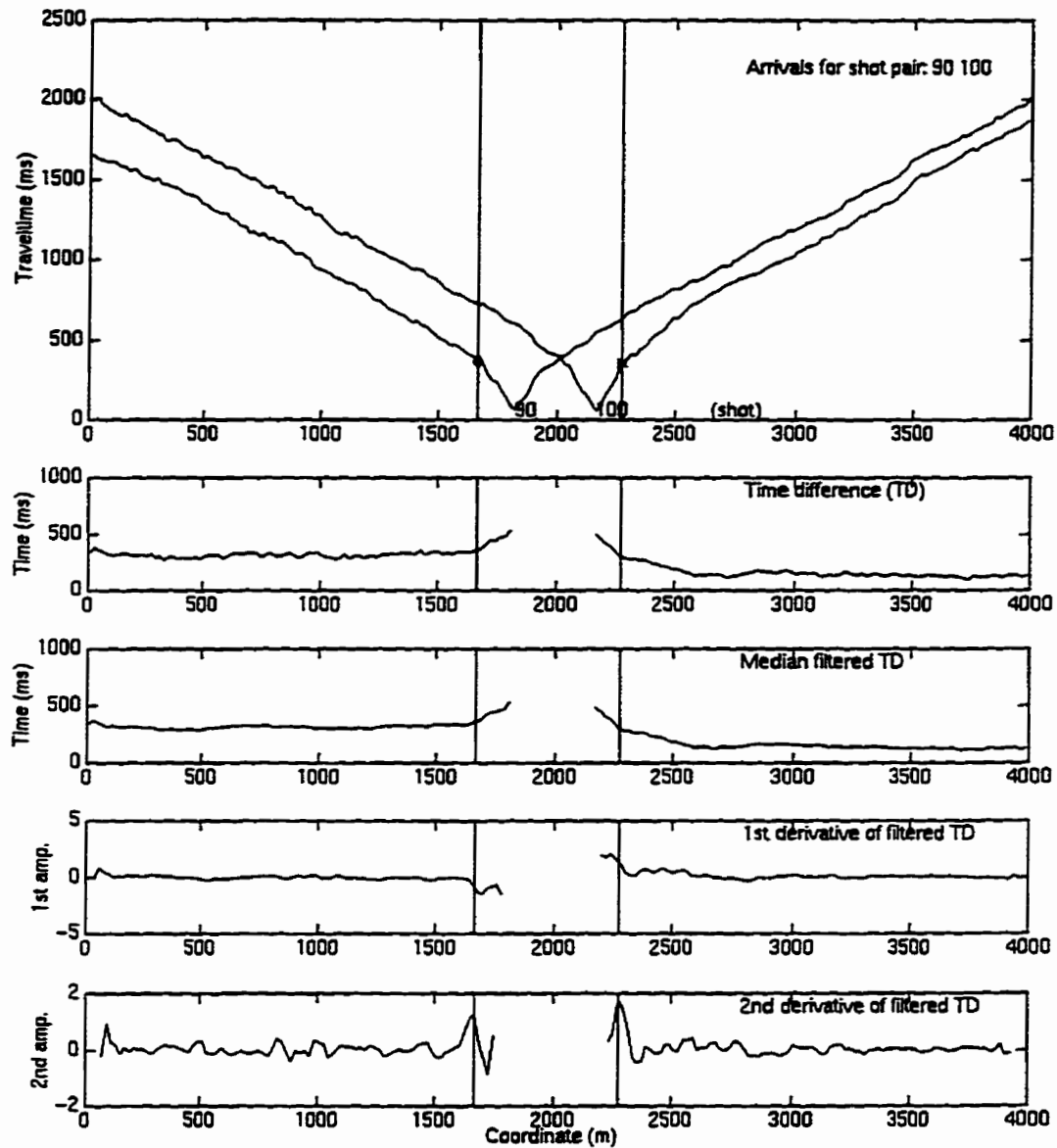


Figure 4.14. Crossover autopicking process for the left crossover point of shot gather #90 (o) and for the right crossover point of shot gather #100 (\*) on the S-wave refractions (median filter window length of 11 samples and differentiation separation length of 3 samples).

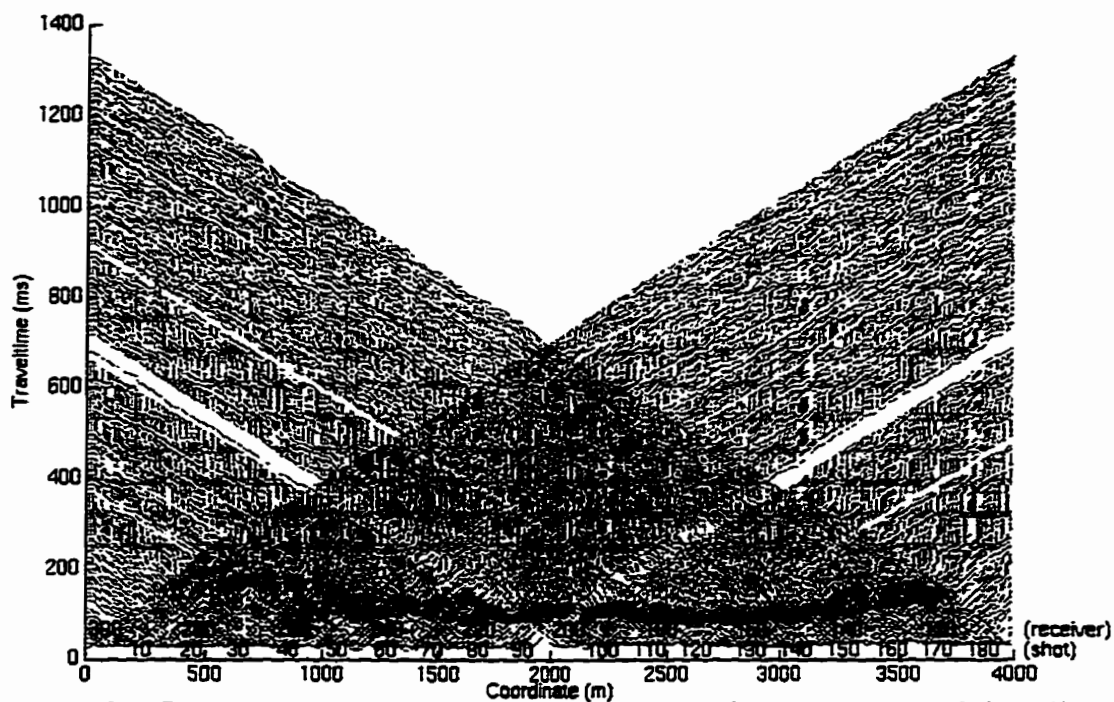


Figure 4.15. Crossover point averages of the  $P$ -wave refractions for the left trailing (o) and right leading (\*) shot spreads.

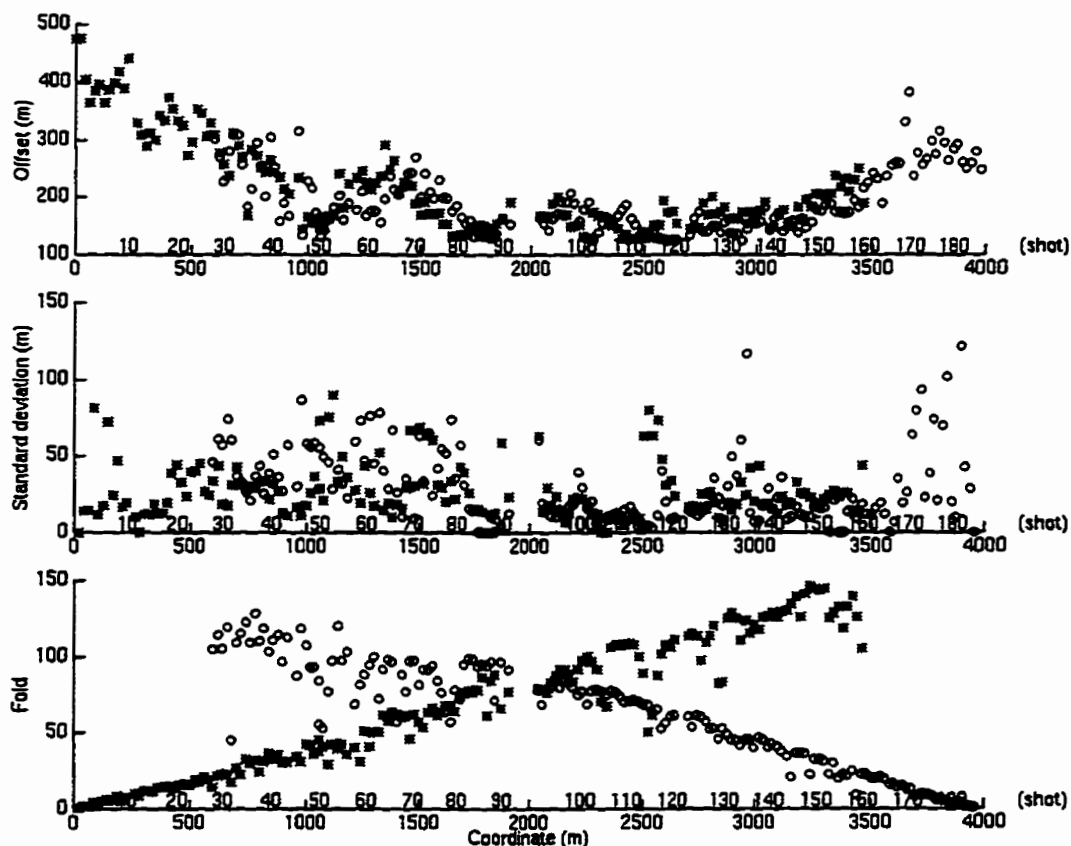


Figure 4.16. Display of the right crossover point average (\*) and left crossover point average (o) for the  $P$ -wave refractions.

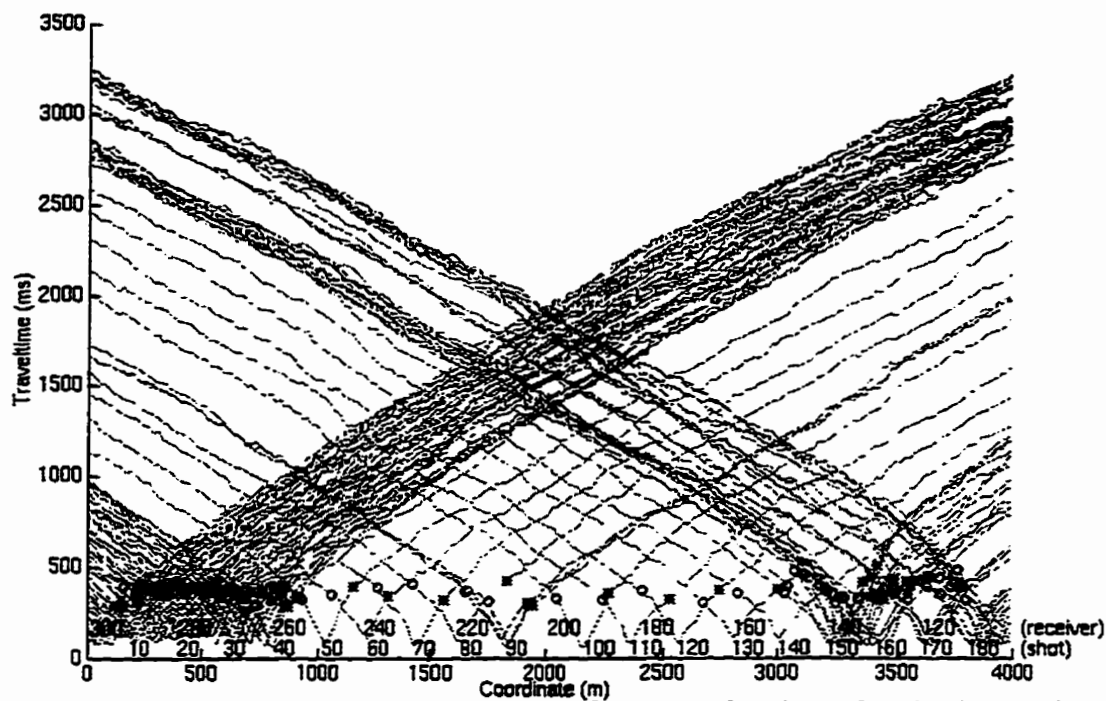


Figure 4.17. Crossover point averages of the  $S$ -wave refractions for the left trailing (o) and right leading (\*) shot spreads.

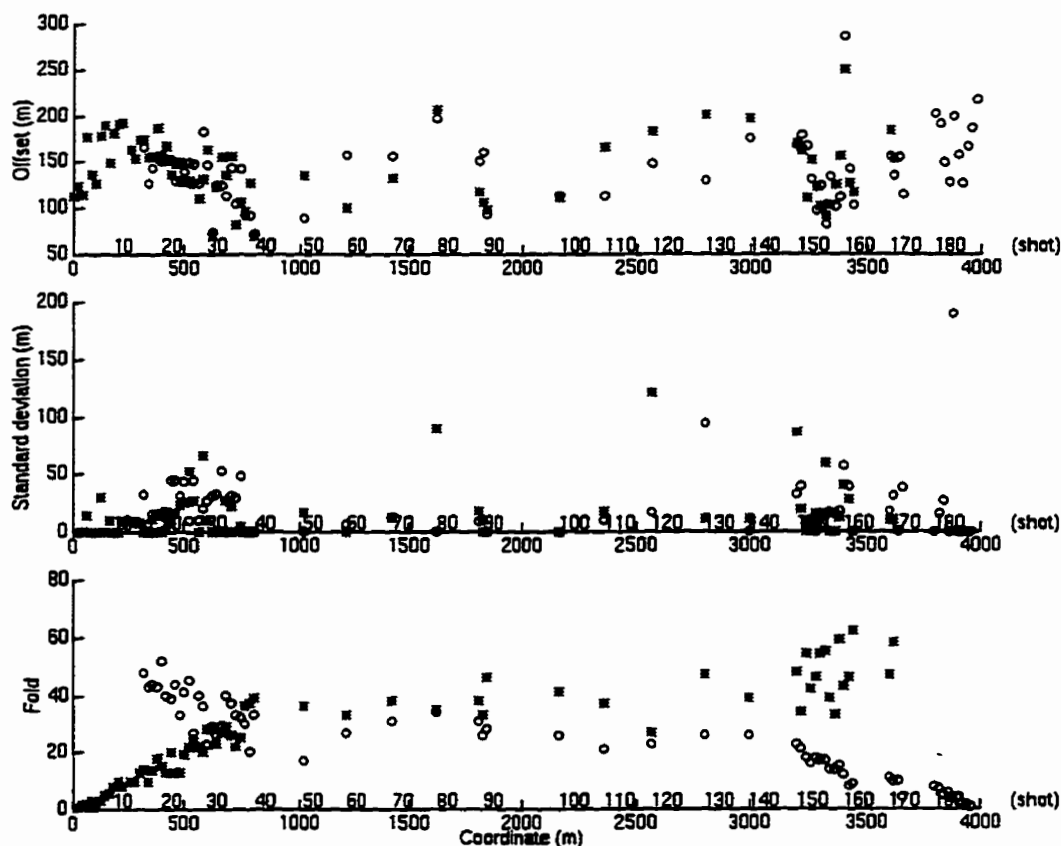


Figure 4.18. Display of the right crossover point average (\*) and left crossover point average (o) of the  $S$ -wave refractions.

#### 4.3.4 Velocity model

The velocity model was established from the knowledge of the crossover point average locations. The velocity calculation uses the direct arrival traveltimes (from shot to crossover point location) to find the velocity of the subweathering layer and the refracted arrival traveltimes (from the crossover point location to the end of survey or to an arbitrary offset limit) to establish the second layer velocity (Minus time analysis). Figures 4.19 and 4.20 show the velocity models from the *P*-wave arrivals and *S*-wave arrivals, respectively. A median filter (window length of 7 samples) was applied to both models to reduce short wavelength variation. The average *P*-wave velocities for the first and second layer are respectively 1968 m/s and 3006 m/s, while the average *S*-wave velocity for the first layer is 465 m/s and 1181 m/s for the second layer. The first layer *P*-wave velocity increases at both ends of the survey. The increase of the *P*-wave velocity coincides with an increase of the crossover point offsets.  $V_p/V_s$  is 4.2 for the first layer and 2.5 for the second layer.

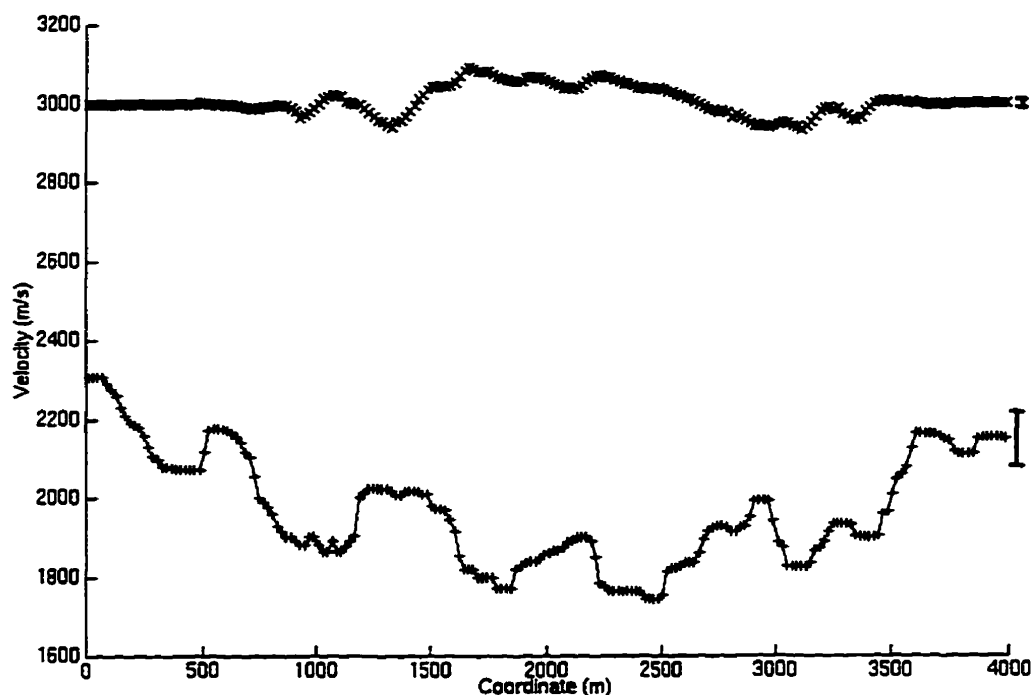


Figure 4.19. *P*-wave velocity model calculated from the *P*-wave arrival traveltimes: first layer velocity (+) and second layer velocity (x). Both velocities were median filtered with a window length of 7 samples.

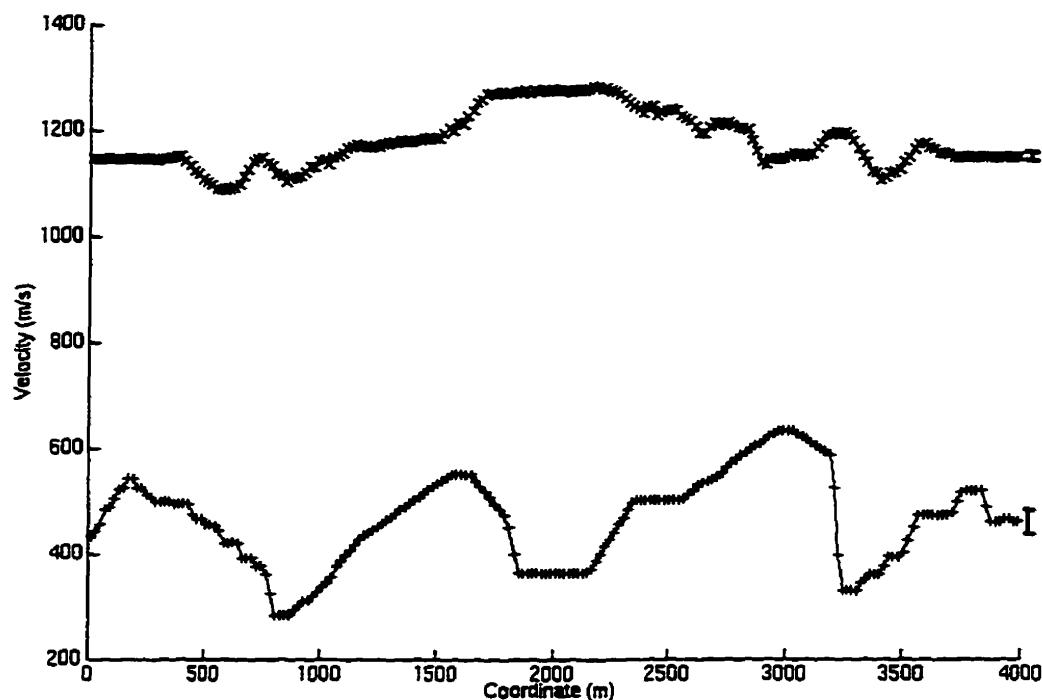


Figure 4.20. *S*-wave velocity model calculated from the *S*-wave arrival traveltimes: first layer velocity (+) and second layer velocity (x). Both velocities were median filtered with a window length of 7 samples.

#### 4.3.5 Plus time and Delay time analyses

The Plus time analysis process was undertaken on both *P*-wave and *S*-wave refractions according to the respective crossover point average locations and a user-selected offset limit. An offset limit of 3000 metres, which constrained the Plus-Minus time analysis window, was used to remove suspected third layer refracted arrivals from the computation. Figure 4.21 shows the Plus time average values at each receiver with the corresponding statistics (standard deviation and fold) for the *P*-wave refractions, while Figure 4.22 shows the results for the *S*-wave refractions. The average Plus time values for the entire line is 72 ms for the *P*-wave and 381 ms for the *S*-wave. The average standard deviation is 8 ms for the *P*-wave and 105 ms for the *S*-wave. The standard deviation increases abruptly at both ends of the survey because the Delay time analysis was used in replacement of the Plus time analysis, which is limited by the Plus-Minus time analysis window. Delay times for receivers outside the Plus-Minus time analysis window were found using the shot Delay times, which are calculated from the known Plus time values of receivers at the same locations (Lawton, 1989). The fold at the survey extremities is less than at the other surface locations because the delay time analysis uses only one shot spread at a time while Plus time analysis uses all the possible combinations of two shot spreads.

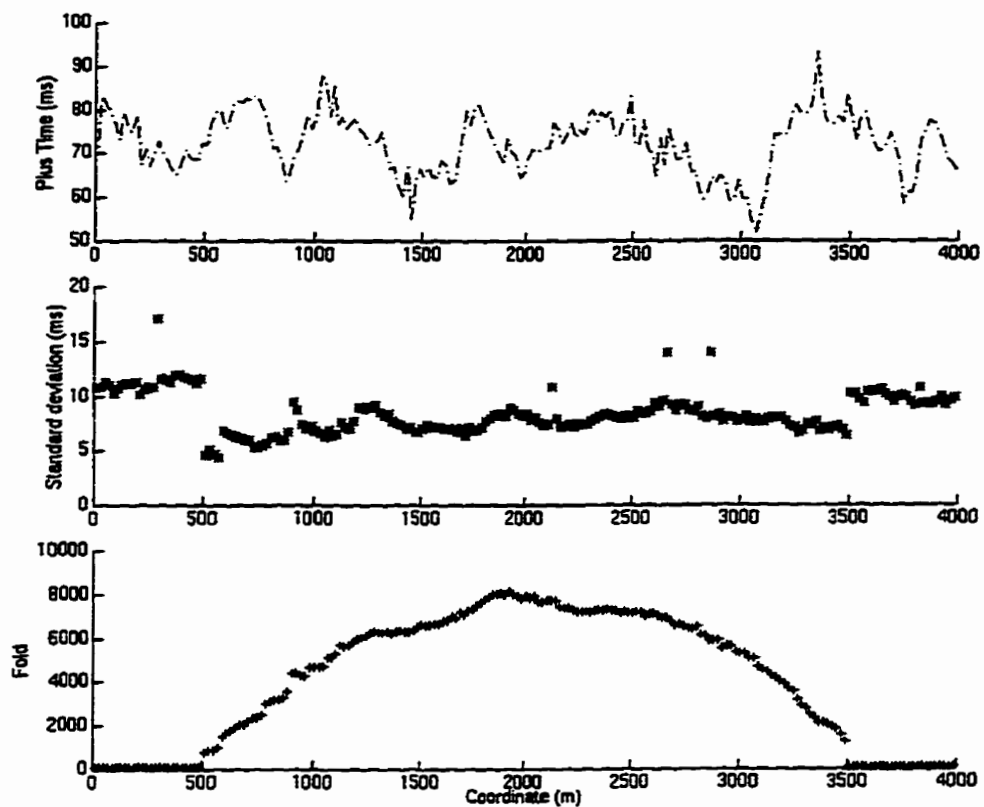


Figure 4.21. Plus time values and statistics for the *P*-wave refractions.

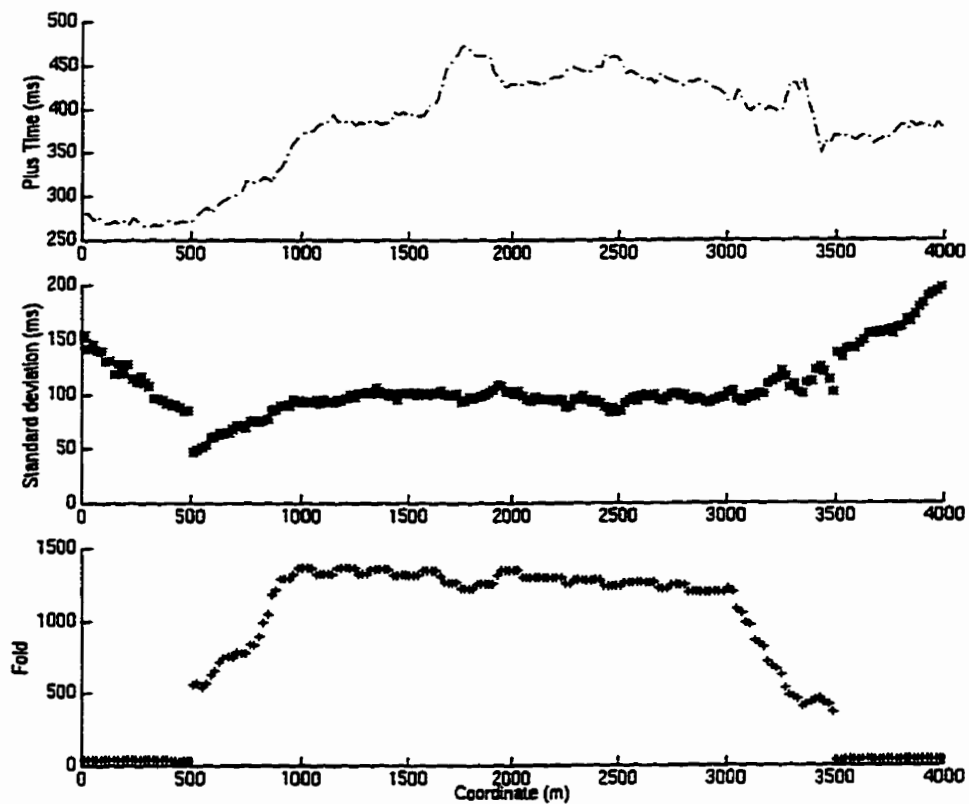


Figure 4.22. Plus time values and statistics for the *S*-wave refractions.

### 4.3.6 Depth model

The first layer thickness calculations were undertaken using the velocities and the Plus time values. For the *P*-wave and *S*-wave depth model calculations, constant first layer velocity of 1968 m/s and 465 m/s, respectively, were used instead of the calculated velocities to reduce the short wavelength variation due to arrival picking errors and lack of near-offset receiver coverage. Figure 4.23 shows the *P*-wave depth model and the corresponding statistics (standard deviation and fold), while Figure 4.24 displays the *S*-wave model. The average thickness of the first layer is of 94 metres for the *P*-model and of 96 metres for the *S*-model. The average standard deviation is 11 meters for the *P*-wave and 27 metres for the *S*-wave. In both cases, the first layer includes the thin surficial glacial deposits and the shale. The second layer which has a *P*-wave velocity of about 3000 m/s and *S*-wave velocity of about 1200 m/s is probably composed of a more compacted and coarser-grained sandstone of the Paskapoo Formation.

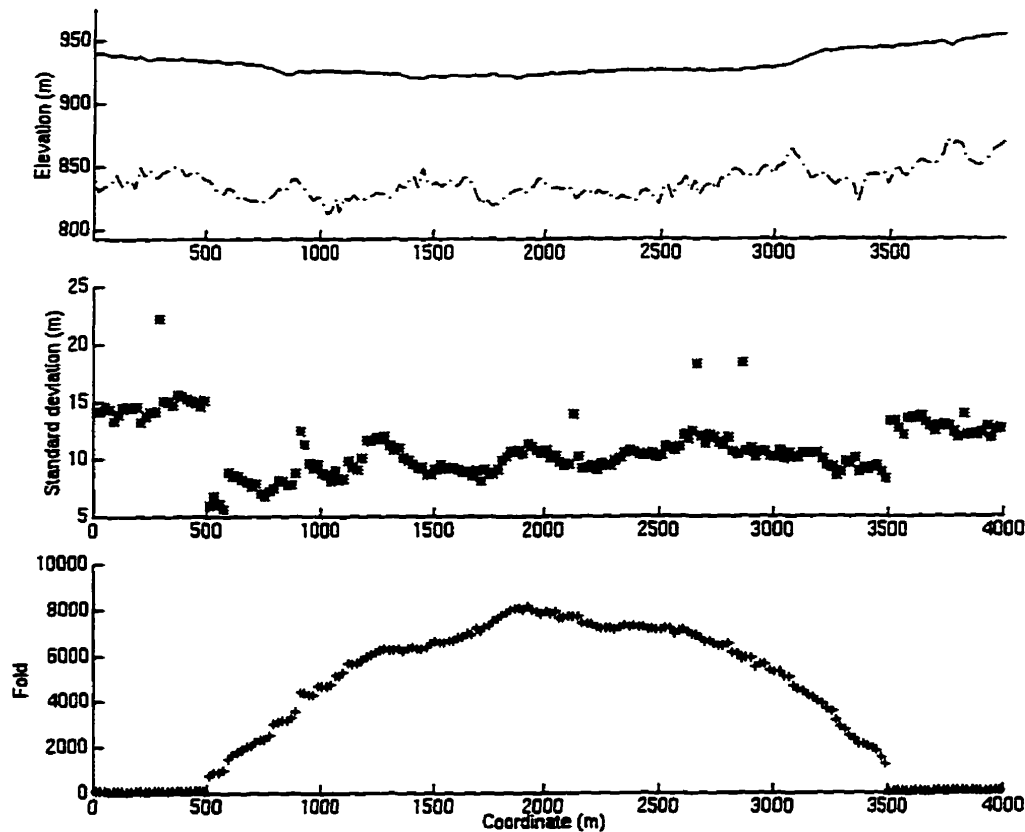


Figure 4.23. *P*-wave depth model and statistics (vertical exaggeration = 6).

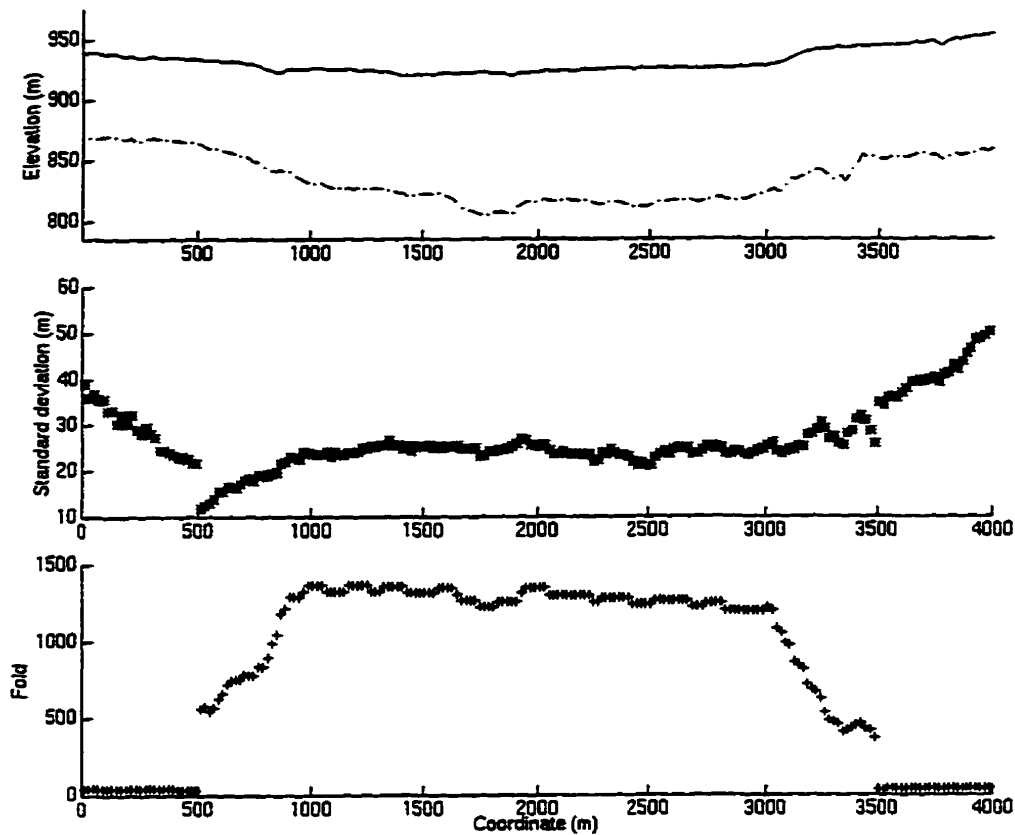


Figure 4.24. *S*-wave depth model and statistics (vertical exaggeration = 6).

#### 4.3.7 Static corrections

With the *P*-wave and *S*-wave models (depths and velocities) known, the static corrections were computed. Figures 4.25 and 4.26 show the surface-consistent elevation corrections, weathering corrections and total corrections for the *P*-wave model and *S*-wave models. The datum elevation used was 930 metres, which is the average surface elevation. The replacement velocity was 3100 m/s for the *P*-wave model and 1200 m/s for the *S*-wave model.



Figure 4.25. Surface-consistent static corrections established from the *P*-wave model: elevation corrections (\*), weathering corrections (+), and total corrections (o).

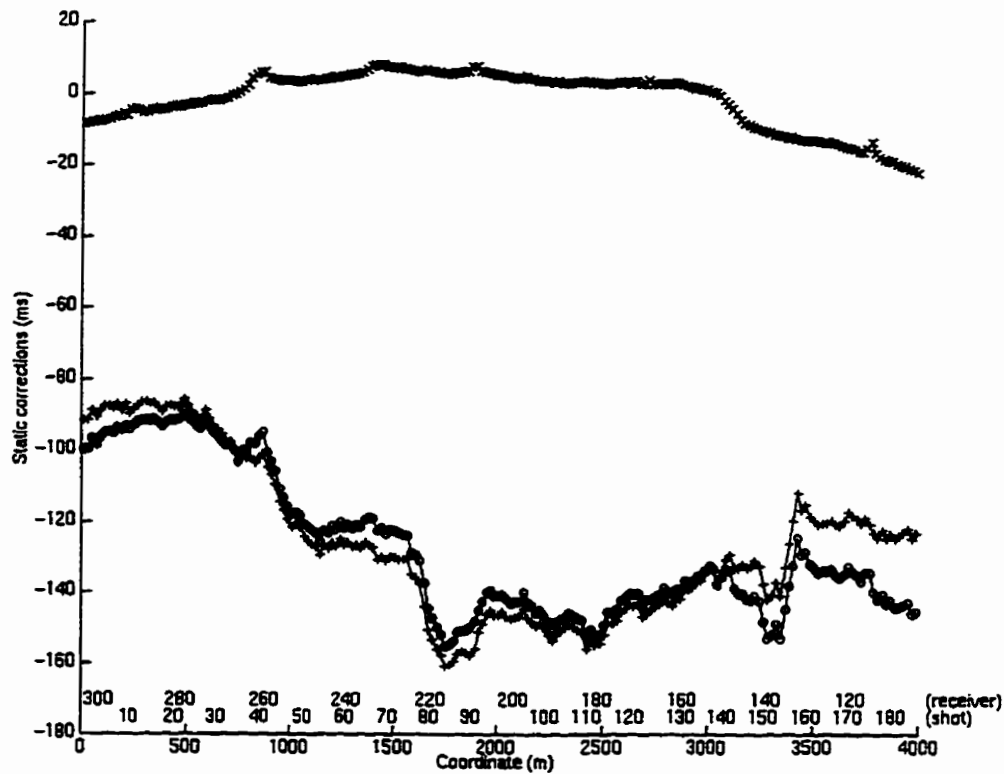


Figure 4.26. Surface-consistent static corrections established from the *S*-wave model: elevation corrections (\*), weathering corrections (+), and total corrections (o).

#### 4.4 GENERALIZED LINEAR INVERSION ANALYSIS

The Generalized Linear Inversion (GLI) method by Hampson and Russell (1984) uses an input model and its calculated refracted traveltimes to compare and to match them with the observed refracted traveltimes by updating the model iteratively (Hampson and Russell, 1984). The GLI method was used to provide a comparison with the PMT method.

##### 4.4.1 Initial input model

The first step of the Generalized Linear Inversion method is to build an approximate near-surface model. The model is built using a slope picking process of the refracted arrivals in an offset window. The same refracted arrival traveltimes ( $P$  and  $S$ ) used for the Plus-Minus time analysis method were used to build the  $P$ -wave and  $S$ -wave input models. Figure 4.27 displays all the  $P$ -wave refracted arrival traveltimes in term of offset, as well as the initial input model (straight-line). The initial  $P$ -wave model has a first layer velocity of 1968 m/s and a second layer velocity of 3168 m/s. The initial first layer thickness is of 95 metres, according to the intercept time of 76 ms. Similarly, the  $S$ -wave refracted arrival traveltimes with the initial input model (straight line-slope) are shown in Figure 4.28. The initial  $S$ -wave velocities are 465 m/s and 1325 m/s for the first and second layer, respectively. The initial first layer thickness is of 87 metres (intercept time of 350 ms).

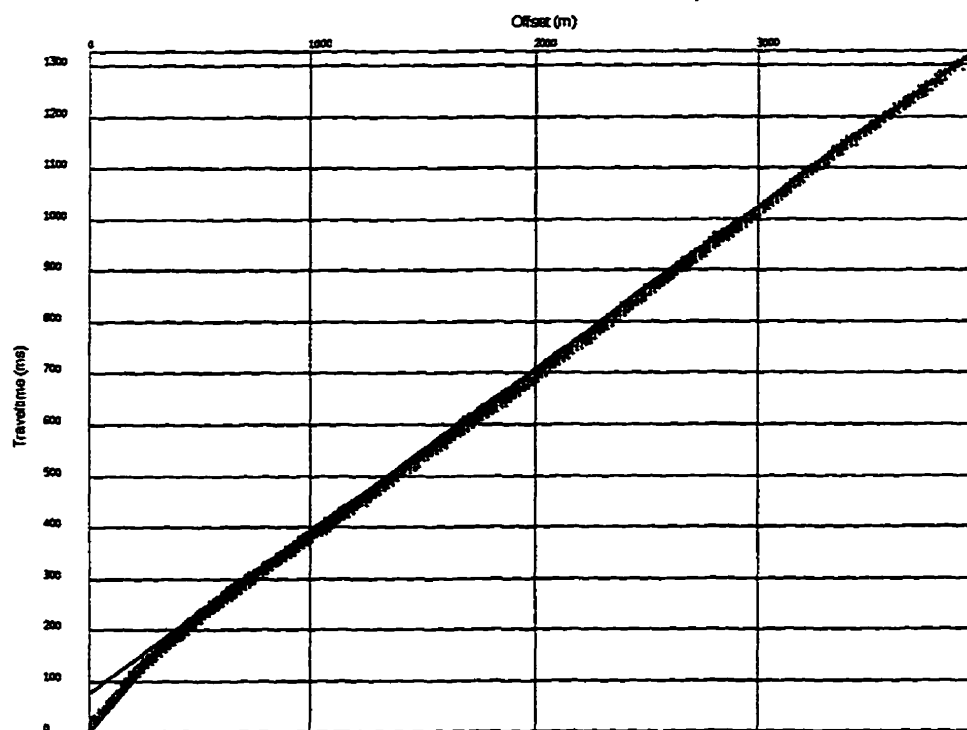


Figure 4.27.  $P$ -wave refracted arrival traveltimes versus offset and initial input  $P$ -wave model (straight line-slope).

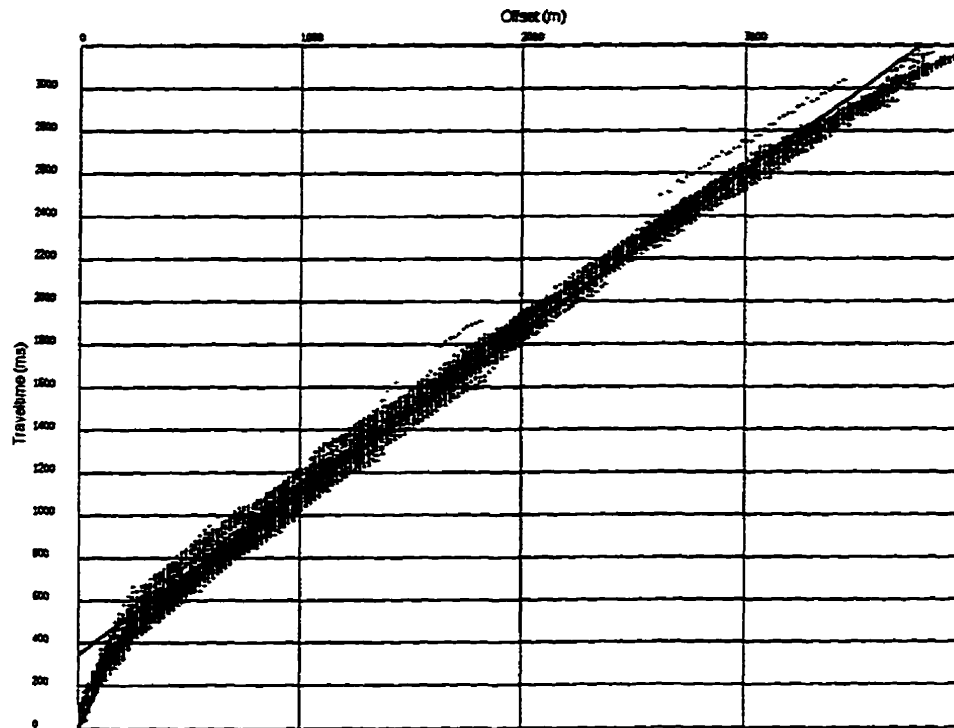


Figure 4.28. *S*-wave refracted arrival traveltimes versus offset and initial input *S*-wave model (straight line-slope).

#### 4.4.2 Final inverted model

From the initial input models (*P* and *S*), arrival traveltimes are calculated using a simple raytracing method (straight raypath and locally flat layer). The inversion procedure consists of sequentially modifying the thickness and velocity of the input model to get a closer match of the calculated arrival traveltimes with the observed arrival traveltimes (Gauss-Seidel iteration and conjugate-gradient algorithm, Hampson and Russell, 1984). Like with the Plus-Minus time analysis, an offset limit of 3000 metres was used to avoid third layer arrivals in the analysis, which can be seen in Figure 4.28. To stabilize the inversion, a depth smoother of 150 metres and a velocity smoother of 1500 metres were used. GLI method uses ray-tracing to perform forward modelling, so that the model must be smoothed to prevent instability. For example, a long smoother length gives a very stable model, but of low resolution. Therefore, a separate short-wave calculation is needed after the inversion. During the inversion, both the thickness and the velocities can change to provide a better fit of the modelled traveltime with the observed traveltime. The result of the inversion on the *P*-wave and *S*-wave model is expressed in term of variation in the first layer thicknesses and the first and second layer velocities.

The average thickness of the inverted *P*-wave depth model is 93 metres and the average second layer velocity is 3190 m/s, while the first layer velocity remains unchanged. The average thickness of the first layer for the *S*-wave model is 91 metres and the second layer velocity average is 1289 m/s.

## **4.5 COMPARISON OF PLUS-MINUS TIME ANALYSIS METHOD AND GENERALIZED LINEAR INVERSION METHOD RESULTS**

### **4.5.1 Depth model comparison**

The *P*-wave and *S*-wave depth models can be compared by looking at the elevation of the first and second layer interface. Figure 4.29 shows the elevation of the first and second layer interface of the *P*-wave depth model for the Plus-Minus time analysis (PMT) and Generalized Linear Inversion (GLI) methods, whereas Figure 4.30 displays the elevation of the first and second layer interface of the *S*-wave model for the two methods. The elevation average for the *P*-wave depth model is 837 metres with the PMT method and 838 metres with the GLI method, while the elevation average for the *S*-wave depth model is 835 metres with the PMT method and 841 metres with the GLI method. When comparing the interface elevations for the *P*-wave models, it is noticed that GLI elevations track the PMT elevations. The GLI elevations are smoother due to the depth smoother used (150 metres). If we look at the *S*-wave interface elevations, the PMT and GLI elevations have the same shape, although there is a constant elevation difference in the middle of the survey line and greater elevation differences for the PMT interface. In terms of the average first layer thickness for the *P*-models, the PMT model is 94 metres and GLI model is 93 metres, whereas for *S*-models, the PMT model is 96 metres and GLI model is 91 metres. The discrepancy between the GLI and PMT model is more important for the *S*-model. This can be explained in part by the poorer quality of the *S*-wave refraction picking which results in a less constrained arrival traveltimes range (Figure 4.28). To obtain a well defined near-surface model, GLI method counts on the rejection of some refracted arrivals that have traveltimes too far from the calculated traveltimes based on an input model. While, the PMT method depends strictly on the statistical redundancy of the refracted arrivals at each location. The average of PMT and GLI models results in the same average thickness for *P* and *S* models, i.e. 94 metres.

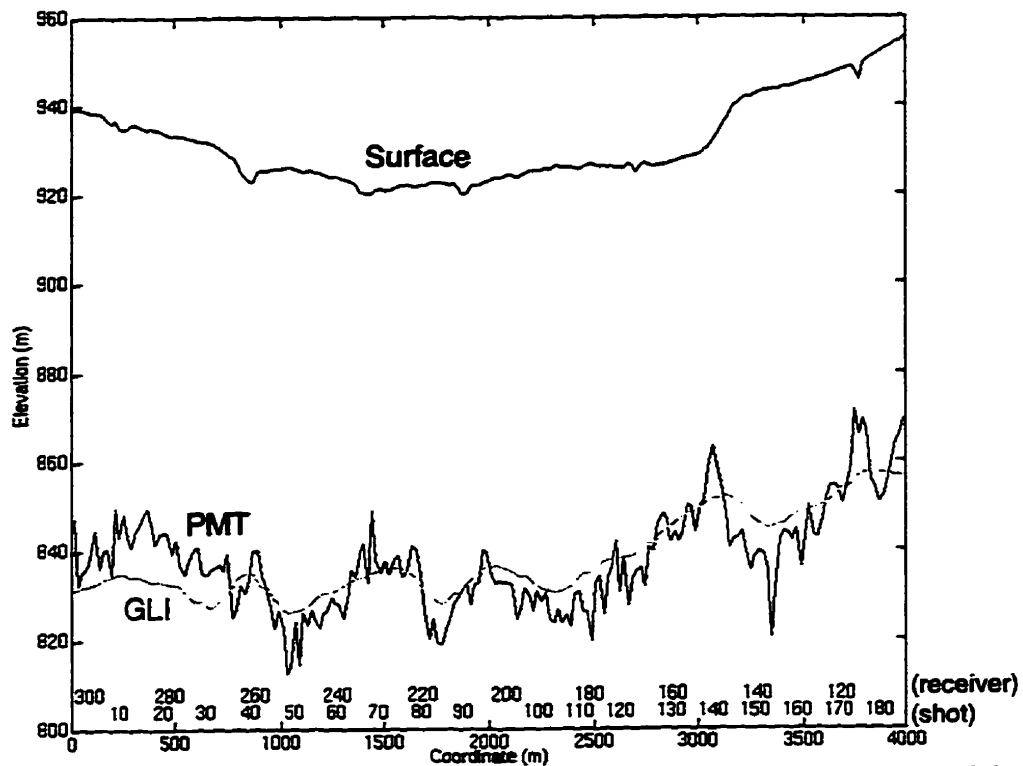


Figure 4.29. First and second layer interface elevation for the *P*-wave models: PMT method (x) and GLI method (o) (vertical exaggeration = 22).

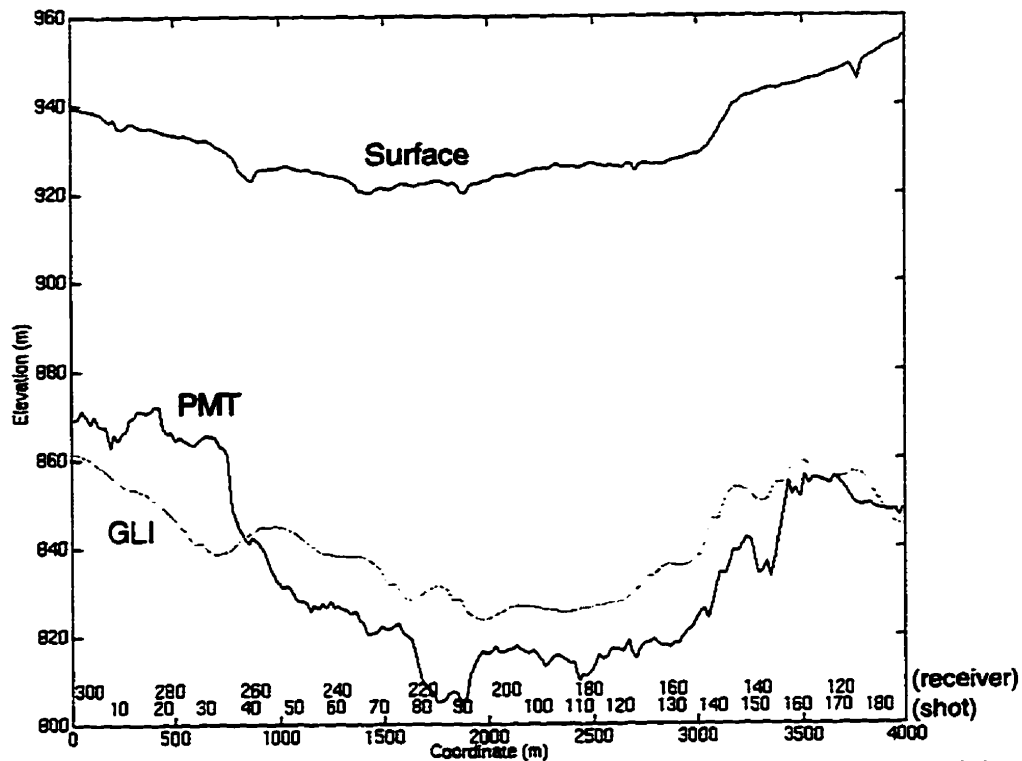


Figure 4.30. First and second layer interface elevation for the *S*-wave models: PMT method (x) and GLI method (o) (vertical exaggeration = 22).

#### 4.5.2 Static solution comparison

From the *P*-wave and *S*-wave models, static corrections were computed. The datum used for both PMT and GLI models was 930 metres. The replacement velocity for the *P*-wave models was 3100 m/s and 1200 m/s for the *S*-wave models. The receiver static corrections calculated from the *P*-wave models (PMT and GLI) are shown in Figure 4.31. The two solutions are very similar in terms of long wavelength character. Figure 4.32 displays the receiver static corrections for the *S*-wave models (PMT and GLI). Again, both solutions express the same features with a constant difference of about 20 ms in the middle of the survey line (receiver number 135-250). However, differences between the PMT and GLI static solutions occur at the beginning and at the end of the survey line. The receiver static corrections coming from the *P*-models can be applied to the vertical component data, while the receiver static corrections calculated from the *S*-models are for the radial component data. The shot static corrections computed from the *P*-models are used for both vertical and radial component data. Figure 4.33 shows the shot static corrections established from the *P*-models and the shot hole depth. Both PMT and GLI solutions have similar values with some differences in terms of intermediate and high frequencies statics.

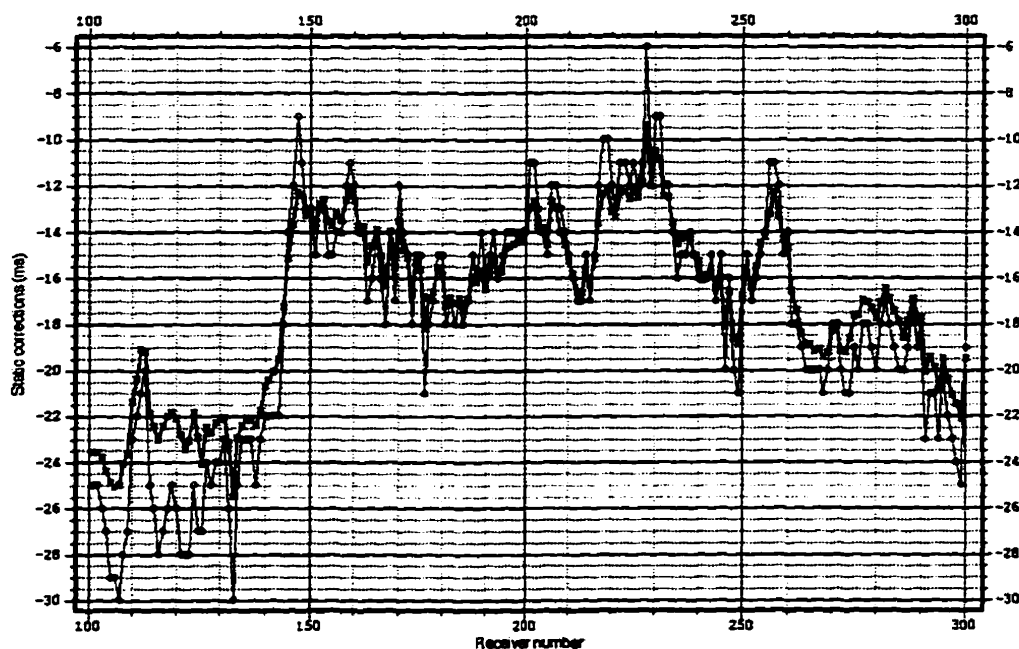


Figure 4.31. Receiver static corrections (weathering + elevation) from the *P*-models: PMT (x) and GLI (o).

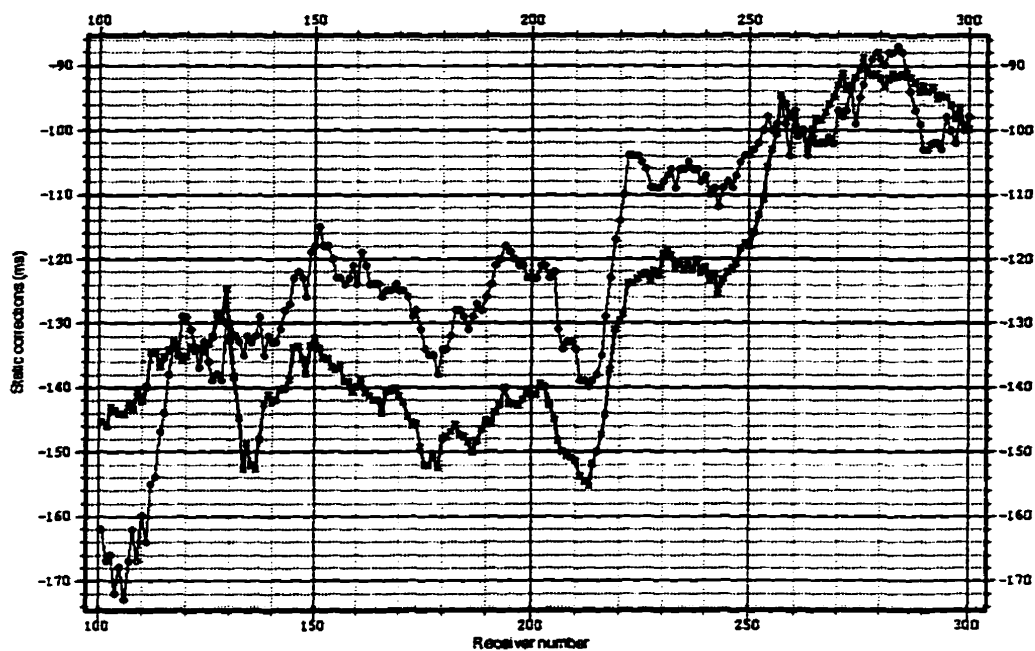


Figure 4.32. Receiver static corrections (weathering + elevation) from the *S*-models: PMT (x) and GLI (o).

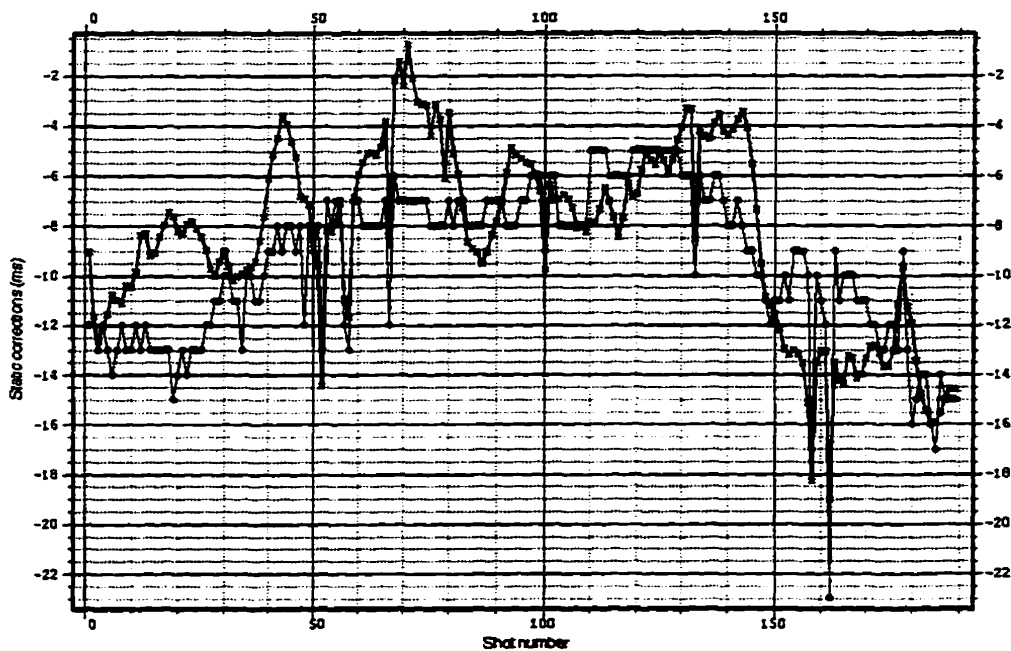


Figure 4.33 Shot static corrections (weathering + elevation) from the *P*-models: PMT (x) and GLI (o).

#### 4.5.3 Common receiver stack comparison

Common receiver stacks were produced from the vertical and the radial component data. The shot static corrections calculated from the *P*-model are used for both component data

(vertical and radial). The receiver static corrections calculated from the  $P$ -model are used for the vertical component data, while the receiver static corrections computed from the  $S$ -model are applied to the radial component data. The quality of a common receiver stack and the efficiency of the static corrections applied can be determined looking at the reflector structure and continuity (receiver static corrections), as well as the energy focus (shot static corrections).

### *Vertical component*

Figures 4.34, 4.35 and 4.36 show the vertical component common receiver stacks without any static correction, with the PMT static solutions and GLI static solutions applied, respectively. Both common receiver stacks with the PMT and GLI static solutions show clear improvement compared to the common receiver stack without static corrections. The static corrections have successfully removed the false reflector time structure, enhanced the reflector continuity, and have provided better energy focus. Both PMT and GLI solutions give comparable results.

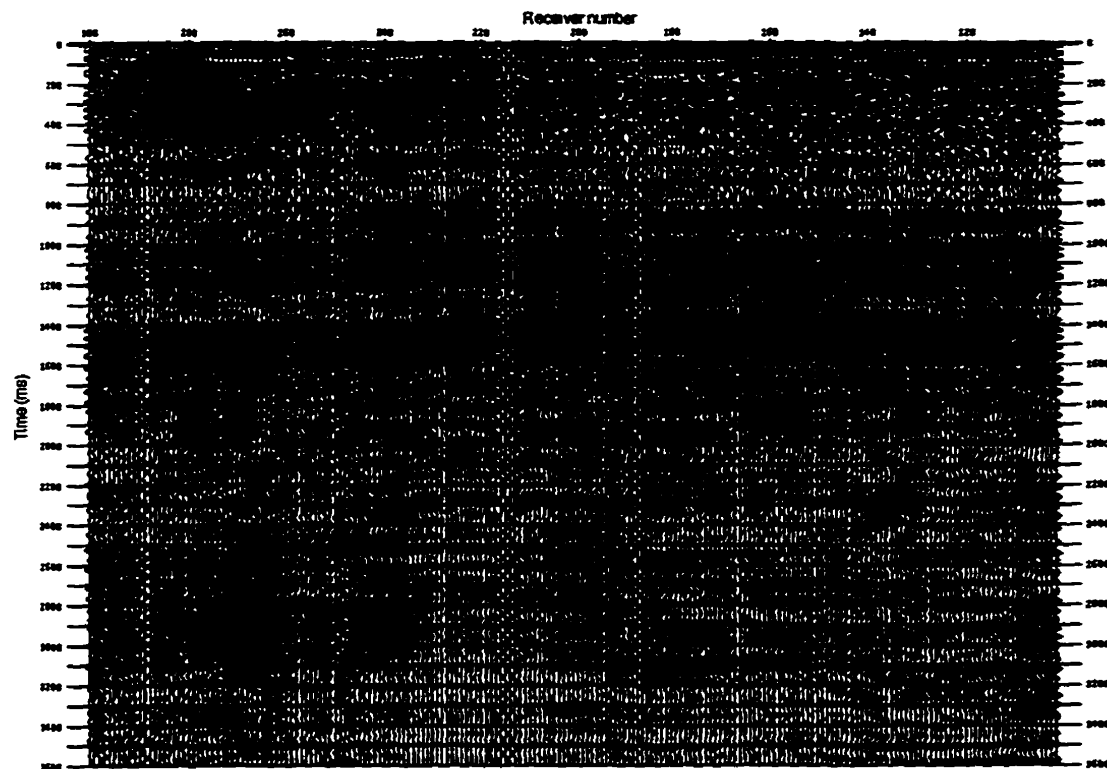


Figure 4.34. Vertical component common receiver stack (raw).

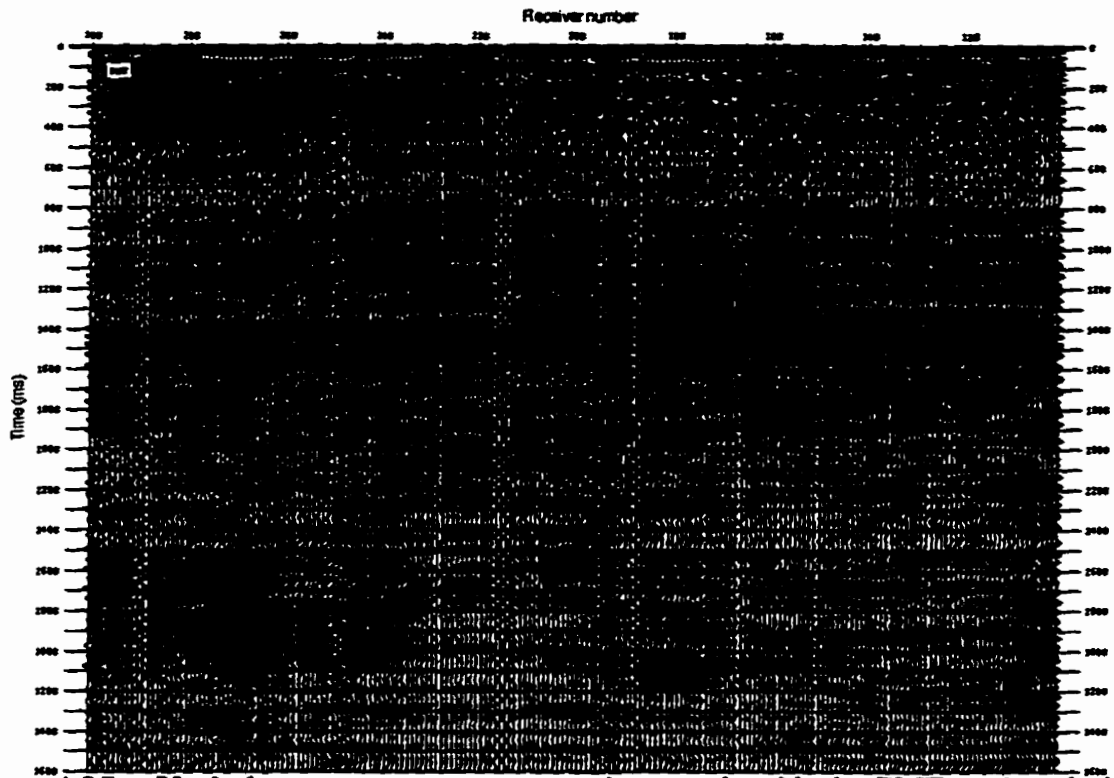


Figure 4.35. Vertical component common receiver stack with the PMT static solutions (receiver and shot static corrections from the *P*-model).

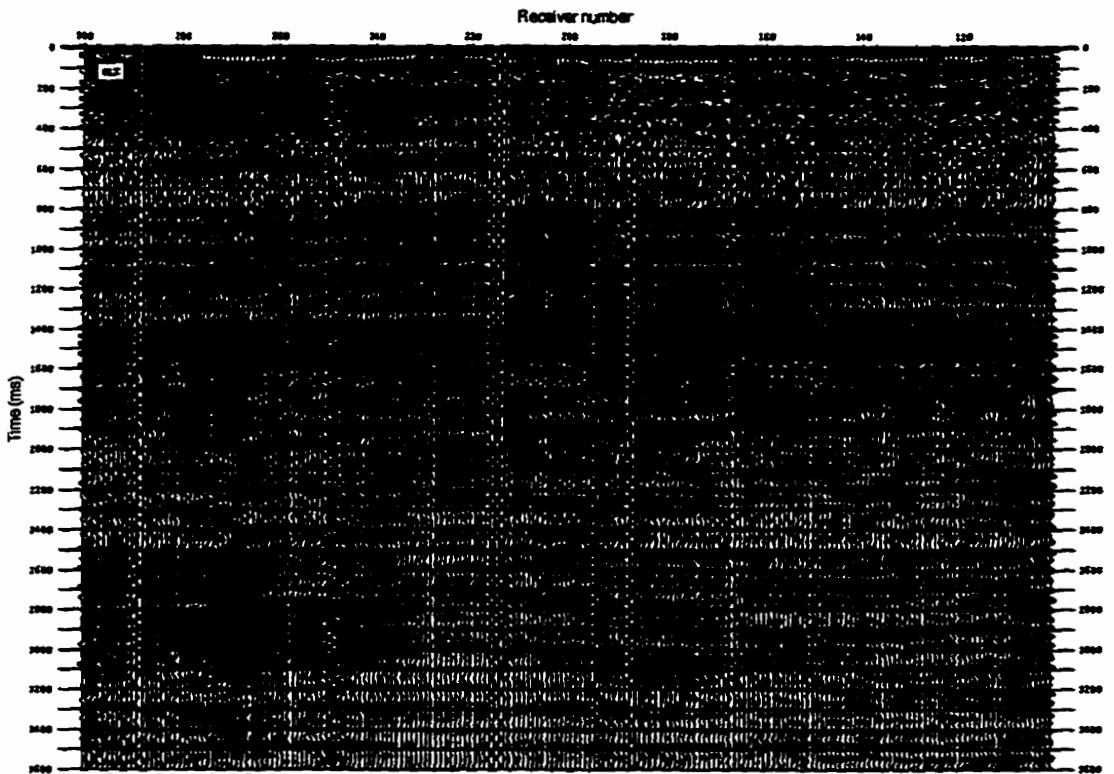


Figure 4.36. Vertical component common receiver stack with the GLI static solutions (receiver and shot static corrections from the *P*-model).

### *Radial component*

Figures 4.37, 4.38 and 4.39 show respectively the radial component common receiver stacks without static correction, with the PMT static solutions and GLI static solutions applied. There is an improvement to the common receiver stack with the PMT and GLI static solutions applied in comparison with the raw common receiver stack. The static corrections did remove some false reflector time structure and enhanced the reflector continuity. However, the improvement is not as obvious and significant as the improvement on the vertical component, also the PMT and GLI static solutions both seem to have added some long wavelength reflector structure. Figure 4.40 displays a reflector horizon before and after the static solutions were applied. It can be noticed that a reflector structure is being added in the middle of the survey line, around receiver number 210, which corresponds to an increasing thickness of the first layer in the PMT *S*-wave model in between coordinate 1500 to 2000 metres (receiver numbers 200 to 230 in Figure 4.30). This feature has a thickness of about 10 metres and is believed to be a paleochannel. The paleochannel might be composed of coarser materials (silt-sand) than the average first layer (shale) so that the local seismic velocities should be faster. Therefore, the use of a constant first layer velocity will cause an overestimation of the static corrections for this feature.

The increasing receiver static correction values (PMT and GLI) towards the middle and the end of the survey line are due to an increasing first layer thickness trend in the *S*-model. Therefore, a long wavelength time structure trend is being added to the reflector. However, removal of some intermediate wavelength apparent-reflector structure has been achieved, especially along the first half of the survey line. As a result of the application of the static corrections, the sections have been moved to earlier times. Difference between the reflector structure with the PMT static solutions and the reflector structure with the GLI static solutions is less obvious. The PMT static solutions give a better result at the end of the survey line between coordinate 3500 to 4000 metres (receiver numbers 101 to 130).

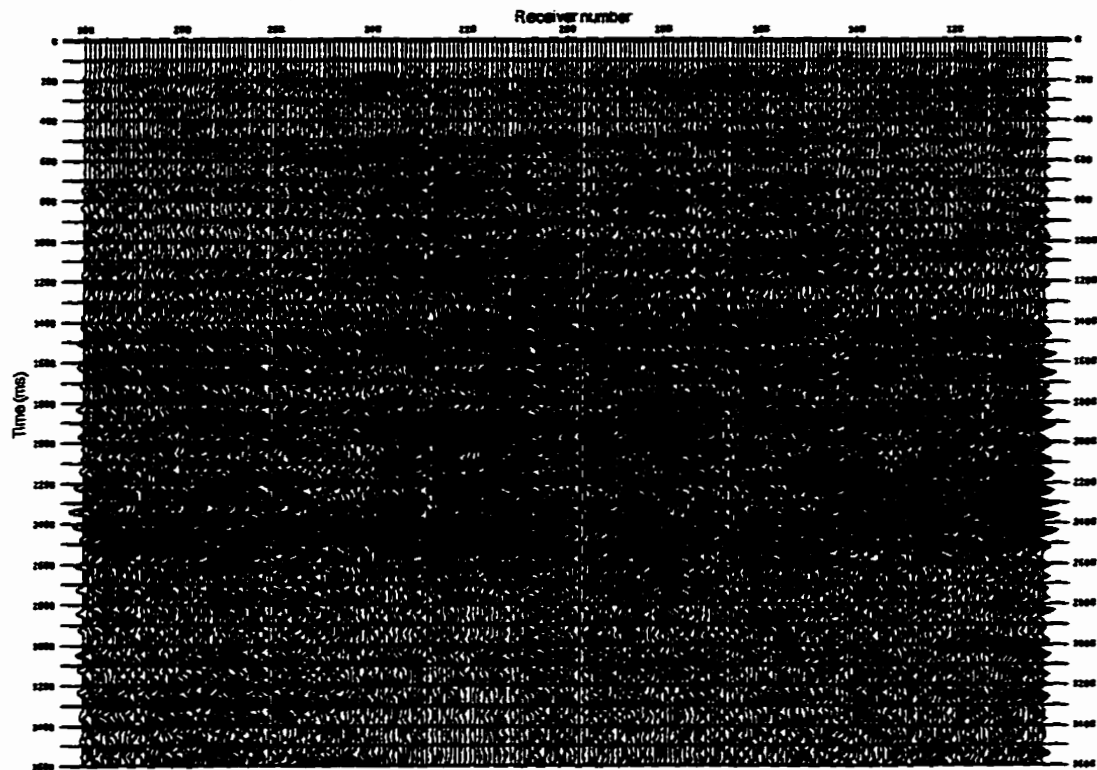


Figure 4.37. Radial component common receiver stack (raw).

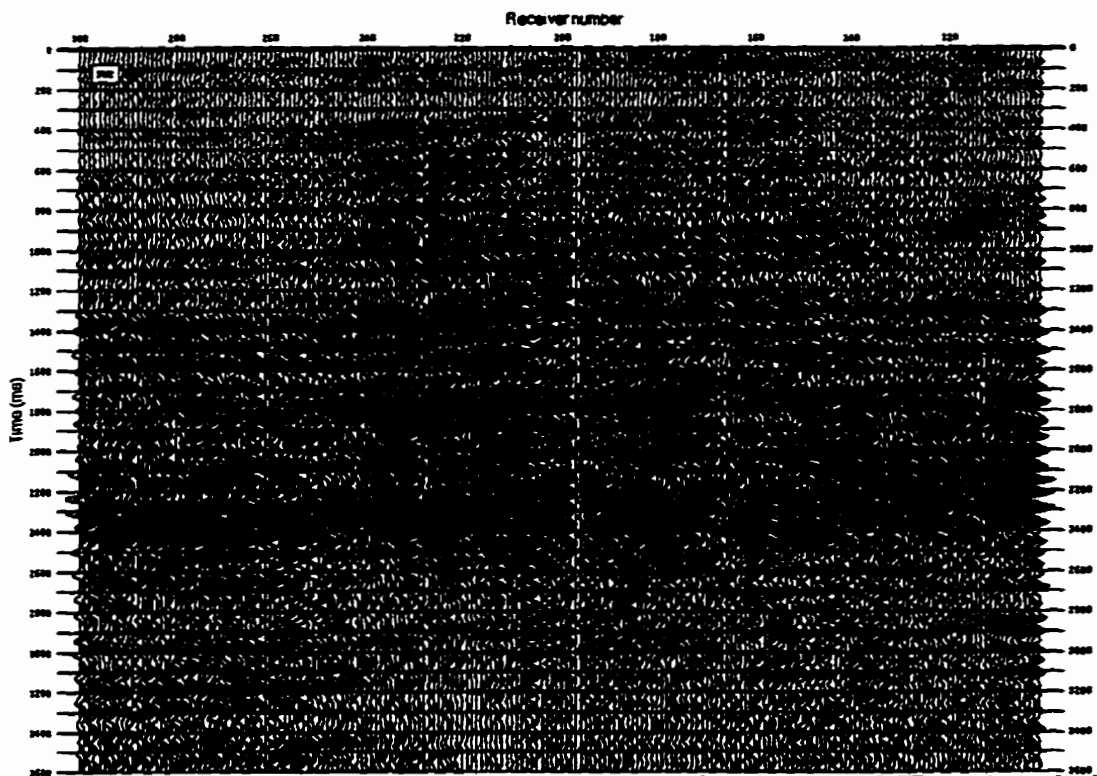


Figure 4.38. Radial component common receiver stack with the PMT static solutions (receiver static corrections from the *S*-model and shot static corrections from the *P*-model).

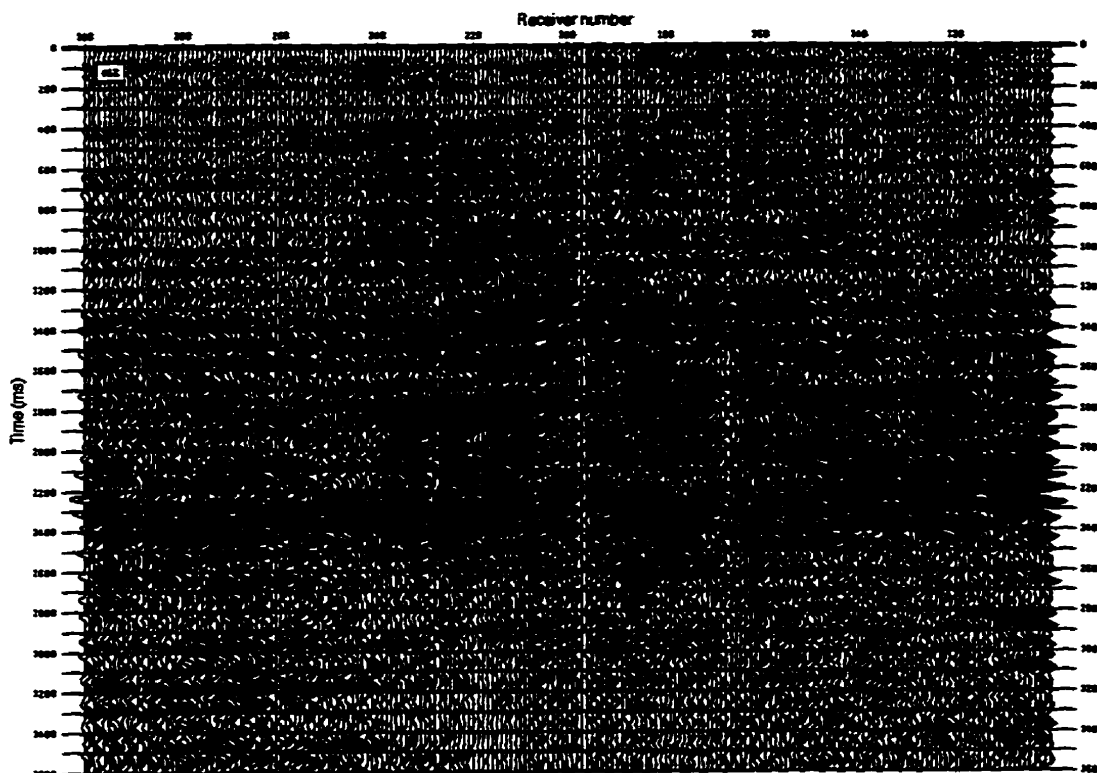


Figure 4.39. Radial component common receiver stack with the GLI static solutions (receiver static corrections from the *S*-model and shot static corrections from the *P*-model).

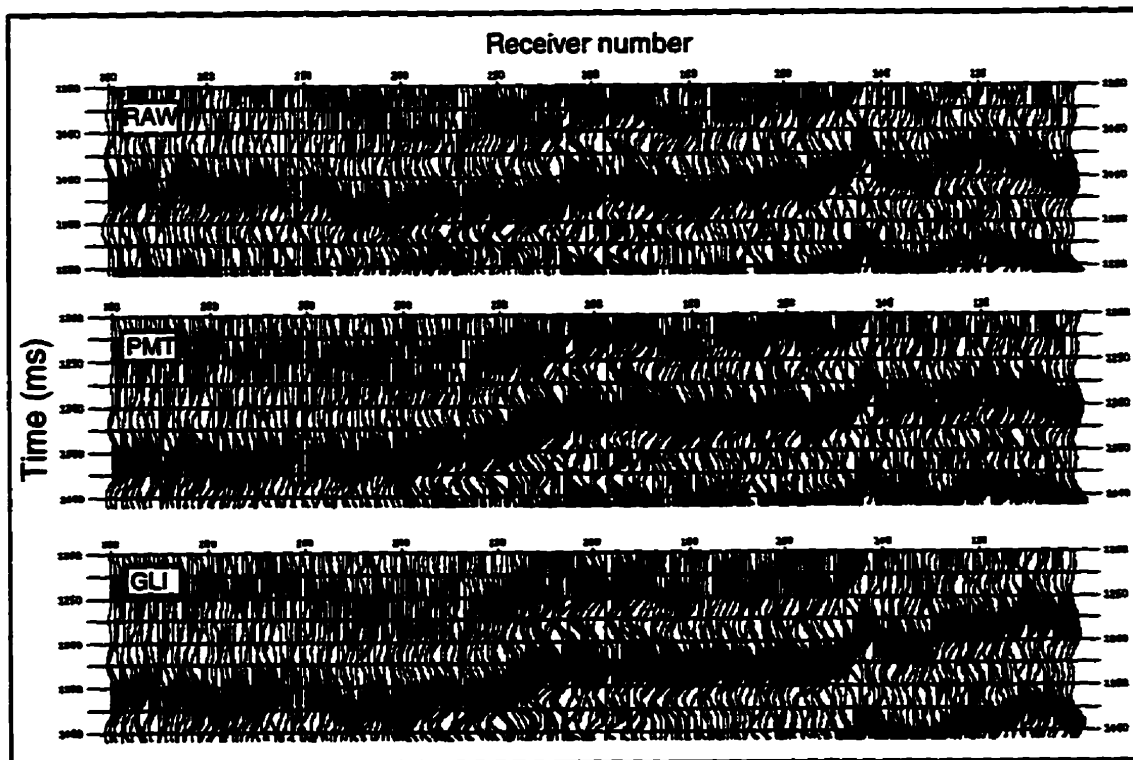


Figure 4.40. Horizon time structure comparison for a common reflector on the radial component data before and after static corrections applied (PMT and GLI static solutions).

#### 4.5.4 Common source stack comparison

Common source stacks were produced using the radial component only, to provide further comparison of the PMT and GLI methods. The static corrections applied were the same as for the common receiver stack ( $P$ -source static corrections and  $S$ -receiver static corrections). The evaluation of the quality of a common source stack and the efficiency of the static corrections applied can be determined looking at the reflector structure and continuity (source static corrections), as well as the energy focus (receiver static corrections). Figures 4.41, 4.42 and 4.43 show respectively the radial component common source stacks without any static correction, with the PMT static solutions and GLI static solutions applied. Both common source stacks with the PMT and GLI static solutions show clear improvement compared to the common source stack without static corrections. The static corrections (PMT and GLI) have successfully removed apparent reflector time structure, enhanced the reflector continuity, and have provided better energy focus. However, the quality of the stack, in the beginning of the section (stations 120 to 189), has been degraded with the addition of the static corrections (PMT and GLI). The PMT static solutions produce a better stack compare to the GLI static solutions, in terms of energy focus and reflector continuity. The receiver static corrections influence the energy focus and the source static corrections impact on the reflector continuity.

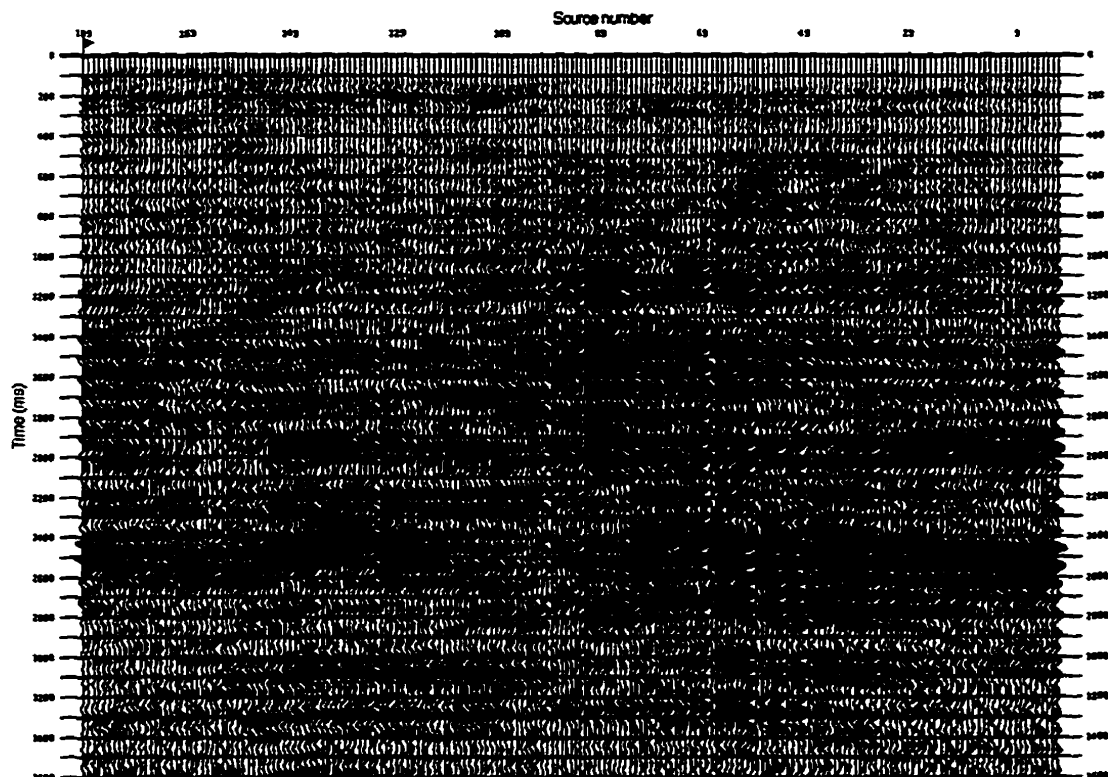


Figure 4.41 Radial component common source stack (raw).

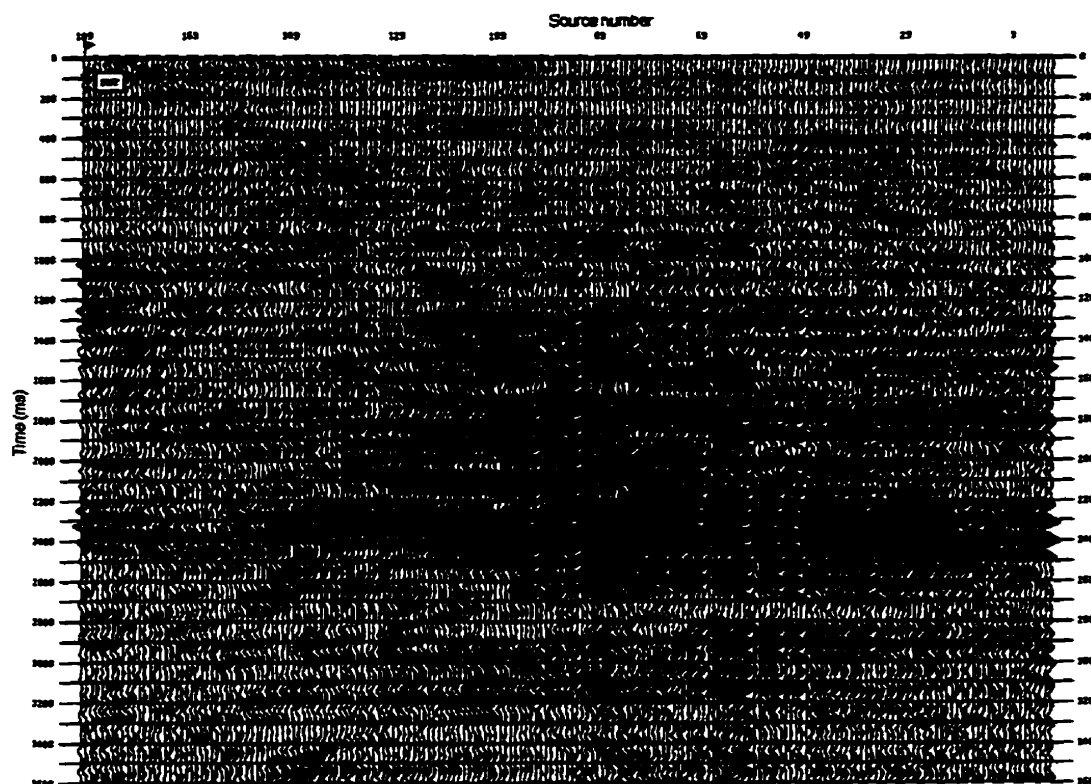


Figure 4.42. Radial component common source stack with the PMT static solutions (receiver static corrections from the *S*-model and shot static corrections from the *P*-model).

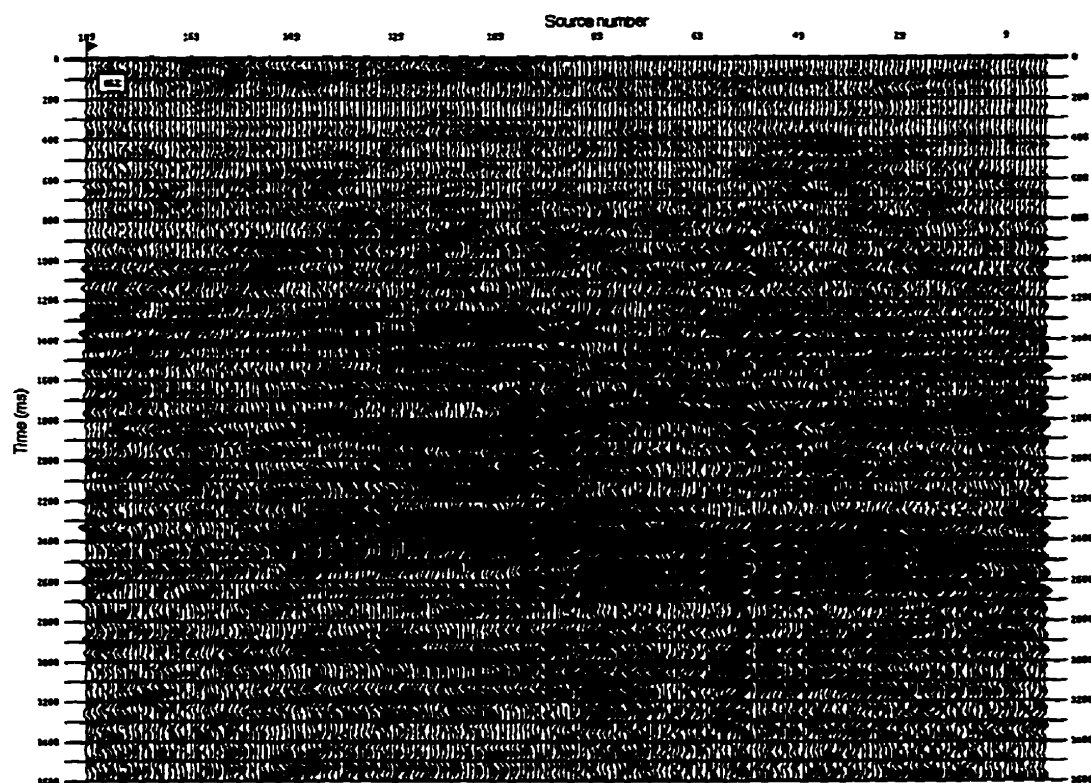


Figure 4.43. Radial component common source stack with the GLI static solutions (receiver static corrections from the *S*-model and shot static corrections from the *P*-model).



of the radial component common source stacks has clearly shown improvement in terms of energy focus and reflector continuity for the stack sections with the static corrections applied (PMT and GLI). Also, the PMT static solutions provide better results than the GLI static solutions.

The use of static corrections based on the near-surface models ( $P$  and  $S$ ) instead of hand picking corrections remains more meaningful and physically realistic (Schafer, 1991). The removal of the intermediate and long wavelength statics should facilitate the short-wavelength residual static computation.

## **FUTURE WORK**

Currently, the Plus-Minus time analysis method works only for simple 2 layer 2-D models. The method should be extended to 3-D and allow more complex near-surface layering (3 or more layers).

A shear-refraction analysis on other 3-component dataset will help establish how reliable the  $S$ -wave refractions are to image the near-surface. Furthermore, the extraction of the  $S$ -wave refractions using more efficient filters should enhance the quality of the refracted arrival picks. Therefore, a more accurate near-surface model should result and more appropriate static corrections can be applied to data.

## REFERENCES

- Anno, P. D., 1986, Two critical aspects of shear-wave analysis: Statics solutions and reflection correlations, in Danbom, S. H., and Domenico, S. N., Eds., Shear-wave exploration: Soc. Expl. Geophys. Dev. Series, 1, 48-61.
- Anno, P. D. , 1987, Two critical aspects of shear-wave analysis: Statics solutions and reflection correlations, in Dambom, S. H., and Domenico, S. N., Eds., Shear Wave Exploration: Soc. Expl. Geophys., 48-61.
- Barry, K. M., 1967, Delay time and its application to refraction profile interpretation, in Musgrave, A. W., Ed., Seismic refraction prospecting: Soc. Expl. Geophys., 348-361.
- Cary, P. W., and Eaton D. W. S., 1993, A simple method for resolving large converted-wave (*P-SV*) statics: Geophysics, v.58, 429-433.
- Clague, J. J., 1991, Quaternary glaciation and sedimentation, Chapter 12 in geology of the Cordilleran Orogen in Canada, H. Gabrielse and C. J. Yorath (ed.): Geological Survey of Canada, Geology of Canada, no.4, 419-434.
- Corbin, R. J., Bell, D. W., and Danbom, S. H., 1987, Shear- and compressional-wave surface and downhole tests in southern Louisiana, in Dambom, S. H., and Domenico, S. N., Eds., Shear Wave Exploration: Soc. Expl. Geophys., 62-75.
- Domenico, S. N., 1984, Rock lithology and porosity determination from shear and compressional wave velocity: Geophysics, v.49, 1188-1195.
- Edelmann, H. A. K., and Helbig, K., 1988, Shear-wave surveys- some aspects of field layout, in Danbom, S. H., and Domenico, S. N., Eds., Shear-wave exploration: Soc. Expl. Geophys. Dev. Series, 1, 39-47.
- Ensley, R. A., 1984, Comparison of P- and S-wave seismic data: A new method for detecting gas reservoirs: Geophysics, v.49, 1420-1431.
- Gardner, L. W., 1939, An areal plan of mapping subsurface structure by refraction shooting: Geophysics, v.39, 292-301.
- Gardner, L. W., 1967, Refraction seismograph profile interpretation, in Musgrave, A. W., Ed., Seismic refraction prospecting: Soc. Expl. Geophys., 338-347.
- Geiger, K. W., 1967, Bedrock topography of the Gleichen area, Department of Energy, Mines and Resources, Ottawa.
- Gregory, A. R., 1976, Fluid saturation effects on dynamic elastic properties of sedimentary rocks: Geophysics, v.41, 895-921.

- Hagedoorn, J. G., 1959, The Plus-Minus method of interpreting seismic refraction sections, *Geophysical Prospecting* 7, 158-182.
- Hampson, D., and Russell, B., 1984, First break interpretation using generalized linear inversion: *J. Soc. Expl. Geophys.*, 20, 40-54.
- Hawkins, L. V., 1961, The reciprocal method of routine shallow seismic refraction investigations: *Geophysics*, v.26, 806-819.
- Irish, E. J. W., 1967, Geology map of Gleichen area, Institute of Sedimentary and Petroleum Geology, Geological Survey of Canada.
- Jolly, R. N., 1956, Investigation of shear waves: *Geophysics*, v.21, 905-938.
- Jolly, R. N., and Mifsud, J. F., 1971, Experimental studies of source generated noise: *Geophysics*, v.36, 1138-1149.
- Jones, J. H., 1934, A seismic method of mapping anticlinal structures: *Proc. First World Pet. Cong.*, 169-173.
- Lawton, D. C., 1989, Computation of refraction static corrections using first-break traveltimes differences: *Geophysics*, v.54, 1289-1296.
- Lawton, D. C., 1990, A 9-component refraction seismic experiment: *Canadian Journal of Exploration Geophysicists*, v.26, 7-16.
- McGee, J. E., and Palmer, R. L., 1967, Early refraction practices, in Musgrave, A. W., Ed., *Seismic refraction prospecting: Soc. Expl. Geophys.*, 3-11.
- Pickett, G. R., 1963, Acoustic character logs and their applications in formation evaluation: *Journal of Petroleum Technologists*, 559-667.
- Ricker, N., and Lynn, R. D., 1950, Composite reflections: *Geophysics*, v.15, 30-50.
- Ricker, N., 1953, Forms and Laws of Propagation of Seismic Wavelets, *Proceedings of the World Petroleum Congress, 1951: Geophysics*, V.18, 1.
- Robertson, J. D., and Pritchett, W. C., 1985, Direct hydrocarbon detection using comparative P-wave and S-wave seismic sections: *Geophysics*, v.50, 383-393.
- Schafer, A. W., 1991, Binning, Static Correction, and Interpretation of P-SV Surface-Seismic Data, Thesis, University of Calgary.
- Sheriff, R. E., 1991, *Encyclopedic dictionary of exploration Geophysics*, third edition: *Soc. Expl. Geophys.*
- Stalker, A. Macs., 1957, Surficial geology of High River area, Geological Survey of Canada.
- Tatham, R. H., and Stoffa, P. L., 1976,  $V_p/V_s$  - A potential hydrocarbon indicator: *Geophysics*, v.41, 837-849.

- Teller, J. T., and Clayton, L., 1983, Glacial Lake Agassiz: Geological Association of Canada, Special Paper 26, 451 pp.
- Thornburgh, H. R., 1930, Wave-front diagrams in seismic interpretation, Bulletin of the American Association of Petroleum Geologists 14, 185-200.
- van Overmeeren, R. A., 1987, The plus-minus method for rapid field processing by portable computer of seismic refraction data in multi-layer groundwater studies: First Break, v.5, no.3, 83-94.
- Wang, W., and Cheadle, S., 1995, Branch point analysis in refraction interpretation, CSEG National Convention, Expanded abstracts.
- Wattrus, N. J., 1989, Inversion of ground roll dispersion: 59th Annual International Meeting, Soc. Expl. Geophys., Expanded Abstract, 946-948.
- Weatherby, B. B., 1940, The history and development of seismic prospecting: Geophysics, v.5, 215-230.
- Winterstein, D. F., and Hanten, J. B., 1985, Supercritical reflections observed in P- and S-wave data: Geophysics, v.50, 185-195.

## APPENDIX A : DELAY TIME ANALYSIS

A traditional method for refraction analysis is the “delay time” method introduced by Gardner in 1939. The Delay time analysis is based on the following equation, where  $t_s$  and  $t_r$  are the time from a shot ( $t_s$ ) and a receiver ( $t_r$ ) to the refractor minus the time necessary to travel the normal projection of the raypath on the refractor (see Equation A.1 and Figure A.1).

$$t_{sr} = t_s + sr/v_1 + t_r ; \text{ if } sr = ad; \quad (\text{A.1})$$

where  $t_{sr}$  equals the source-receiver traveltimes of the refracted raypath and  $v_1$  the velocity of the first refractor.

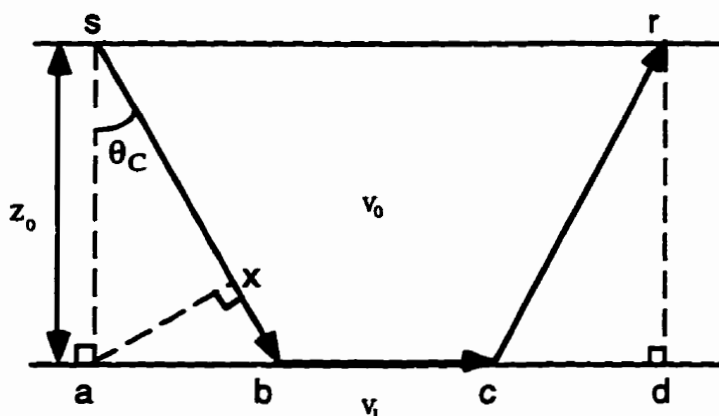


Figure A.1. Refracted raypath for a two layers model, i.e. a subweathering layer of  $z_0$  thickness and low velocity ( $v_0$ ), and a second undefined layer of high velocity ( $v_1$ ).

The Delay time for a shot ( $t_s$ ) and for a receiver ( $t_r$ ), based on Figure (A.1), can be expressed in the following manner:

$$t_s = sb/v_0 - ab/v_1 \quad (\text{A.2})$$

$$t_r = cr/v_0 - cd/v_1 \quad (\text{A.3})$$

Then the basic Delay time in equation (A.1) can be modified as follows:

$$t_{sr} = ab/v_1 + cd/v_1 + bc/v_1 + t_s + t_r \quad (\text{A.4})$$

Equation (A.1) corresponds to the equation of a straight line with a slope equal to  $1/v_1$ , and a time intercept ( $t_i$ ) of  $t_s + t_r$  (Figure A.2).

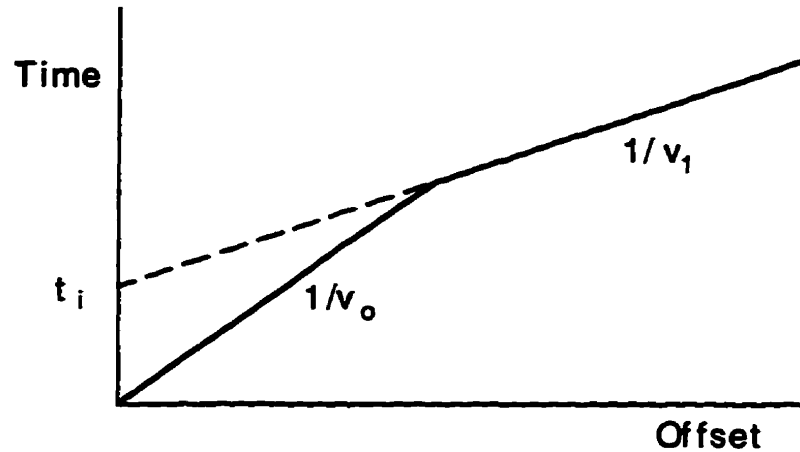


Figure A.2. First-arrivals traveltimes in function of source-receiver offset distance based on the two layers model in Figure (A.1).

From there, it can be demonstrated that:

$$t_i = t_s + t_r = 2 z_0 \cos \theta_c / v_0 \quad (\text{A.5})$$

where  $\theta_c$  is the critical incidence angle in Figure (A.1), and  $z_0$  the thickness of the first layer ( $v_0$ ).

If we look at Figure (A.1) and, since  $xb/v_0 = ab/v_1$ , then :

$$t_s = (sx + xb)/v_0 - ab/v_1 = sx/v_0 \quad (\text{A.6})$$

where:  $(sx + xb)/v_0 = t_{sb}$  ; and  $sx/v_0 = z_0 \cos \theta_c / v_0$  .

Similarly, it can be shown that:

$$t_r = z_0 \cos \theta_c / v_0 \quad (\text{A.7})$$

Therefore the delay time analysis allows the determination of the first layer thickness below the shot and the receiver. However the knowledge of the first and second layer velocity is required and the delay time analysis assumes a local flat interface below the shot and the receiver and works only for a gentle dipping interface.

**APPENDIX B - THE PLUS-MINUS TIME ANALYSIS**  
**METHOD: THEORY**

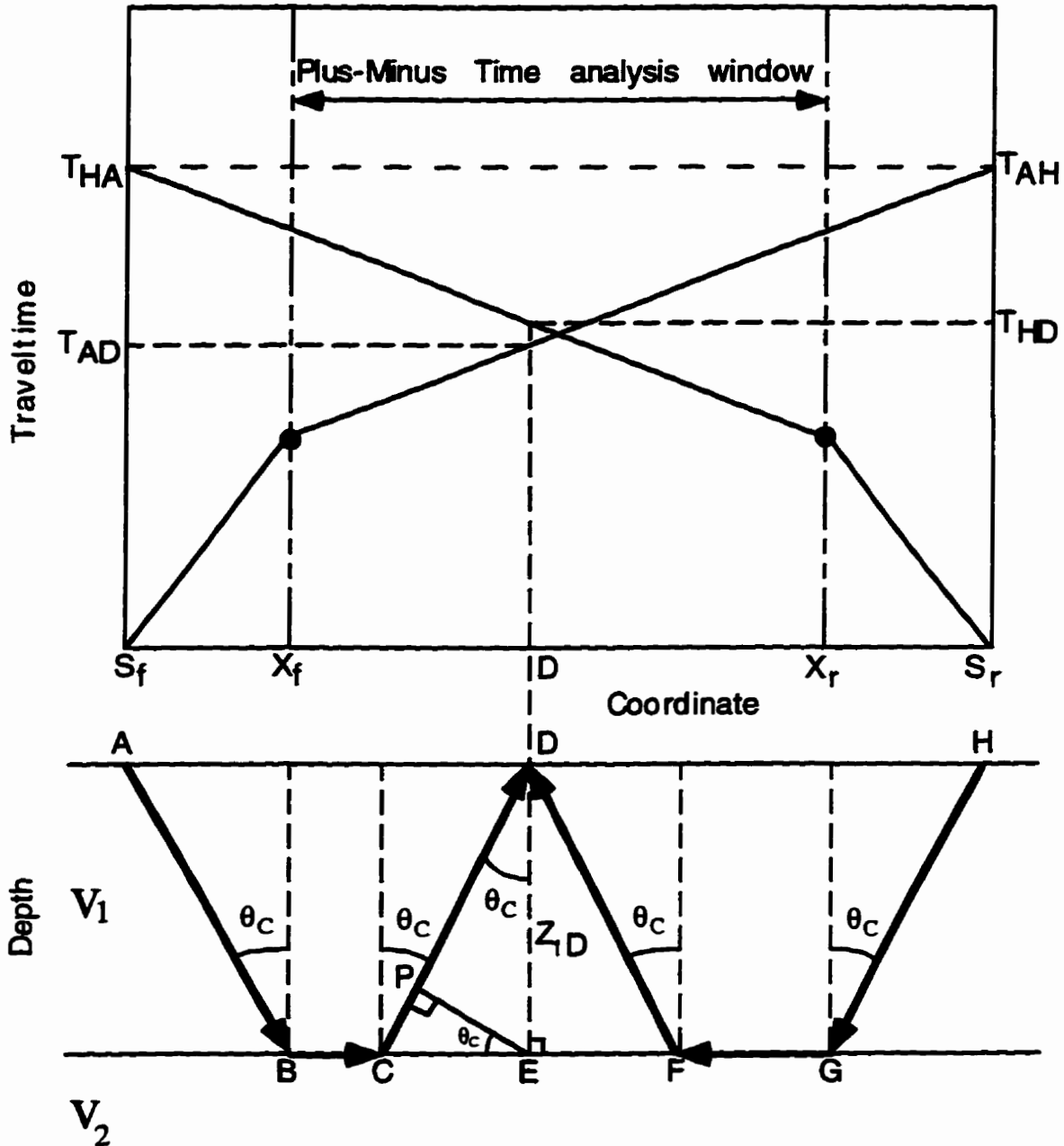


Figure B.1. Plus time analysis according to the "plus-minus" method of Hagedoorn (1959).

The Plus time value ( $T^+$ ) can be evaluated for each of the receivers inside that window (Figure B.1). The Plus time value at a receiver ( $T^+D$ ) is defined as the sum of the

traveltime at the receiver from a forward source ( $T_{AD}$ ) and the traveltime at the receiver from the reverse source ( $T_{HD}$ ), minus the traveltime between the two sources ( $T_{AH}$ ).

$$T^+D = T_{AD} + T_{HD} - T_{AH} \quad (B.1)$$

Each one of these raypath traveltimes can be replaced by smaller raypath traveltime segments:

$$T_{AD} = T_{AB} + T_{BC} + T_{CD} \quad (B.2)$$

$$T_{HD} = T_{HG} + T_{GF} + T_{FD} \quad (B.3)$$

$$T_{AH} = T_{HA} = T_{AB} + T_{BG} + T_{GH} \quad (B.4)$$

The raypath traveltime  $T_{BG}$  can also be replaced by smaller segments:

$$T_{BG} = T_{BC} + T_{CE} + T_{EF} + T_{FG} \quad (B.5)$$

The substitution of Equation (B.5) into Equation (B.4), and then of Equations (B.2), (B.3), and (B.4) into Equation (B.1), gives the following equation:

$$T^+D = T_{CD} - T_{CE} + T_{FD} - T_{EF} \quad (B.6)$$

where  $T_{CD} - T_{CE}$  is the left Delay time ( $\delta_{Dl}$ ) and  $T_{FD} - T_{EF}$  is the right Delay time ( $\delta_{Dr}$ ) at receiver D.

Now, if we replace the traveltime by the equivalent distance divided by the corresponding seismic velocity, Equation (B.6) becomes:

$$T^+D = CD/V_1 - CE/V_2 + FD/V_1 - EF/V_2 \quad (B.7)$$

where  $CD/V_1 - CE/V_2 = \delta_{Dl}$  and  $FD/V_1 - EF/V_2 = \delta_{Dr}$

The left Delay time can be expressed as:

$$\delta_{Dl} = (CP + PD)/V_1 - CE/V_2 \quad (B.8)$$

From Snell's law, it can be shown that  $CP/V_1 = CE/V_2$ , so that the left Delay time ( $\delta_{Dl}$ ) becomes  $PD/V_1$ .

From there, a link between the left Delay time ( $\delta_{Dl}$ ) and the thickness of the first layer below receiver D ( $Z_{1D}$ ) can be established:

$$\delta_{Dl} = PD/V_1 = [Z_{1D} \cos(\theta_c)]/V_1 \quad (\text{B.9})$$

where  $\theta_c = \sin^{-1}(V_1/V_2)$

Similarly, it can be shown that the right Delay time ( $\delta_{Dr}$ ) is linked to the thickness of the first layer below receiver D ( $Z_{1D}$ ):

$$\delta_{Dr} = [Z_{1D} \cos(\theta_c)]/V_1 \quad (\text{B.10})$$

According to Equations (B.9) and (B.10), the expression for the Plus time ( $T^+_D$ ) can be expressed as:

$$T^+_D = 2[Z_{1D} \cos(\theta_c)]/V_1 \quad (\text{B.11})$$

where  $T^+_D$  is equal to the sum of  $\delta_{Dr}$  and  $\delta_{Dl}$ .

Hence, the thickness of the first layer at the receiver D can be found.

$$Z_{1D} = [(T^+_D) \cdot (V_1)] / 2(\cos(\theta_c)) \quad (\text{B.12})$$

The velocity of the first layer can be found using the inverse slope of the first layer arrivals ( $S_f$  to  $X_f$  and  $S_r$  to  $X_r$ ). From the second layer arrivals (after  $X_f$  for the forward spread and after  $X_r$  for the reverse spread), the second layer velocity can be derived using the Minus time analysis (Figure B.2).

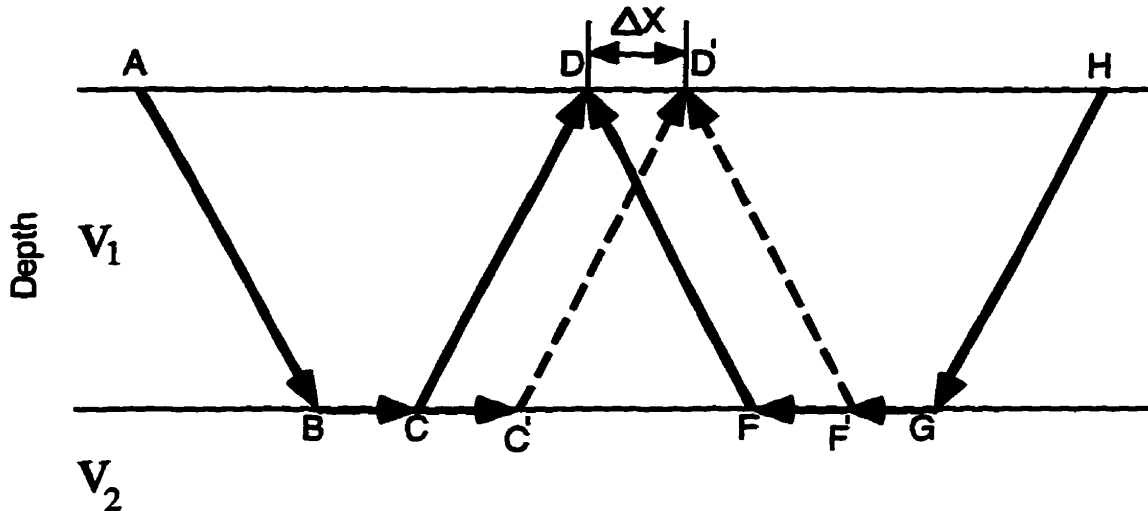


Figure B.2. Minus time analysis according to the “plus-minus” method of Hagedoorn (1959).

The definition of the Minus time at a receiver ( $T^{-D}$ ) is the subtraction of the traveltime at the receiver from the reverse source ( $T_{HD}$ ) of the traveltime at the receiver from the forward source ( $T_{AD}$ ), minus the traveltime between the two sources ( $T_{AH}$ ).

$$T^{-D} = T_{AD} - T_{HD} - T_{AH} \quad (B.13)$$

A velocity analysis of the second layer can be undertaken using the Minus time values at two receivers (D and D') with a specified separation distance ( $\Delta X$ ):

$$T^{-D'} = T_{AD'} - T_{HD'} - T_{AH} \quad (B.14)$$

Subtraction of Equation (B.13) from Equation (B.14) results in:

$$T^{-D'} - T^{-D} = T_{AD'} - T_{AD} + T_{HD} - T_{HD'} \quad (B.15)$$

where  $T_{AD'} - T_{AD}$  and  $T_{HD} - T_{HD'}$  are equal to  $\Delta X/V_2$

The velocity of the second layer ( $V_2$ ) is equal to twice the inverse slope of a best fit line through the Minus time variations ( $\Delta T^{-D}$ ) calculated for each receivers inside the Plus-Minus time analysis window.

$$T^{-D'} - T^{-D} = \Delta T^{-D} = 2(\Delta X)/V_2 \quad (B.16)$$

## **APPENDIX C - THE PLUS-MINUS TIME ANALYSIS METHOD: IMPLEMENTATION**

### **Program overview**

The Plus-Minus time analysis method has been implemented as a interactive, menu driven application in the Matlab computing environment. The program, called PMT, takes at its input first break picks and geometry from a 2D seismic survey. PMT is designed so that the user is guided through the processing flow shown in Figure 2.3. In addition, to the automated processing, manual, interactive editing may be performed on the following intermediate results: crossover points, crossover point averages, the velocity model, and the depth model. When satisfactory depth and velocity models are built, the user may output the depth and velocity models and the static corrections. At any point in the processing flow, the project may be saved to disk.

### **Hardware/software requirement**

The Plus-Minus time analysis software is written in the Matlab language. Matlab is a commercial package which provides a technical computing and visualization environment. A Matlab license is required to run the Plus-Minus time analysis software. Currently, arrival times and geometry are input from ProMax exported database files. The refracted arrival times are previously picked in the processing software (currently ProMax) and then input to the Plus-Minus time analysis software. The geometry files include the receiver coordinates and elevations, and the shot coordinates and elevations, as well as the uphole time (see next section). The software can be run on any platform for which Matlab is available, including UNIX, MS-Windows, and Macintosh.

## Data files

### *Files required for import*

The Plus-Minus time analysis method requires the refracted arrival traveltimes and survey geometry. The import of this information is currently supported using ProMax ASCII database export files.

All the necessary information is in the ProMAX database under the trace order (TRC), surface station (SRF) and source index number (SIN) (Table C.1). The picked refracted arrivals are found in the database under trace order with the name given when saved (GEOMETRY FB\_PICK) (Table C.2). Then go to ASCII/SAVE and save the files with a specified name and the extension ".a\_db".

The same process is repeated for all the geometry files. The receiver coordinates and elevations should be found in the database under surface station (SRF) as receiver x coordinates (GEOMETRY X\_COORD) and receiver y-coordinates (GEOMETRY Y\_COORD), and as receiver elevation (GEOMETRY ELEV) (Table C.3). The source elevations and coordinates can be found under source index number (SIN) as source x-coordinates (GEOMETRY X\_COORD) and source y-coordinates (GEOMETRY Y\_COORD), and as source elevation (GEOMETRY ELEV) (Table C.4).

If available, the uphole time file is found under source index number (SIN) as source uphole time (GEOMETRY UPHOLE). Finally to create a link between the refracted arrivals and the surface station and the source index number, two more files must be exported. These are found under trace number (TRC) as corresponding surface station for each trace number (GEOMETRY SRF) and as trace numbers for each source index number (GEOMETRY SIN) (Table C.2).

Areas	Lines	Orders
Name	Name	TRC SRF SIN

Table C.1. Dataset line orders.

Orders	Attributes
TRC	GEOMETRY SIN GEOMETRY SRF GEOMETRY FB_PICK

Table C.2. Trace order attributes.

Orders	Attributes
SRF	GEOMETRY X_COORD GEOMETRY Y_COORD GEOMETRY ELEV

Table C.3. Surface station order attributes.

Orders	Attributes
SIN	GEOMETRY X_COORD GEOMETRY Y_COORD GEOMETRY ELEV GEOMETRY UPHOLE

Table C.4. Source index number order attributes.

*Exporting files from PMT*

The output of the PMT method analysis is a depth model, a velocity model and static corrections. The depth model contains the interface elevation between the first and second layer at each receiver location (surface station) (Table C.5). This model is exported into a file with the extension ".dpt". The velocity model contains the velocity of the first and second layer at each receiver location (Table C.6). This model is exported into a file with the extension ".vel". The static corrections contain the source and receiver statics (Table C.7). Each of these static corrections includes the weathering correction, the elevation correction and the total correction at the corresponding coordinate location. The exported static files have the extension ".sta" added. All the output files are in ASCII format and may be read by most processing software packages.

Receiver #	Coordinate	Surface elevation	Layer1-Layer2 interface elevation	Layer1 thickness
------------	------------	-------------------	-----------------------------------	------------------

Table C.5. Depth model.

Receiver #	Coordinate	Layer1 velocity	Layer2 velocity
------------	------------	-----------------	-----------------

Table C.6. Velocity model.

Receiver #	Coordinate	Weathering	Elevation	Total
Shot #	Coordinate	Weathering	Elevation	Total

Table C.7. Static corrections.

**Interactive editing**

During the processing, the following intermediate results may be manually edited. Many of the processing steps use parameterized algorithms which may not produce optimal results with noisy data.

*Crossover points*

If there is a second near-surface layer there will be two crossover points, and the crossover point autopicking routine will sometimes pick the deeper one. This can usually be controlled by specifying the maximum offset during the autopicking process.

The crossover point edit module allows the user to modify each individual crossover point location manually. To enable the "crossover point editing", the "crossover point autopicking process" must be completed. Crossover point editing uses two overlapping shot gathers and the corresponding crossover point locations, i.e. the left crossover point of the left shot and the right crossover point of the right shot. To help edit the crossover point, the arrival picks and the traveltime difference with the median filtered equivalent, as well as the first and second derivative of the filtered traveltime difference are displayed in different windows (Figure 2.6). If the crossover point locations have not been edited before, their locations should correspond to the maximum of the second derivative curves. The options are to move the crossover point locations, to delete the crossover points or to add a crossover point. Now, only one crossover point is allowed on each traveltime difference segment curve and should belong to the smaller traveltime arrival spread.

### *Crossover point averages*

The crossover point average editing module can be used after the crossover points have been picked and averaged. All the crossover points (CVPs) at a given location are averaged in the crossover averaging module. The CVP average editing module allows for the precise control of this averaging process. This editing module looks at one shot gather (left and/or right spread(s)) and at the corresponding left and/or right crossover point average(s). Figure C.1 shows, in the top right corner, the arrivals with the crossover point averages. Below the arrivals window, all the possible traveltime difference (TD) curves with the shot gather are being aligned to their flat portions and then stacked. Stacking the TD curves results in noise reduction. Then, the median filtered equivalent of the stacked TD curves as well as the first and second derivatives are shown. Now the locations of the maximum second derivative might not correspond to locations of the crossover point averages due to some remaining bad crossover point picks in the averages or to some stacking problem and noise in the data. The main point of this editing function is to let the user interpret which location for the crossover point average is more valid.

The stacking process of all the traveltime difference curves should reduce the level of noise in the data by canceling the inconsistent traveltime differences due to bad arrival picks. The process of crossover point averaging and rejection is also statistically reliable, so that the final decision on crossover point location should be made as an interpretation by the user.

Crossover point rejection can be accomplished interactively in this function or in the crossover point rejection process. The advantage of doing the crossover point rejection in this function is that the standard deviation limit can be modified and the resulting crossover point average observed interactively. Also, instead of stacking all the possible TD curves, the user can constrain the range of the overlapping shots that are going to be used. Now the crossover point averages saved in the database can be moved to the maximums of the second derivative of the stack traveltime difference (STD) or to the crossover point average locations according to the rejection criteria or anywhere else along the traveltime difference segments.

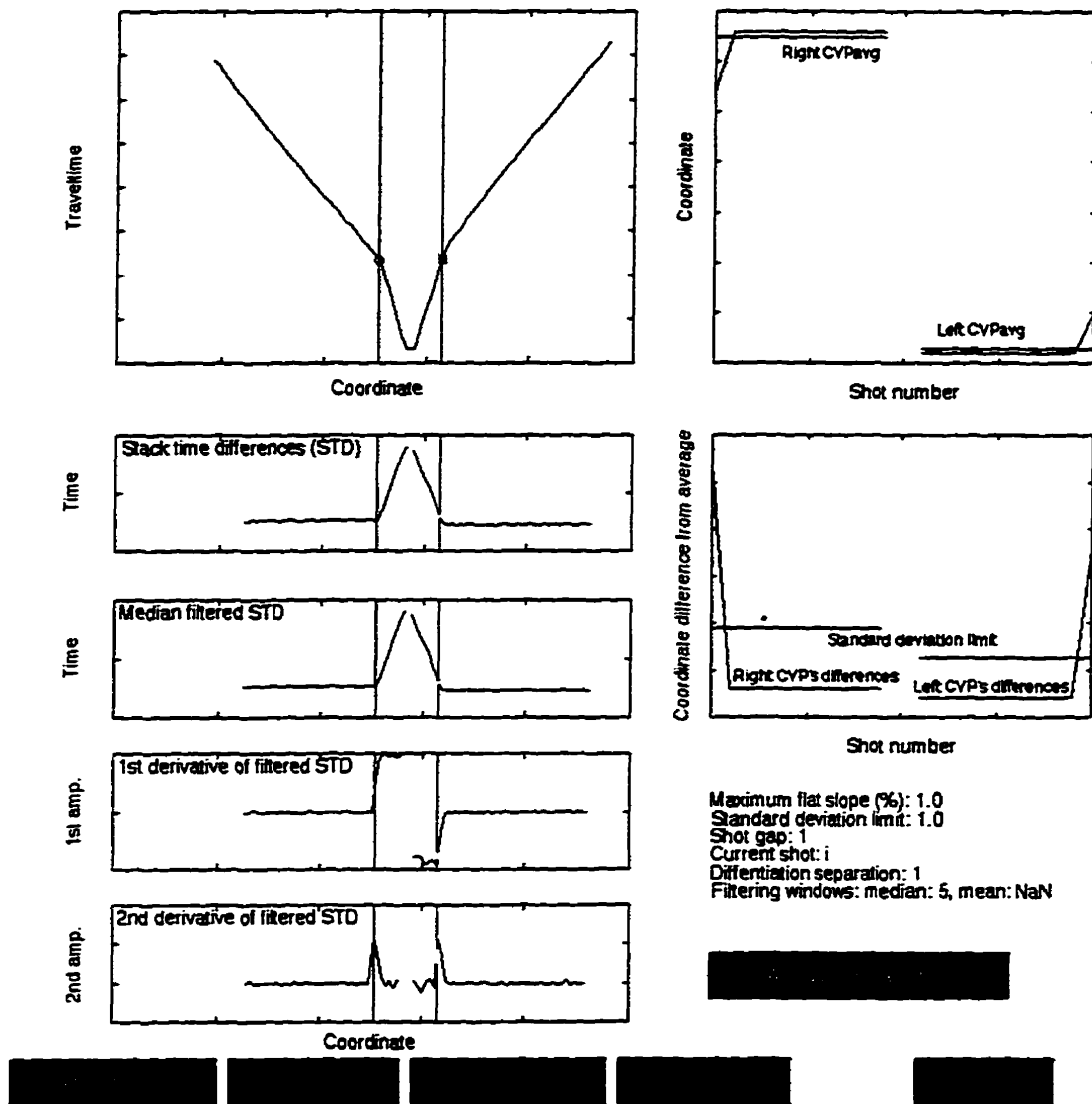


Figure C.1. Crossover point averaging editing.

### *Velocity model*

The first and second layer velocities can be median filtered and manually edited using the edit velocity model function. The median filter is applied to the first or/and the second layer velocity with a specified window length. The window length is determined according to the degree of smoothness wanted. The velocities should not be changed drastically from one receiver to the next one, according to a realistic near-surface earth model. Also, the first layer velocity should not be greater than the second layer velocity. The use of the "velocity model display" prior to editing the velocity model should help the user identify the modification needed. The velocity changes are allowed only along the velocity axis, so that the velocity values remain at the same receiver locations.

*Depth model*

Finally, the depth model editing function allows the filtering and the manual editing of the interface between the first and second layers. The filtering of the first and second layer interface using a median filter with a specified window length will smooth the interface and reduced its frequency content. As the window length increases, the frequency content of the interface decreases. The use of the median filter is generally not recommended in order to keep all the details in the depth model, which determine the short wavelength static corrections. The median filter should be used; if necessary, or if only the long wavelength component is wanted. The first and second layer interface can also be manually edited in the same way. The depth model manual editing should be used only to modify unreasonable irregularities along the interface. The depth model depends on the velocity model and the Plus time values, so that irregularities in the depth model are due to the velocity model or/and to the Plus time values. It is better to correct the velocity model and check the Plus time values than edit the depth model. Remember that changes in the depth model will directly change the static corrections, so that only necessary modifications should be undertaken.

**APPENDIX D - WATER WELLS IN THE AREA OF  
THE BLACKFOOT 2D-3C DATA**

The water well data information were provided by the Alberta Environmental Protection.

Well location LSD/SEC/TWP/RGE/W. MER	Date	Lithology	Water level
15-07-023-23-W4	August, 1995	0-4 m: clay, 4-24 m: shale (with sandstone), 24-30 m: sandstone	15 m
04-08-023-23-W4	January, 1966	0-12 m: clay, 12-69 m: shale, 69-70 m: sandstone	40 m
NE-08-023-23-W4	June, 1990	0-3 m: clay, 3-4 m: till, 4-23 m: shale, 23-26 m: coal, 26-34 m: shale, 34-46 m: fine-grained sandstone, 46-52 m: shale, 52-55 m: fine-grained sandstone, 55-60 m: shale, 60-67 m: fine-grained sandstone	
SW-15-023-23-W4	January, 1991	0-2 m: till, 2-15 m: shale, 15-19 m: coarse-grained sandstone, 19-32 m: shale, 32-39 m: coarse-grained sandstone, 39-59 m: shale, 59-70 m: medium-grained sandstone	
SE-17-023-23-W4	September, 1988	0-8 m: clay & till, 8-43 m: shale (with sandstone & coal)	3 m
NW-20-023-23-W4	December, 1974	0-4 m: clay, 4-28 m: shale (with sandstone)	15 m

Table D.1. Water well information in the area of the Blackfoot 2D-3C data.